POLYMERIC PRESSURE CUSHIONS FOR POTENTIAL APPLICATIONS ON FOREARM ROBOTIC ORTHOSES

by

Nezam Matthew Alavi

B.A.Sc., Simon Fraser University, 2013

Thesis Submitted in Partial Fulfillment of the
Requirements for the Degree of
Master of Applied Science

in the
School of Engineering Science
Faculty of Applied Sciences

SIMON FRASER UNIVERSITY

Spring 2017

Approval

Name:	**Nezam Matthew Alavi**
Degree:	**Master of Applied Science**
Title:	***Polymeric Pressure Cushions for Potential Applications on Forearm Robotic Orthoses***
Examining Committee:	**Chair:** Dr. Michael Adachi Assistant Professor

Dr. Carlo Menon, P.Eng
Senior Supervisor
Professor

Dr. Ash Parameswaran, P.Eng
Co-Supervisor
Professor

Dr. Bonnie L. Gray, P.Eng
Internal Examiner
Professor
School of Engineering Science

Date Defended/Approved: November 18th, 2016

Abstract

Robot devices for stroke rehabilitation measure the interaction forces between users and the structure of the orthosis through load cells. Although these load cells are well-suited for stationary robotic devices in hospitals, they do not easily allow for the development of affordable wearable orthoses that can assist in daily living. When load cells are attached onto a robotic orthosis, they neither conform to the shape of the user's body nor directly measure the applied forces at the contact point between the user and the orthosis. A polymeric cushion containing atmospheric air was developed as an alternative technology for measuring forces. A finite element model (FEM) of the polymeric cushion was made to simulate air pressure changes inside the polymeric cushion from applied forces. The polymeric cushions were fabricated entirely of Poly(dimethylsiloxane) (PDMS), making them biocompatible, flexible, and free of electrically conductive materials. An air pressure sensor attached to the tube of the polymeric cushion measured the air pressure and converted it into an electrical signal to be processed by a data acquisition board (DAQ). A test bench setup was made to characterize the relationship between the air pressure and applied force from each polymeric cushion, where a linear stage applied a setpoint force onto the cushion with an aluminum flat plate and a spherical glass tube. The characterization results of the experimental test bench setup were compared to the FEM results. Six polymeric cushions were mounted onto a wrist brace exoskeleton, where a LabVIEW program was written to record specific combinations of pressure sensors and measure the pronation/supination torque of the forearm (rotation), flexion/extension force of the elbow (up/down), and the internal/external rotation of the shoulder (left/right) at the forearm. These measured force values from the polymeric cushions were compared to the measured values of a torque sensor and load cell. The potential suitability of polymeric cushions for the measurement of isometric forces on an orthoses, is compared to the abilities of exoskeleton devices which involve the motions tested in this study using the wrist brace exoskeleton.

Keywords: Cushion; force; forearm; polymer; pressure; orthosis

Dedication

I would like to dedicate this thesis to those are going through rehabilitation from stroke and living their lives with dignity and respect.

Acknowledgements

I would like to thank my senior supervisor, Dr. Carlo Menon, for allowing me to be his masters of applied science student and work on projects that are making a difference in the world.

I would like to thank Mr. Stefano Zampierin for his support and the work he did in the MENRVA lab.

Special thanks to all the members of the MENRVA lab, past and present, for their friendship and kindness throughout my time working alongside them. My best wishes for your futures.

Last but not least, I would like to thank my family for their support, patience, and encouragement, which helped me finish my masters. Without you, I would not be able to go after my dreams.

Table of Contents

List of Tables

List of Figures

List of Acronyms

3D	Three Dimensional
ADC	Analog to Digital Card
BWRD	Bimanual Wearable Robotic Device
CAD	Computer Aided Design
CO_2	Carbon Dioxide
DOF	Degrees of Freedom
EMG	Electromyography
FEM	Finite Element Model
FES	Function Electrical Stimulation
FMV	Fuzzy Membership Value
GCF	Ground Contact Force
IC	Integrated Circuit
MEG	Magnetoencephalography
MVC	Maximum Voluntary Contraction
M-P	Myo-Pneumatic
MRI	Magnetic Resonance Imaging
MSS	Muscle Stiffness Sensor
PCB	Printed Circuit Board
PDMS	Poly(dimethylsiloxane)
PMMA	Poly(methyl methacrylate)
pMMG	Pressure Mechanomyography
PVC	Polyvinyl Chloride
RKI	Residual Kinetic Image
RMSE	Root Mean Squared Error
TAP	Tendon-Activated Pneumatic
VSA	Variable Stiffness Actuator

List of Symbols

a	Length of the plate
b	Width of the plate
c	Radius of the circular area
$C1$	Polymeric Cushion 1
$C2$	Polymeric Cushion 2
$C3$	Polymeric Cushion 3
$C4$	Polymeric Cushion 4
$C5$	Polymeric Cushion 5
$C6$	Polymeric Cushion 6
d	Distance from the center of the wrist brace to the cushion force
D	Flexural rigidity of the plate
E	Modulus of elasticity
ΔF	Difference in force
F	Applied force
$F(x)$	A function of variable x
F_m	Coefficient of the Fourier series with respect to x
F_{C1}	Force on C1
F_{C2}	Force on C2
F_{C3}	Force on C3
F_{C4}	Force on C4
F_{C5}	Force on C5
F_{C6}	Force on C6
F_{FE}	Force of the elbow's flexion and extension
F_{IE}	Force of the shoulder's internal and external rotation
F_{LC}	Force of the load cell
F_{WB}	Force of the wrist brace
$G(y)$	A function of variable y
G_n	Coefficient of the Fourier series with respect to y
h	Thickness of the plate
$J_1(\gamma_{mn}c)$	Bessel function of order one with argument $\gamma_{mn}c$
K	Coefficient of the trend lines between the EXP and FEM

m	Whole integer
n	Whole integer
n_a	Number of molecules of air in the cushion
ζ	X-coordinate of the circular area's centroid
η	Y-coordinate of the circular area's centroid
θ	Polar coordinate variable
P	Air pressure
ρ	Polar coordinate variable
ρ_a	Density of air
q	Intensity of the load
q_{UDLmn}	Intensity of the load for the uniformly distributed load at m,n
q_{UDLo}	Intensity of the load for the uniformly distributed load
q_{CLmn}	Intensity of the load for the centralized load at m,n
q_{CLo}	Intensity of the load for the centralized load
R	Gas constant
R^2	Coefficient of determination
$S1$	Pressure Sensor 1
$S2$	Pressure Sensor 2
$S3$	Pressure Sensor 3
T	Temperature
T_{PS}	Torque of the forearm's pronation supination
ΔV_c	Change in volume of the cushion
V_o	Initial volume of the cushion
v	Poisson's ratio
w	Deflection of a plate
w_{mn}	Deflection of a plate at m,n
w_{CLmn}	Deflection of a plate at m,n for the centralized load
w_{UDLmn}	Deflection of a plate at m,n for the uniformly distributed load
x	Cartesian coordinate variable
y	Cartesian coordinate variable

Chapter 1. Introduction

Stoke is the number one cause of adult disability, affecting 400,000 Canadians, and it affects their physical, emotional, and cognitive abilities [1]. One of the aftereffects of stroke is that one side of the body is more affected than the other. Using traditional rehab equipment, the patient can't feel what their affected arm is doing, or the therapist has to move their arm passively for them, which has been shown to be not very effective [2]. Recently, new technologies in robotic rehabilitation have been improving the way that stroke survivors are recovering [3]. Studies have shown that robot assistive rehabilitative movements help in functional recovery from stroke [4]. Therapists are also often managing multiple patients at once with very little individual face time, whereas a rehabilitation robot gives the user the ability to actively engage in the exercise training and in turn, helps to better recover from a stroke [5]. Rehab robotic devices give medical professionals more time for their patients and help to reduce the $3.6 Billion cost of stroke on the Canadian economy [1]. These robotic devices need to measure the applied forces from the users in order to understand how to react in accordance with their rehabilitation protocols. What is proposed in this thesis is an inexpensive device that is able to measure forces from a user, provided that they can still move their move their body after a stroke, onto an exoskeleton in a way that is comfortable to use, measures the user's forces directly at the point that the forces are applied, and does not use any electrically conductive materials. The proposed device is a polymeric air cushion force sensor.

1.1. Motivations

Robotics used for stroke rehabilitation measure the interaction forces between the human and the robot via load cells. The accuracy of the load cells makes them suitable for stationary robots used in hospitals, although their cost and inability to conform to the shape of the human impedes their use in the development of more affordable robotic orthoses for assisting in daily activates.

This work explores the use of polymeric air cushions as a potential alternative technology for measuring the interaction forces between the user and the wearable rigid structure of a robotic orthosis. A flexible polymer material, such as PDMS, would allow for a biocompatible and comfortable interface with a low fabrication cost. A series of cushions mounted onto an orthosis would allow for the measurement of forces in various degrees of freedom (DOF).

1.2. Objectives

1. Improve concept of polymeric air cushion force sensor for the forearm
2. Apply finite element model and validate the proposed concept cushion
3. Validate the finite element model and the proposed concept in an application

1.3. Summary of Contributions

The fabrication concept and original configuration of the cushion came from the previous work done by Zampierin et al [6], who created a number of configurations for the cushion molds, and then went forward with a mold that created a cushion that did not have a tube. The sealing of the Tygon tube and the cushion's outlet could not reliably hold the air inside, and so the air pressure would be lost and the cushion would have to be regularly repaired. To remedy this, a new leak-resistant cushion configuration was fabricated, as seen in Chapter 3, and thus became part of my work. I redesigned the cushion mold to include the tube, which drastically reduced the number of repairs needed for a successfully fabricated cushion. I also did leak tests to prove that there were no leaks when fabricating the cushions using my mold. Using a CO_2 laser, I cut the shape of the cushion and bonded the top and bottom layers. An FEM model of the cushion with comparisons between FEM and experimental results of a glass tube and an aluminum plate as external loads on the top surface of the cushion were my work, as presented in Chapters 5 and 7, respectively. Characterizing and testing the cushions with the wrist brace exoskeleton were performed by Zampierin et al. [7]; however, these tests were repeated by me for the newly configured cushions. I added a long period loading test, a maximum pressure test, and I changed the

repeatability test to use a force feedback LabVIEW program. These improvements of the cushion configuration allow for a more practical application of measuring isometric interaction joint forces from the user onto exoskeletons at ranges of applied forces that are closer to those as suggested by Tsagarakis et al. for rehabilitation orthoses, while still being comfortable to use and inexpensive to fabricate for potential applications on assistive devices for in home use. These polymeric air cushions when used in rehabilitation and assistive devices will allow stroke individuals to rehabilitate more comfortably, effectively, and efficiently while a medical professional can give feedback to the stroke-affected individual on their rehabilitation progress and how to better improve their recovery.

1.4. Thesis Layout

Chapter 2 is an in-depth literature review, outlining recent work and state of the art research surrounding flexible air cushion pressure sensors. Chapter 3 discusses the requirements of the cushion to perform well and its advantages for force sensing applications. Objective 1 is covered in Chapter 4. Chapter 4 discusses the concept design of the polymeric air cushion. Objective 2 is covered by Chapter 5 to Chapter 7. Chapter 5 presents the finite element modelling of a polymeric air cushion. Chapter 6 includes the fabrication and experimental testing of the cushions. Chapter 7 compares the finite element modelling with the experimental testing results. Objective 3 is covered in Chapter 8. Chapter 8 presents the 3D-printed wrist brace exoskeleton prototype and the application testing with the cushions. Chapter 9 discusses this paper's research and results. Chapter 10 concludes this paper with a summary of how the objectives were met, as well as recommendations for future work.

Chapter 2. Literature Review

Polymer force sensors are devices made of a flexible polymer that bends when loaded by an applied force and outputs an electrical signal. Usually, these sensors are closed systems of a contained volume of air in the form of a cushion, where the change in air pressure due to the deformation of the cushion from an applied load is given from the output of air pressure sensor. In this chapter, an in-depth literature review of polymer force sensors is presented. First, polymer force sensors are described as to what they are in more detail, then the progression of research in the field of polymer force sensors is presented. The mechanism of polymer force sensors, as well as why they are advantageous when compared with non-polymer force sensors, is explained.

2.1. Force Sensing Mechanisms for Exoskeletons

Robotics are playing a more prominent role in the biomedical field [8], and various devices are being used for human rehabilitation from a stroke [9]. Robotic exoskeleton systems have been developed world-wide with rehabilitation protocols that monitor the user's improvement [10][11]. This is done through feedback sensors that, via analytical software, measure various metrics through the user's position and applied forces [20]. Many of these robotic devices include wearable orthoses as part of exoskeletons [12], as well as hand-held devices that are end effector-based [13], such as those used for grasping, which use dynamic signals like force or torque exerted by the subject [14]. These systems can use sensors such as force sensing resistors (FSR)s [15], capacitive force sensors [16], load cells [17], and torque sensors [18] to measure the applied forces that are exerted by the user of the device on the mechanical system. These methods of force measurement can have high precision or be very robust, but they may not be best suited for measuring interaction forces on low cost wearable devices that can measure the applied force at the point of contact while comfortably conforming to the user's body. Alternatives to the cushion, such as electromyography (EMG), can be too sensitive to environmental conditions like electric and magnetic noise [19]. One technique for measuring brain activity in stroke rehabilitation involves the use of an MEG (Magnetoencephalography), where a stroke-affected individual is inside of a magnetically

sealed room that prohibits the use of electrically conductive materials [20]. These polymer force cushions have a unique advantage in that they would not interfere with the electrical restrictions of the room, and can be used to observe brain activity when the stroke-affected individual applies forces onto an orthosis.

2.2. Prior Art in Force Sensing Air Cushions

Polymer force cushions are deformable sensors made from polymers, which translate an input load into an electrical signals. There have been various early works in using air cushions to measure applied forces from the human body. A device for trans-radial amputees was made to characterize the movements of the muscles in the forearm by studying the pressure patterns in the limb during phantom finger taping [21]. This device involved an array of 32 myo-pneumatic (M-P) sensors that were fabricated from polyurethane open-cell foam and encased in a 5 x 10mm polyethylene bag, with a maximum thickness of 5mm, and attached to a flexible tube with a 2mm outer diameter [22]. These M-P sensors were embedded in a silicone sleeve that was tightly fitted against a custom designed hard prosthetic socket and the wear's limb, seen in Figure 1. This was then used to produce a residual kinetic image (RKI). The RKIs were used to decode and map the flexion and extension motion of their phantom pink finger, middle finger, and thumb from their limb.

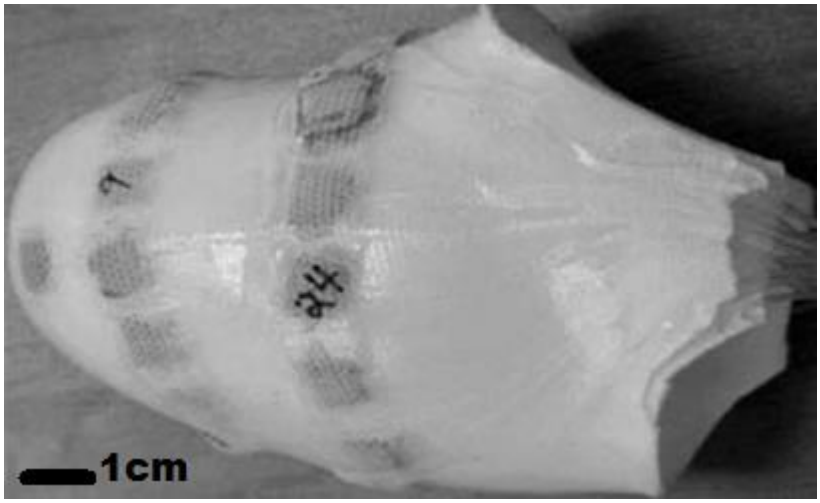

Figure 1 - Smart-sleeve's custom silicone design with sensors and tubes [21].

Each of the 32 M-P sensors were connected to a pressure transducer (Sensym SCX-01, Santa Clara, CA) and processed through an 8-channel data acquisition board (DAP/1200, Microstar Laboratories, Inc., Bellevue, WA). The data collected from the M-P sensors were filtered, sampled, and then stored for processing offline to produce the RKI. The paper by Abboudi et al. describes the characteristics of the M-P sensors, which they call Tendon-activated pneumatic (TAP) sensors. The maximum measurable force of these TAP sensors was calculated to be 0.35N until saturation, based on the 5mm thickness of the foam sensor and its 0.07N/mm stiffness [22]. This results in a maximum measurable applied torque at the elbow for flexion/extension to be 0.1Nm, from an average arm length of 26.2cm. Although it may be suitable for measuring residual muscle movement, it is not practical to use for measuring joint forces on an orthosis, as this is only 0.13% of the recommended elbow flexion/extension torque that exoskeletons should be capable of, which is described by Tsagarakis et al. as 72.5Nm.

Force sensors in shoes have been widely investigated by the research community with the use of FSRs for monitoring gait cycles [23] such as the work done by Yu et al. Another device has been made to smoothly and continuously measure the ground contact forces of an individual’s foot during the different phases of the gait cycle [24]. This device was used inside of a shoe and consisted of four coils of silicone tubing that were placed

underfoot for measuring foot contact at the (a) hallux (b) first metatarsal (c) fourth metatarsal and (d) heel of the foot, as seen in Figure 2.

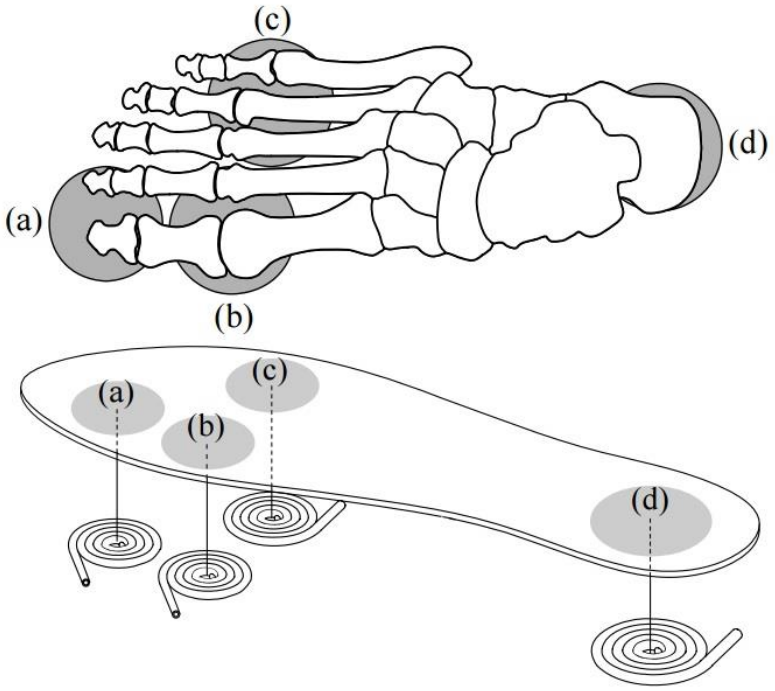

Figure 2 - Ground contact force sensors used in a shoe during gait cycles [24].

The Ground Contact Force (GCF) tubes of air were compressed and relieved while air pressure sensors measured the changes in pressure of the four bladders, converting it into electrical signals. A fuzzy logic method was used to map the 6 phases of walking: initial contact, loading response, mid stance, terminal stance, pre-swing, and the swing phase. Each of the walking phases were associated with a fuzzy membership value (FMV), which indicated the phase of the gait cycle that the individual was currently in. The coiled shape of the tubed cushion produced a circular or oval shaped surface area that was not fully covered by the foot, resulting in less sensitivity to the true applied forces from the body onto the cushion. The walls of the tube may have also interfered with sensing the applied forces, since they added an additional layer of structural stiffness, the space of which could have instead been taken up by more air to be used for sensing. It is also not clear how the coil maintained its shape under pressure while walking and whether the coiled tube would separate, causing a loss of sensitivity and efficiency.

Another use of air cushions has been to measure the deflection of the muscles of the arm in order to estimate the intended action of a wearer of an orthosis. The pressure cushions, labeled as muscle stiffness sensors (MSS), were attached to the bicep and the brachioradialis as seen in Figure 3.

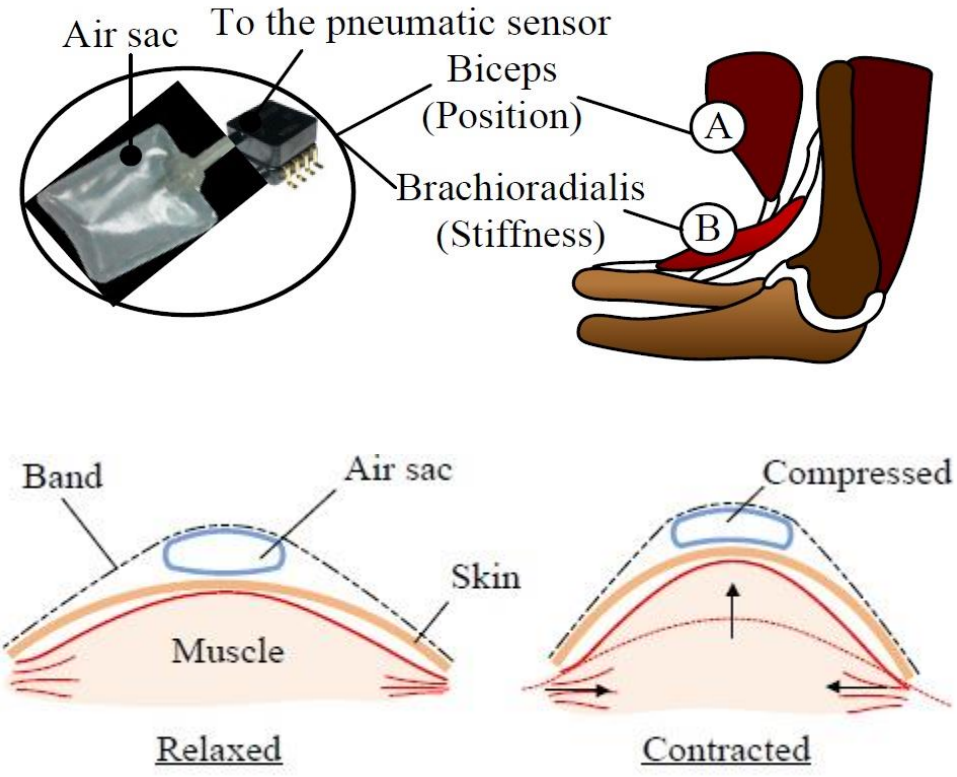

Figure 3 - Cushions measuring the intention of the user of an exoskeleton [25].

The 30 x 30 x 5mm^3 cushions, weighing 1g, were connected to pressure sensors, where a digital signal processor read the pressure as a voltage from both cushions A and B. The system then evaluated the position of the user with their intention to flex or extend their elbow from the bicep muscle, and so a change in added weight to the end of the arm could be sensed from the stiffness of the brachioradialis muscle contraction. This, together with a variable stiffness actuator (VSA) controller, could change the stiffness of the exoskeleton and have it imitate the motion of the wearer. The current configuration of the MSS pressure sensors made it difficult to place multiple sensors on the forearm between the bandage and the orthosis. The tightness of the arm band would change the initial pressure of the cushion when at rest, as stated by Bae et al., and needed time to be

adjusted before beginning the experiment. It would take a long time to add an array of sensors onto the body with this method, and have it prepared for testing, even with the assistance of someone who has had a stroke.

Wearable wrist bands that measure the forces of the muscles around the forearm are becoming more prominent in the research community, such as the Tangential Force Sensing System for measuring forearm forces [26] from Makino et al., as well as in the commercial market, such as the Myo Gesture Control Armband [27] from Thalmic Labs Inc. A similar air cushion device has been made to map the movements of a forearm for gesture recognition using Polyvinyl Chloride (PVC) plastic and air cushions with pressure sensors attached to the cushions which use Bluetooth to communicate the user's arm movements to a receiver [19]. A series of six 35 x 40mm^2 air cushion units with EMG electrodes placed around the forearm created a band, as seen in Figure 4, and were attached together around the forearm to measure the muscle deformations as the user moved their wrist and fingers to perform gestures.

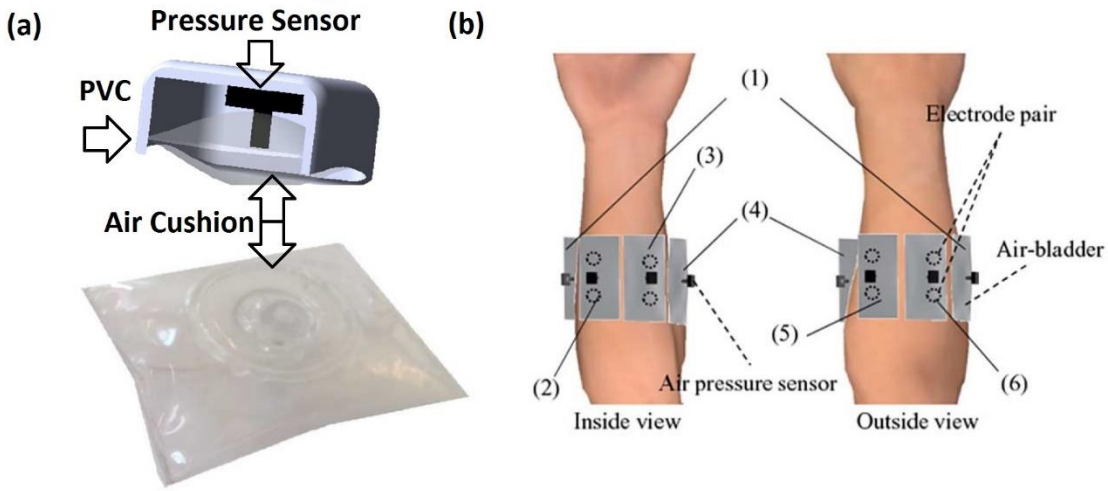

Figure 4 - (a) air cushion and pressure sensor, (b) six cushion arm band [19].

The combination of pressure mechanomyography (pMMG) signals from the air pressure sensors would be used with a fuzzy logic method to recognize six gestures: wrist flexion, wrist extension, mass flexion, mass extension, radial deviation, and ulnar deviation. The range of applied forces from a normal force on the cushion was not stated by Jung et al. and the measured forces were recorded as percentages of a Maximum

Voluntary Contraction (MVC), not a standard physical metric of force. The forces of the forearm muscles were induced by grasping handgrips and the air cushions measured the deflection, although the range of forces measured radially from forearm muscles is expected to be much less than those exerted by elbow flexion/extension. The rigid cover that holds the air cushion limits its range of compression and will saturate its measurement range when the forearm comes into contact with the cover and therefore cannot compress further.

Measurement of forces from the lower limbs is also a growing field of research, such as the calf muscle band for monitoring the legs during gym exercises [28] from Zhou et al. A sensing band with cushions was made to measure the mechanical pressure distribution on a lower-limb exoskeleton as a physical human-machine interface [29]. Light detectors measured the change in between the light transmitter, labeled TX, and the receiver, labeled RX, as seen in Figure 5. The cushion's deformation and the force from a flat surface were simulated using computer aided design (CAD) software, and the cushion's pressure and force values were compared to tactile sensors during an experimental test when worn around the user's thigh.

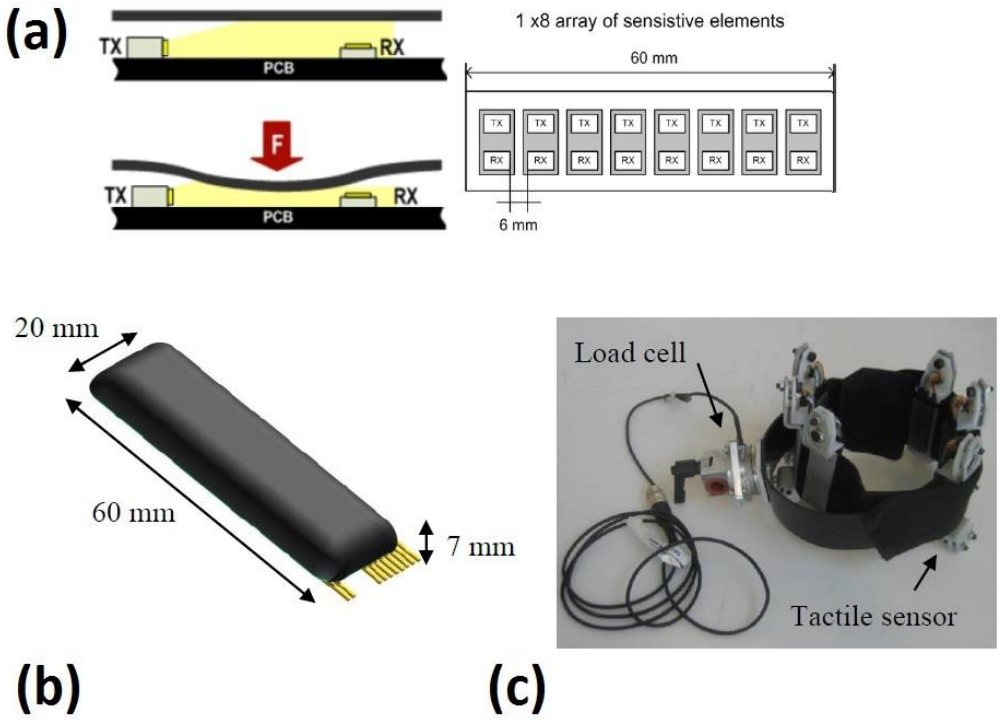

Figure 5 - (a) light transmitter/receiver, (b) sensitive element, (c) thigh cuff [29].

The transmitter used a light emitter (InGaN chip technology, high luminosity green LED, OSA Opto Light GmbH, Köpenicker Str. 325/Haus 201, 12555 Berlin, Germany) to send light to the photo diode receiver (an analog ambient light opto-electronic transducer with current output, Avago Technologies Ltd., 1 Yishun Avenue 7, Singapore). When a load was applied on the pressure sensor, the amount of light received from the photodiode was partially blocked and a lower current output was measured. The components were mounted on a printed circuit board (PCB) and communicated the measured values through a 32-channel analog to digital card (ADC), which were processed by a LabVIEW program (National Instruments Corporation, Austin, TX, USA). The sensing pressure cuff was then tested for static and dynamic loading while comparing its RMSE force output results to a load cell's (ATI Mini45, ATI Industrial Automation, 1031 Goodworth Dr., Apex, NC 27539 USA) as a reliable measurement reference. A structural finite element model of the silicone layer and the rigid PCB surface of the light transmitter/receiver sensors [29] was made, as seen in Figure 6, to find the desired force range. A 3D model of the sensor

was made by De Rossi et al. and it was found that the structure of the silicone had a sinking effect in the middle, altering the transduction in two ways: increasing the light occlusion and reducing the sensitive range at the center, saturating the optoelectronic output.

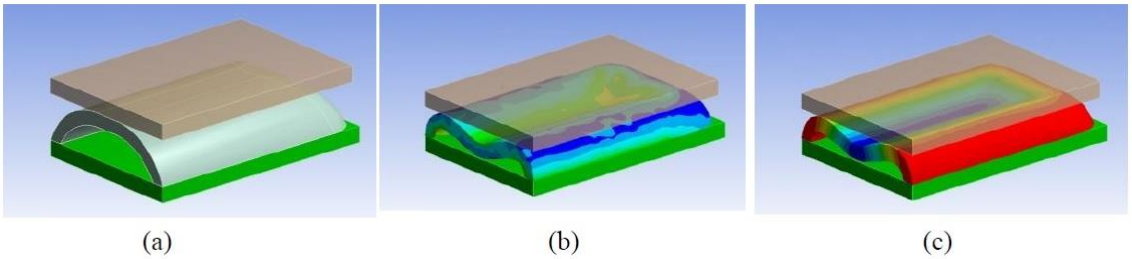

Figure 6 - 3D CAD structural model of silicone cushion on a rigid PCB [29].

With these effects in mind, De Rossi et al. mentioned that they worked on the dimensions of the sensor to obtain their final cushion, and reported a 60N maximum force before the sensor saturated. This applied force at the forearm from elbow flexion/extension would be 15.72Nm, which is 22% of the recommended elbow torque to be measured from an exoskeleton as suggested by Tsagarakis et al. which is 72.5Nm. It should be noted that the finite element model by De Rossi et al. does not incorporate the fluid effects of air inside a cushion and does not accurately represent the interactions of forces involved in air pressure cushions, such as the ones seen in this thesis. Other non-exoskeleton air cushion devices were explored, such as blood pressure cuffs or chamber plethysmography in the literature, but no prior art was found to be similar to the nature of the work done in this thesis since the force cushions in this study.

Chapter 3. Cushion Requirements for Applications

This chapter describes the ideal requirements needed for the polymeric cushion to best perform in force sensing applications for rehabilitation exoskeletons, as well as the advantages of using the polymeric cushion in those applications.

3.1. The Cushion Requirements

A very important aspect of the cushion's performance is to be able to measure joint forces of the human arm at the forearm without saturating within a working range of forces. Tsagarakis et al. describes the suggested forces that an exoskeleton should be designed for with human isometric strength from joints in mind, such as elbow flexion/extension and forearm pronation/supination forces [30] being 72.5Nm and 9.1Nm, respectively. It is not a requirement for exoskeletons to be able to produce these torques because most stroke patients on average will not exert torques higher than 14Nm from elbow flexion extension [31]. Nonetheless, rehabilitation exoskeletons would be better equipped with force sensors that work closer to the range mentioned by Tsagarakis et al. without saturating or breaking for individuals with higher than average arm strength. The need for the cushion to be mouldable when fabricating and flexible when worn led to the use of a polymer, such that it would meet these needs while withstanding the load of a forearm when sensing forces [32]. The light weight and durability of the system are important factors to consider, since they would allow for portability and versatility when mounting the cushions onto the rehabilitation exoskeletons [33]. A simple design would be advantageous for the maintenance of the cushions, and would be important for functionality where servicing time is minimized. Finally, the comfort of the user was a key aspect of its functionality with the cushion system, as individuals may be using the devices that these cushions are mounted to for long periods of time [34]. The comfortable cushions, which act as an interface to the human body, will also encourage users to practice with the wearable devices, which builds on their rehabilitative progress while avoiding unnecessary fatigue and stress [35].

3.2. Advantages for Applications

This section outlines the parameters that are required of a force sensor in certain applications, and how the advantages of the proposed force sensor will be able to deliver on those requirements, where other conventional force sensors would be limited. A wrist brace exoskeleton was mounted with six air cushions on the interface surface, with the goal of being able to ideally meet the following criteria. Air-based cushions are not limited by the size or weight of their pressure sensors, since the tube linking the cushion to the external pressure sensor can in fact be attached to any pressure sensor. This makes the cushions more versatile for users who need a particular range of highly accurate measurements that can only be taken with specific air pressure sensors that may be large and expensive. Due to the fact that the initial air pressure in the cushion is atmospheric before being worn, the cushions are simple to troubleshoot through exposing the cushion to the open air pressure in the room. This becomes very important for its use for potential in-home therapy devices with clinical physicians and individuals with stroke [36], as no pre-pressurization is needed. Air-pressure changes can be measured more robustly than minute changes in electrical signals such as those from electromyography (EMG) with small signal to noise ratios [19]. When applying a functional electrical stimulation (FES) to a muscle, or when measuring muscle activity using EMG, air-based cushions will not interfere with their electrical signals due to the cushion's non-conductive material. The cushions are fully in contact with the user's arm and structurally independent from the orthosis, which allows for direct measurement of the user by the cushions; this reduces the calculated error that would occur from the structure affecting the user's arm's measured forces. The flexible cushions conforming to the user's arm also allows for maximum readability of the forces being enacted, due to there being no gap between the cushion and the arm. Biocompatible Poly(dimethylsiloxane) (PDMS) air cushions are also very safe and ethically sound to use [37] [38], as well as being a soft and comfortable material to interface between the human body and the orthosis.

Chapter 4. Polymeric Air Cushion Concept Design

Objective 1 is covered in Chapter 4. This chapter describes the cushion and its mold, as well as the wrist brace exoskeleton upon which the cushions are mounted. The cushion fabrication process is described, as well as a test with which air leakages were detected, and the electronics of the sensing unit are also elaborated upon. This chapter sets up the cushions in preparation for the subsequent chapters involving Objective 2.

4.1. The Bladder

The previous configuration of the cushion from the work done by Zampierin et al. is presented in Figure 7. The shape and configuration of the previous cushion was chosen with a rectangular profile, a 20 x 50mm flat top surface area, and an outlet hole to be fitted with a Tygon tube, after a series of other configurations were considered [6]. The previous version of the cushion had a rigid top surface made of Poly(methyl methacrylate) (PMMA) that was used to apply a uniformly distributed load onto the cushion. In short, the new cushion's bladder improved on two major issues. The first was that the PMMA piece was removed to improve the comfort of the user while being able to conform to the shape of the forearm. The second was that the cushion was molded such that the bladder and tube were one uniform piece in order to stop leaking air that was found to come from the joint interface between the Tygon tube and the cushion's outlet, despite previous attempts to seal the interface with silicone gels, thermal bonding, and epoxy gels.

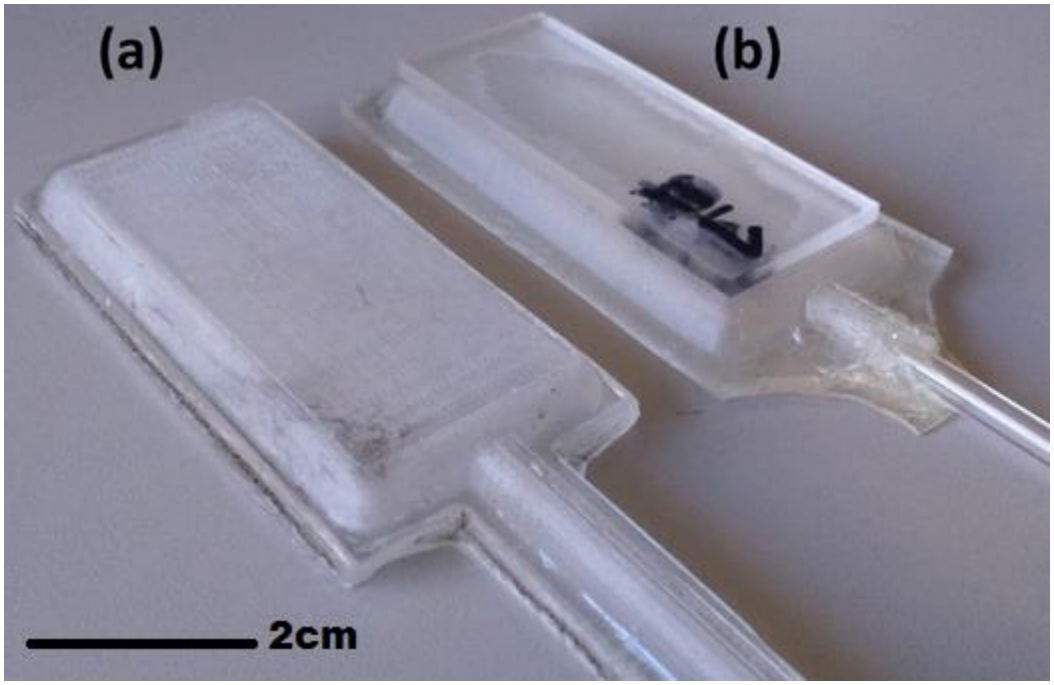

Figure 7 - New version (a) and previous version (b) of the polymeric cushion.

The dimensions for the polymeric cushion were chosen to be 50mm in length, 20mm in width, and 1mm in thickness. These dimensions were selected such that six cushions could be mounted on a wrist brace exoskeleton while staying in contact with the human arm without having unwanted contact between each cushion. The curvature of the corners of the cushion was chosen to allow a desirable deformation of the bladder, but at the same time ensure that the structure of the bladder holds its initial position when unloaded.

The cushion presented in this thesis had the same dimensions as the previous version made by Zampierin et al. [6], although with a reduction in height since the top of the cushion no longer has the Plexiglas surface. Instead, the cushion consists of a top and bottom PDMS cover that are combined together to create the bladder and outlet tube, as seen in Figure 8.

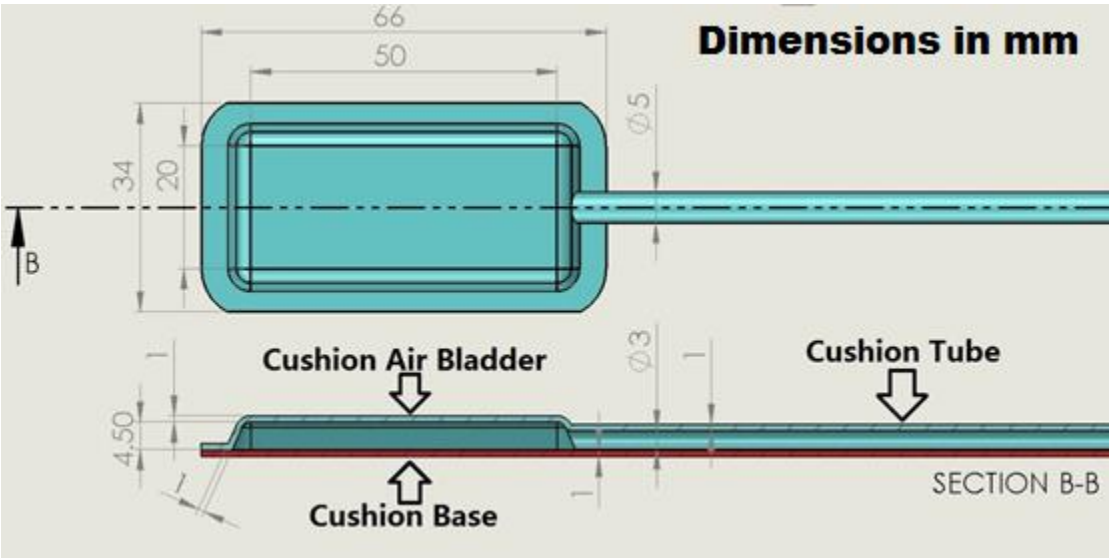

Figure 8 - New cushion bladder with tube (blue) and cushion base (red).

The best polymer material for the cushion had to be chosen from that which was available in the lab. PDMS had a much lower over-shoot when a step response test was performed, and also had a better sensitivity to a threshold test. The cushion bladder and outlet tube were made entirely out of PDMS. The material of the cushion was chosen for its responsiveness, while also being simple to fabricate from inexpensive equipment. Using PDMS to fabricate the cushion was convenient and feasible with the available equipment in our lab for rapid prototyping [7].

4.2. Cushion Mold

The first part of the production process of the air bladder is necessarily the manufacturing of the mold for the polymer's casting. The design must take into account the necessity of being able to take the manufactured shell away from the mold; in addition, as the manufacturing process involves the use of the vacuum chamber in order to take all of the air bubbles away from the uncured polymer, the mold must be provided with vents. The last consideration is that the shape of the mold must ensure the positioning of the two parts, so that the thickness of the shell is accurately constant. Figure 9 shows the design of the molds; the cushion is made from a top and bottom half and bonded together. The 3D model of the two piece mold was drawn in SolidWorks.

In the configuration by Zampierin et al. [6], the cushion was created separately from the tube (Tygon S3 laboratory tubing [40]), and then the cushion and tube were sealed together.

Figure 9 - Bottom (a) and top (b) half of the old mold, and the mold assembly c).

The outlet of the cushion bladder was connected to a pressure sensor through a Tygon tube that was bonded with a sealant. However, the sealant that bonded the tube and the cushion was not reliable enough for our needs and would regularly leak air, causing the cushion to deflate. When the cushion deflated, the air pressure inside the bladder would change and the signal with it; therefore, the cushions would have to be repaired regularly in order to maintain their accuracy and usability. This regular maintenance was costly in terms of time, and would lead to frustration and setbacks for users. To remedy this, I redesigned the previous cushion mold to now include a tube attached to the cushion bladder. By casting the cushion and the tube as one piece, there was no more need for the addition step of sealing, as well as no more risk of human error in regards to the sealing, which drastically reduced the number of repairs needed for a successfully fabricated cushion.

The mold was 3D printed in0house from a Fortus Stratasys 250mc [41] and made out of ABS (acrylonitrile butadiene styrene) [42]. The cushion bladder material was directly cast into the 3D printed mold. The mold's shape was altered from its previous version by extending a tube section of the 3D-printed mold from the bladder outlet, in order to have the tube and bladder molded as one piece. The uncured liquid PDMS, in a 10:1 ratio mixture of the bulk and hardening materials which has been degassed to expel any bubbles in the mixture, is poured into the bottom mold, and then covered by the top mold to create the assembly as seen in Figure 10.

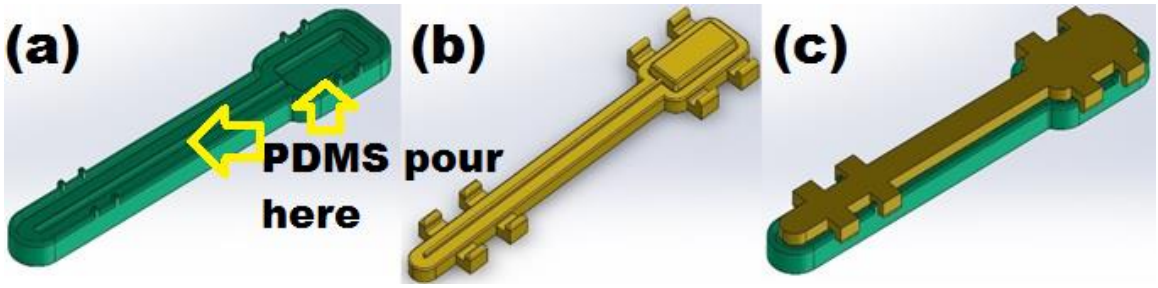

Figure 10 - Bottom (a) and top b) half of the new mold, and mold assembly (c).

The assembled mold with the PDMS is placed into the oven to be cured. After curing, and waiting 30min until the assembly had time to cool down to room temperature, the top mold would be separated from the bottom mold, and the cured PDMS would be delaminated the mold.

4.3. System Components

The structure of the wrist brace exoskeleton was made by Zampierin et al. [6] . The size and shape of the wrist brace exoskeleton was made to fit the author's forearm and be able to measure the perpendicular isometric forces and torques from the forearm onto the cushions. The dimensions of the wrist brace exoskeleton were made to fit two cushions under the forearm, two cushions above the forearm, and one cushion on each side of the forearm, as seen in Figure 12. The structure is simple and comprised of two parts, with a shaft acting as a hinge and another one acting as a locking pin. This configuration keeps the manufacturing costs low by simplifying the 3D printing process and limiting the amount of material needed to produce the exoskeleton. Similar to the cushion's mold, the wrist brace exoskeleton was 3D printed in-house (Fortus 250mc, Stratasys Ltd. MN, USA) [41] out of ABSplus plastic [42]. A 3mm diameter stainless steel rod was used as a pin joint hinge, and threaded screws we attached to the sides and bottom surface for mounting purposes during the experimental testing phase, as seen in Figure 11.

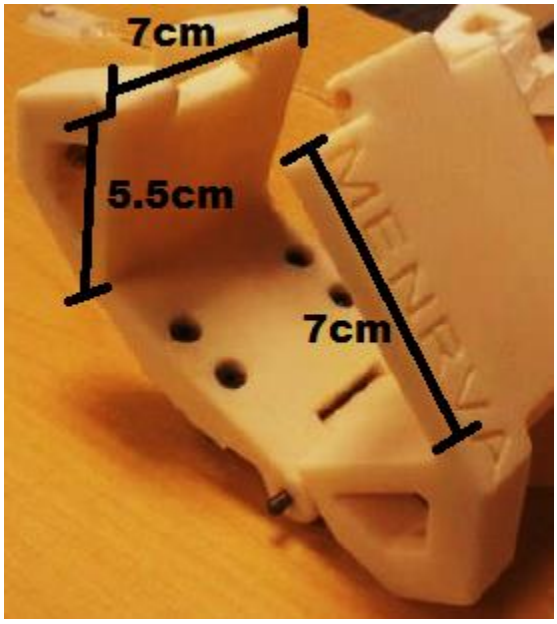

Figure 11 - 3D printed exoskeleton wrist brace.

The wrist brace exoskeleton configuration allows for the forearm movements inside to be captured by the six mounted polymeric force cushions through the pressure sensor circuit by converting the air pressure inside the cushions into electrical signals. The data acquisition card receives the signals from the pressure sensor circuit and then sends them to the LabVIEW program (National Instruments Corporation, Austin, TX, USA) on the computer to be processed and recorded, of which the data can be plotted and analyzed offline, as seen in Figure 12.

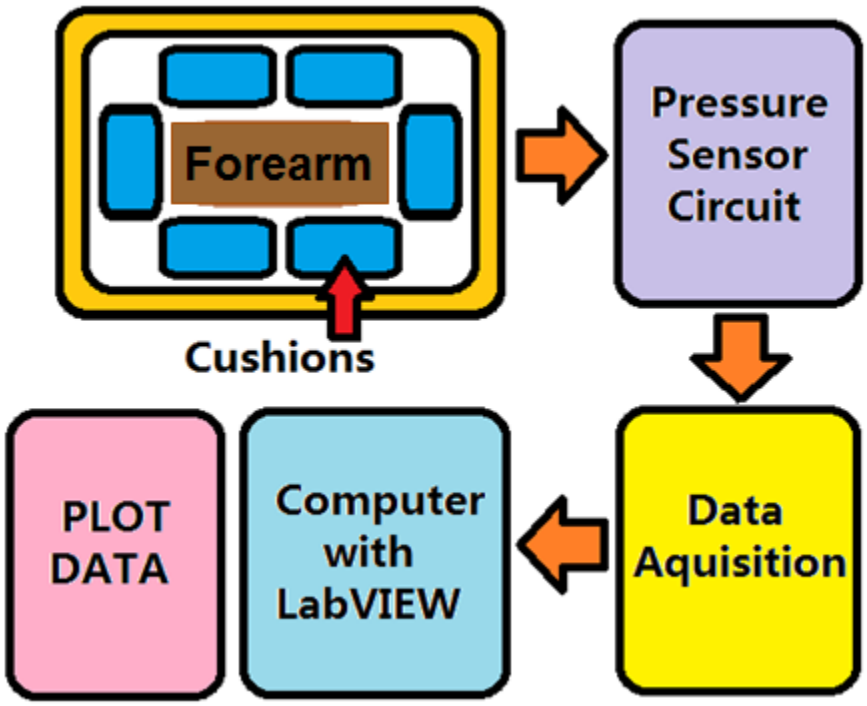

Figure 12 - Complete wrist brace exoskeleton system.

4.4. Cushion Fabrication and Air Leak Test

In the previous set of cushions made by Zampierin et al. [6], one problem that was found was that the 3D printed ABS plastic mold adheres to the PDMS during the curing process. A functionalization step of the surface of the mold was performed in order to prevent the PDMS from sticking to the ABS plastic. This functionalization step was performed through heat deposition of fluoro-silanes salts and allowed the PDMS to be formed with the mold, and easily detachable from the mold. Due to a lack of accessibility to the facilities required to functionalize the ABS plastic with fluoro-silanes salts, a less toxic and more time efficient method was used, where a light coat of acetone was brushed onto the surfaces of the mold in order to melt the porous areas and deterring the PDMS from bonding onto it.

The following procedure was convenient and feasible to use with the available equipment in our lab for rapid prototyping. The fabrication process below was the one

used by Zampierin et al. in his thesis [6], which was replicated for manufacturing the new cushions, with the exception of not sealing the tube separately to the bladder and not gluing Plexiglas to the top of the cushions. The rational for having the top of the cushion to be rigid, was in order to have a uniform pressure and displacement onto the cushions. Although, since the whole cushion top is being compressed by the forearm uniformly, the need for a rigid top is unnecessary. Finally, a laser cutter was used in order to trim and seal the cushions, whereas Zampierin et al. simply used a knife which did not seal the sides of the cushion bladder.

1) The uncured materials of the Dow Corning Silicone Elastomer [43] were poured on a scale and mixed. The PDMS polymer was made of two fluids: the main bulk component and the curing/hardening agent. The uncured PDMS materials were prepared at a 10:1 ratio of the bulk and hardening agent.

2) The now-mixed PDMS was stirred and poured into the bottom part of the mold, and then the top and bottom mold pieces were fitted together to form the mold assembly.

3) The mold assembly with the PDMS was placed in vacuum chamber, and were degassed of air bubbles for 30 minutes at 80kPa. Then, once the materials had been degassed, the PDMS was placed in an oven for three hours to cure at 80^{o}C.The mold assembly with the cured PDMS was set outside the oven to cool down to room temperature. After cooling, the PDMS was carefully delaminated from the mold, and forming the top shell of the cushion bladder. Figure 13 shows the top cover of the cushion bladder's fabrication steps.

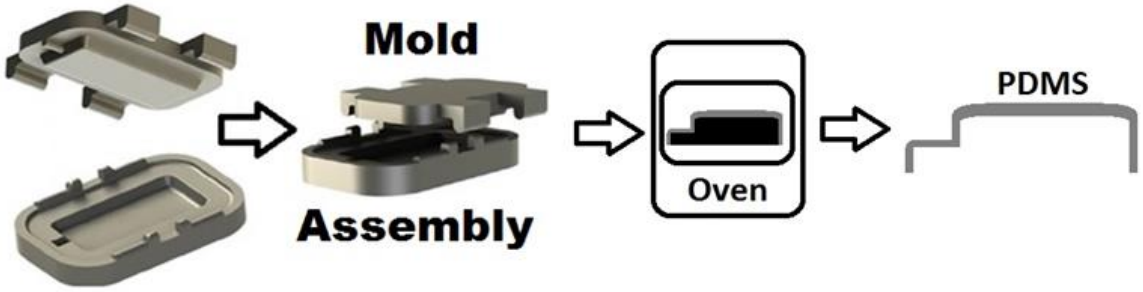

Figure 13 - Cushion's top cover fabrication using the assembly mold.

Note that this mold has an open outlet to expose the cushion bladder to atmospheric air before when a separate Tygon tube [40] would be inserted. Although with the new mold, the tube and the bladder are molded as one unit with no need for a separate tube.

4) A thin layer of uncured PDMS, which was spread on a plate of Plexiglas with rectangular walls to form the bottom cover of the cushions. The PDMS bottom cover which will become the cushion's base, is prepared following the same steps as above. Figure 14 shows the steps for fabricating the base.

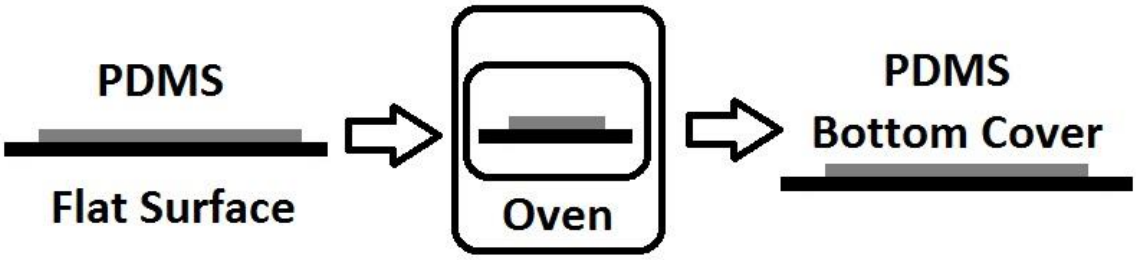

Figure 14 - Bottom cover fabrication using a flat Plexiglas plate.

5) The top cover is then glued to the PDMS bottom cover, using some uncured PDMS between the interfacing surfaces of the top and bottom of the cushion parts.

6) The uncured layer of PDMS between the top and bottom covers, underwent a cycle of degassing in the vacuum chamber for 30 minutes at 80^{o}C. Once the degassing was complete, the top and bottom layers were bonded by curing in the oven for another three hours at 80^{o}C. The steps for the cushion assembly are shown in Figure 15.

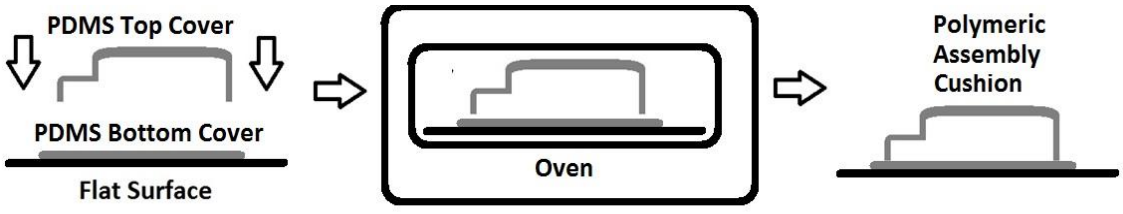

Figure 15 - Combined cushion assembly.

The resulting cushions are 50 x 20 x 6.5mm^3 and has a bladder cushion with atmospheric pressure air inside.

7) Finally, the cushion was laser cut in order to remove the excess PDMS, as well as to further bond the pieces together.

8) To make sure that the cushion was fully sealed, a leak test was performed after it was laser cut. The cushion was submerged under a cup of soapy water; if no bubbles formed, then the cushion did not have a leak and was therefore well sealed. However, if bubbles did form, or if an unusual deflation occurred when holding the end of the tube and then lightly pressing onto the top of the cushion, as seen in Figure 16, then uncured PDMS that had been mixed and degassed was poured onto the suspected leakage sites and cured in the oven for at 80^{o}C another three hours.

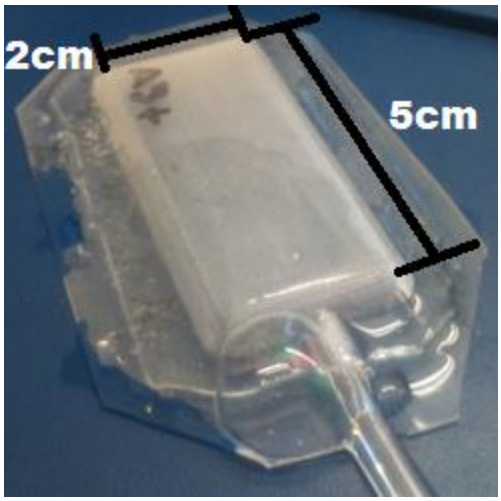

Figure 16 - Leak test of a cushion showing a bubble leak using soapy water.

4.5. CO_2 Laser Cutting of Cushion

The bonded bottom and top cushion covers, which form the cushion bladder of the newly configured cushions, had excess PDMS around the edges of the cushion. These edges were cut by a CO_2 laser cutter using the Versa Laser System 3.60 (LST Group. 109 Bonds Road, Punchbowl NSW 2196, Australia) [44] at Simon Fraser University's Engineering Science Lab. By doing this, the cushions would have identically shaped edges that fit well on the wrist brace exoskeleton. The outline of the cushion and its tube was drawn in Corel-Draw 2015 (Corel Corporation, Ottawa ON, Canada) [45] with the

required settings necessary for the laser cutter program to use, and then laser cuts the along outline as seen with the before and after in Figure 17.

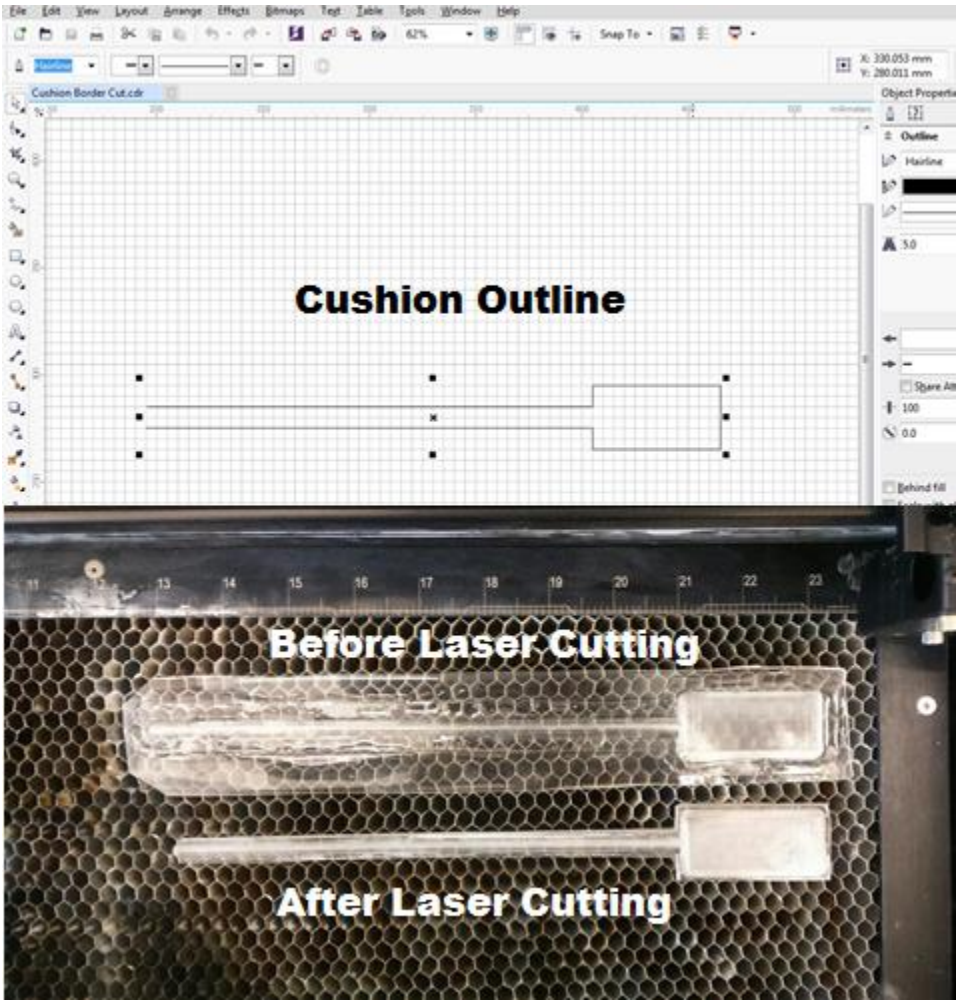

Figure 17 - CorelDraw outline of the cushion, with before and after laser cutting.

The laser cutter was set to the following settings: Power 30%, Speed 5%, PPI 500, while cycling 15 times around the cushion outline. It is important to note that the outline in CorelDraw be set to hairline and that the colour of the line be pure RGB. These settings were experimentally found, with reference to the Laser Cutter User Manual written by Alavi et al. in 2009, which was revised by Alavi et al. in 2014 [46], to cut the PDMS while conserving the power of the laser cutter. The laser cutting of PDMS has been safe to work with and has been common practice in various publications in microfluidic lab-on-a-chip applications [47] [48] [49]. The heat of the laser also helped to fuse the edges of the top

and bottom cushion covers along its outside perimeter. A black charred residue was left along the cut edge of the cushion, but this was carefully scrapped off and disposed, along with the excess PDMS material.

4.6. Electronics of Sensing Unit

The pressure sensor had to fulfill three main requirements: its dimensions needed to be kept small to minimize the system's overall size, it has to be easily be able to connect to the cushion's tube, it had to be able to sense the expected pressure changes, as well as being a low cost sensor. From the options of available air pressure sensors, the Freescale Semiconductor MPXV7007DP, integrated silicon pressure sensor on-chip signal conditioned, temperature compensated and calibrated, was chosen to be the differential air pressure sensor for this study [50].

The sensing unit is composed of the cushion bladders and the integrated circuit (IC) pressure sensors. The IC pressure sensors were chosen to be differential sensors to measure the cushion's movements in pairs. The pin-out is labled as the following: pins 1, 5, 6, 7, and 8 are not connected, pin 2 is +5V, pin 3 is ground, and pin 4 is the output voltage shown in Figure 18.

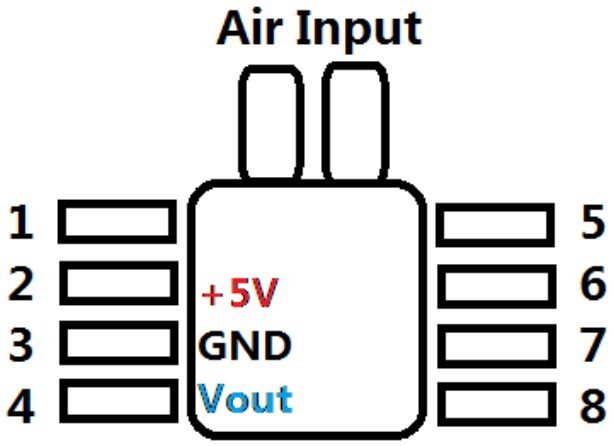

Figure 18 - Differential pressure sensor pin out.

This was changed from the previous work done by Zampierin et al. [6], where before six individual gauge pressure sensors [51] were used for a single cushion. In the new cushion sensing configuration, only three differential pressure sensors are used, instead of six indivisual ones, which reduces the cost and complexity of the equiptment, as well as reducing the clutter of connections of wires and tubes, when using the exoskeleton wrist brace. The differential pressure sensors are each connected to two cushions that are mounted on the exoskeleton wrist brace. The cushions that are connected to their respective IC differential pressor sensors were chosen to allow the pairs of cushions to move in alternating diretions when subjected to various arm movements when inside an exoskeleton wrist brace.

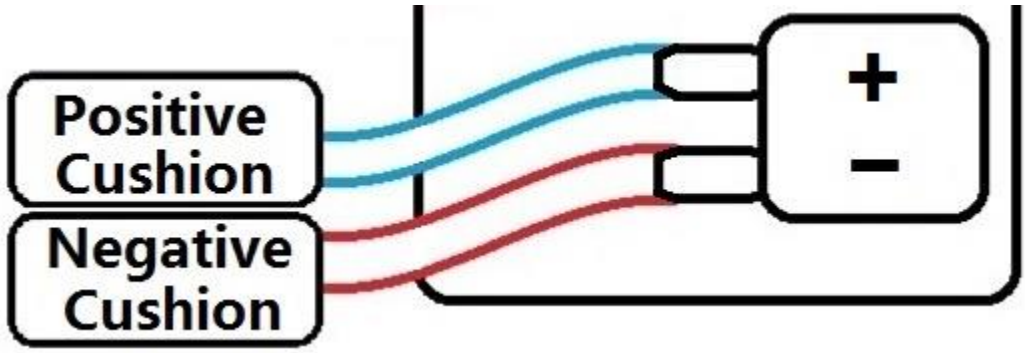

Figure 19 - Differential pressure sensor and positive / negative cushions.

The IC pressure sensor reads the pressure from the cushions and registers an output signal as a positive or negative analog signal from a data acquisition board. The IC differential pressure sensors are connected to an electronic circuit, as perscribed by the manufacturer [51]. The electronic circuit of each sensing unit, along with the pin assignment of the pressure sensor, and the 0.01uF, 1.0uF, and 470pF capacitors, are shown in Figure 20.

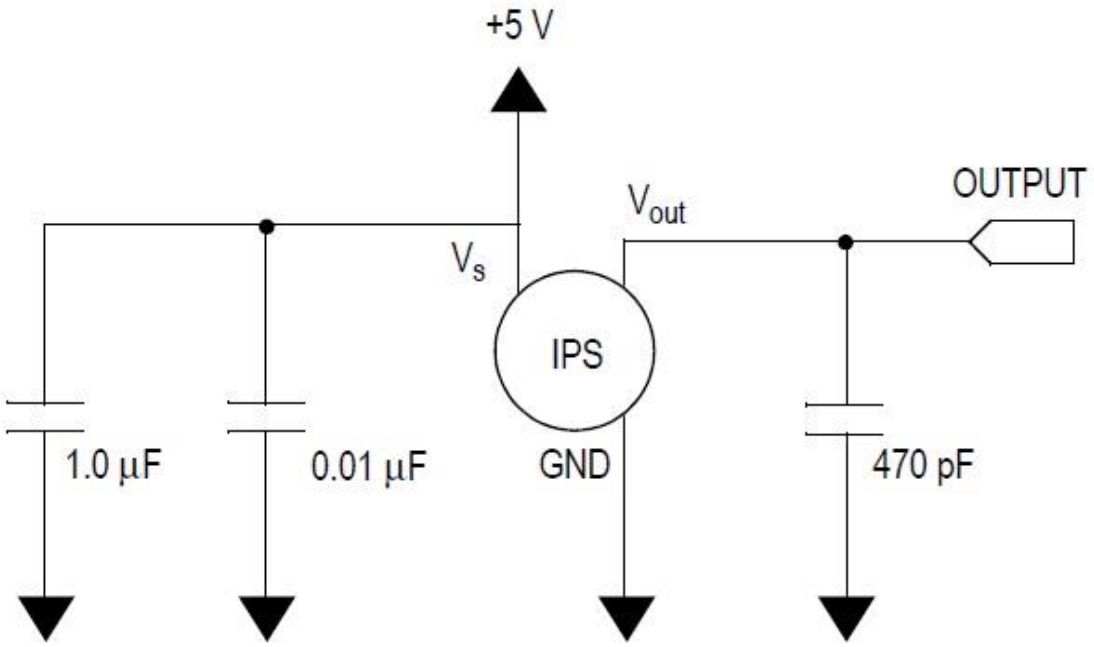

Figure 20 - Pressure sensor datasheet electronic circuit schematic [50].

From to the configuration of the cushions as shown in Figure 12, six cushions were made into three cushion pairs, each with a differential pressure sensor. The electronic circuit for all three pressure sensors were implemented on a breadboard for each pressure sensor, and connected to a data acquisition board below it, as seen in Figure 21, to be read and processed by a LabVIEW program.

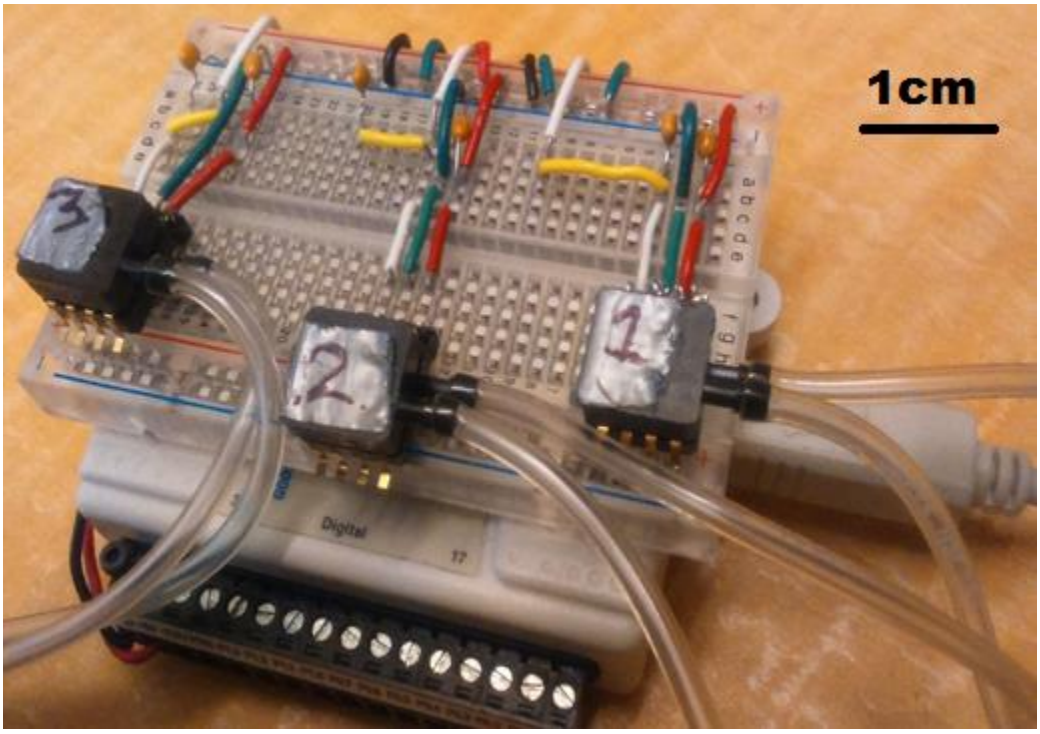

Figure 21 - Pressure sensor circuit and DAQ with three pressure sensors.

4.7. Summary

The cushions presented in this thesis are made entirely of Sylgard 184 10:1 PDMS. This material was chosen for its flexibility, good step response characteristics, low cost, and ease of access for manufacturing. The six cushions were able to accommodate the size of the wrist brace exoskeleton, while maintaining contact with the forearm.

The cushion mold made by Zampierin et al. was altered to have the bladder and tube as one unit, as opposed to having to attach and seal an external tube onto the bladder after the cushion had been cured. A new 3D printed mold was manufactured in order to cast the new desired cushion configuration. The wrist brace exoskeleton can be opened and closed with a hinge, and can be locked with a pin very easily with one hand. The configuration of the cushions was made to fit the wrist brace exoskeleton to capture various isometric forearm motions, particularly forearm pronation/supination (rotation), elbow flexion/extension (up/down), and shoulder internal/external rotation (left/right). The torques and forces from the arm onto the wrist brace exoskeleton were measured through

these cushions. The signals from the pressure sensors that picked up the changes in air pressure from the cushions were read by the data acquisition card, which sent the signals to the LabVIEW program that then plotted the isometric forces from the forearm movements.

The cushions are fabricated using a process very similar to the one used by Zampierin et al. [6], with some differences. These include the use of acetone to melt the porous surface and allow easier delamination of the cushion from the ABS plastic mold, removing the need for a separate tube while having the cushion and tube be made as one uniform piece, as well as not using a Plexiglas top piece for evenly distributing applied forces, and using a CO_2 laser cutter to trim the cushions and further bond the top and bottom bladder covers along the cushion outer perimeter. The gauge pressure sensors that were originally used for a single cushion, have been replaced by a differential pressure sensor that monitors two cushions at once; this reduces the cost and hardware necessary to create the system.

Chapter 5. Finite Element Model

Objective 2 is partly covered by Chapter 5. This chapter is dedicated to the finite element models of the cushion, aluminum plate, and glass tube, involved in the simulation of the compression of the cushion. The model of the cushion, and its simplifications, is described. The meshing, element types, materials, and boundary conditions of the simulation are also described. The results of the simulations are presented at the end of the chapter, which then leads to the next part of Objective 2 the following chapter.

5.1. Cushion Model Simplification

In order to accurately understand the behaviour of the proposed cushion, due to the complexity of the combined behaviour of the air compression inside the cushion and the PDMS material, a finite element model was created using ANSYS Mechanical APLD 14.0 [52]. The geometry of the cushion was drawn and represented by a simplified rectangular chamber that is divided in half along the x-axis of symmetry, producing a 50 x 10 x 6.5mm^3 half cushion bladder volume, with a narrow rectangular half cushion tube volume of 220 x 1.5 x 3mm^3, connected to the main chamber. The cushion chamber was modeled to contain air which behaves as an ideal gas, at standard atmospheric pressure and a standard room temperature of 25°C. The finite element model was created using a script that was written from the ANSYS command line codes. The cushion was not analyzed using a non-linear model such as the Ogden or Mooney-Revlin, since the deformation of the Sylgard 184 PDMS [43] was within the linear region of its stress-strain curve and elastic modulus-strain curve [53].

5.2. Cushion FEM with Flat Aluminum Plate

A flat surface was drawn to represent a solid object that pressed onto the top surface of the six cushions. This flat surface was modeled with rigid material properties similar to an aluminum block, which can be experimentally tested by attaching an aluminum block to a linear stage. As the flat surface was pressed onto the cushion, the pressure of the contained air would increase due to the reduction in volume of the chamber. The solid

volumes of the cushion and aluminum plate model in ANSYS Mechanical APDL 14.0 are shown below in Figure 22.

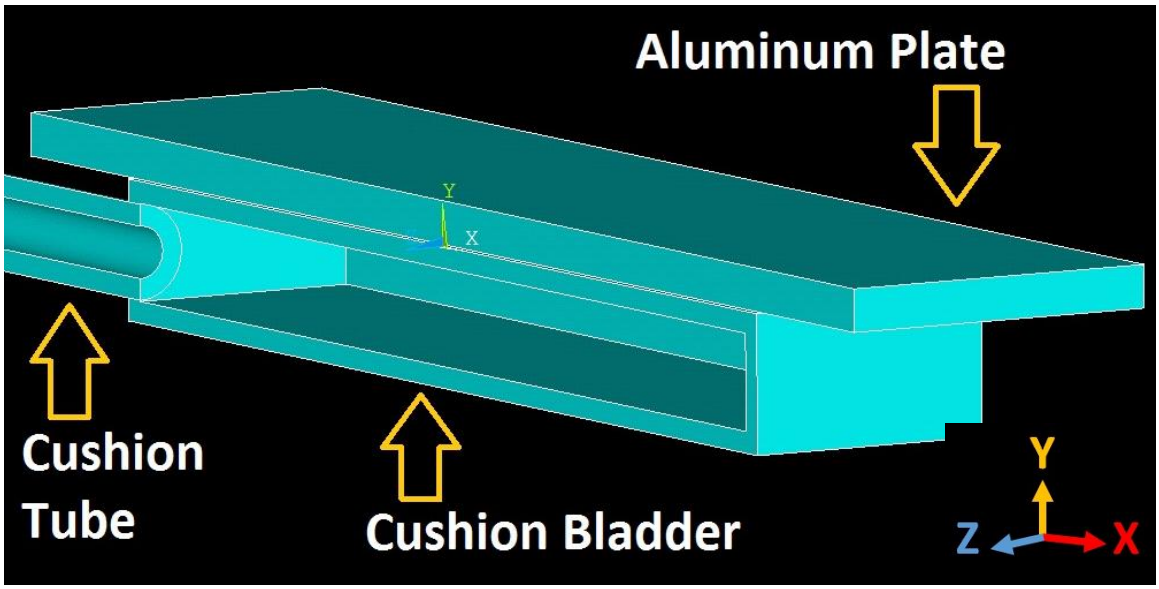

Figure 22 - Cross-section view of the cushion tube, bladder, and aluminum plate.

5.2.1. Meshing and Surface Mapping

The mesh of the PDMS material and the aluminium plate was made of 93,579 and 13,196 SOLID285 elements respectively. There were 17,712 HSFLD242 elements that represented the air, which connected to a node of the inner walls of the cushion and the central pressure node, which was located at the geometric centre of the cushion chamber. There were 2,581 TARGE and CONTRA elements meshed on the surfaces of the cushion and the aluminium block that would come into contact and push against each other. The tetrahedral elements were chosen to be 1mm in size to allow for at least two layers of elements along the thickness of the aluminium plate, with a total number of meshed elements being 124,487, as seen in Figure 23.

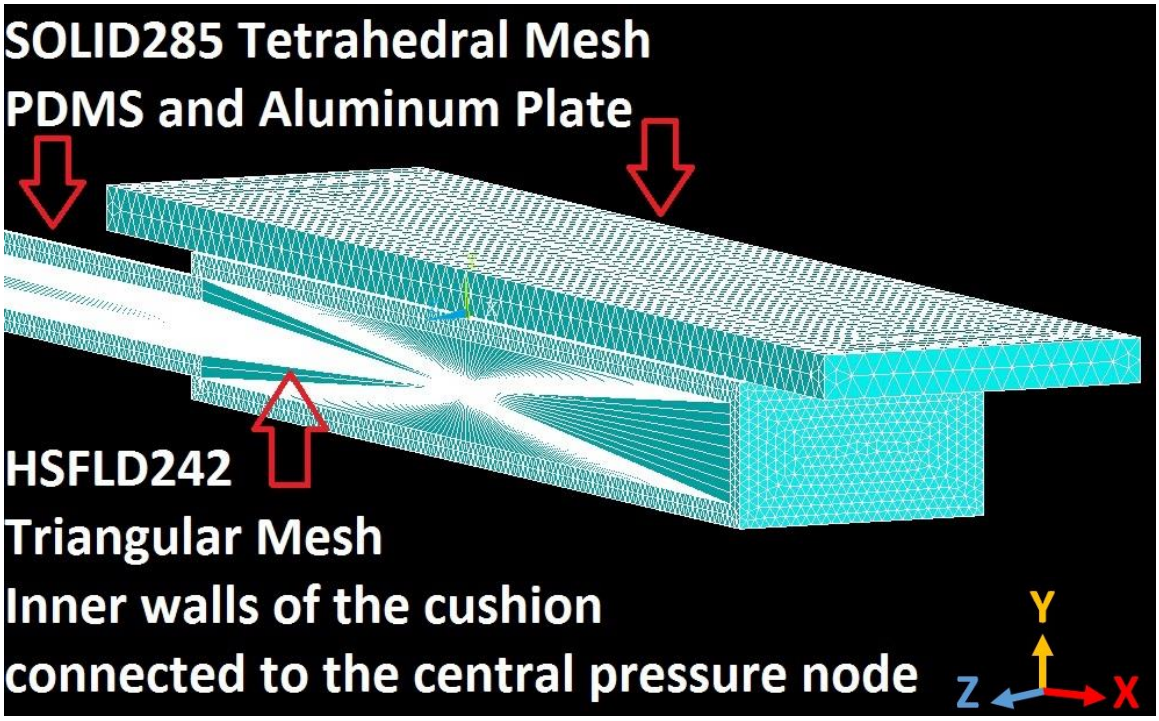

Figure 23 - Elemental Meshing of the solid and air elements.

The white cross that is seen in the middle of the cushion is due to the geometry of the cushion mesh having a higher concentration of HSFLD242 elements connecting the inner walls of the cushion to the central pressure node. A transparent view of the meshed air elements is shown in Figure 24 and Figure 25.

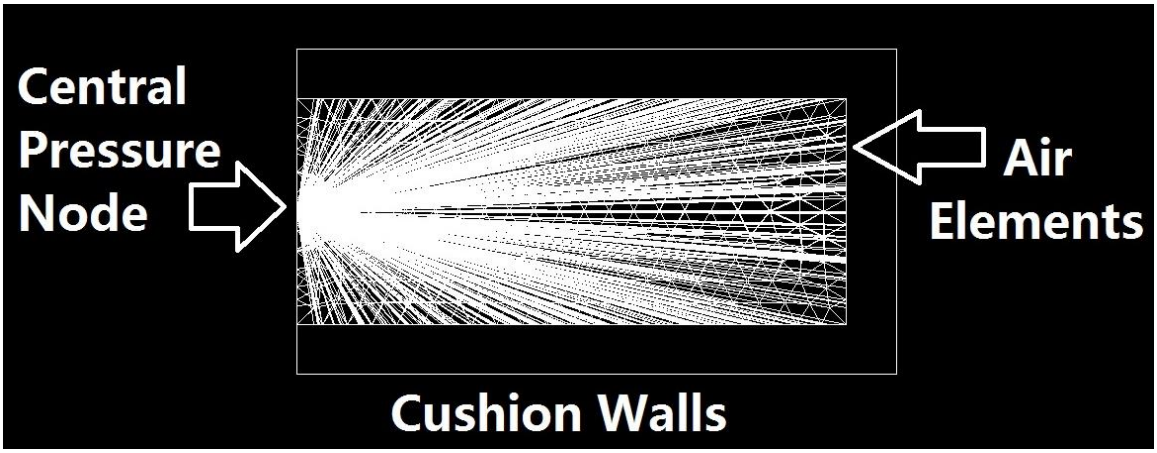

Figure 24 - Transparent meshed air elements in the cushion bladder.

This meshing type can also be seen at the end of the cushion tube, where the horizontal lines are the air elements connecting the inner walls of the tube back to the central pressure node. The hashed triangular pattered is the meshed PDMS walls of the cushion. The tube end was meshed and enclosed to model the tube being connected to the IC differential pressure sensor as seen in Figure 25. In order to settle on a result from the FEM computational solution, the result needed to have mesh independence, where the solution would not change significantly while the size of the mesh elements would reduce. The mesh size of the polymeric cushion was reduced small enough to converge well and give a solution that would be within 2% of the previous element size. Further refining the mesh to smaller element sizes would not converge to find a solution and would require further computational power.

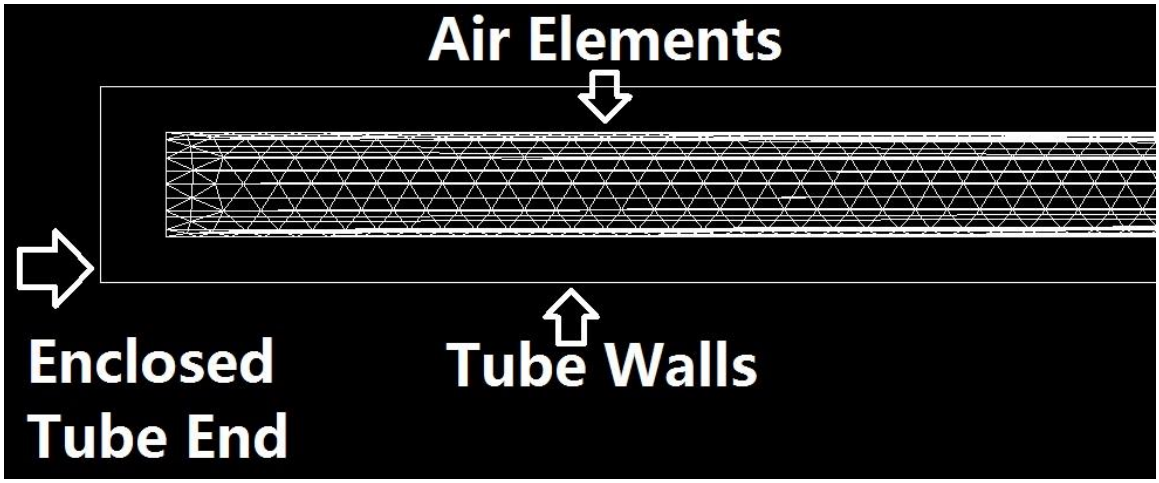

Figure 25 - Transparent meshed air elements at the end of the tube.

5.2.2. Element Types and Materials

The elements used to model the cushion system were chosen for their properties and function. In order to model an air cushion undergoing a physical deformation due to contact with an external object, there had to be particular elements to represent the cushion material, the object that contacts the cushion, the air inside the cushion, as well as particular surface elements for the two objects to come into contact with each other. In order to simulate the air contained inside the cushion, a specific element was chosen; the three-dimensional hydrostatic fluid element, HSFLD242 [52]. This element was introduced in 2010 by ANSYS to model the effect of a pressure loading on a contained fluid. As the fluid's volume or temperature changes, the pressure exerted on the walls of the structure will change. It was not possible to accurately model this type of relationship with a regular fluid element due to its linear stiffness relationship, such as FLUID79/80, in ANSYS Mechanical APDL or user subroutines [54]. The HSFLD242 [52] elements do not need to be meshed in a typical way inside the container, where single lines connect the nodes on the inner walls of the chamber to the shared central 'pressure node', in order to model the change in volume of the cushion and result in a measureable uniform pressure. In the model used in this paper, the central pressure node was placed at the geometric center of the rectangular cushion chamber. The structural element used to model the cushion's PDMS material was SOLID285 [52], which is a three-dimensional tetrahedral element. This element was chosen because of its compatibility with the hydrostatic fluid elements

used to model the air inside with cushions. The model was drawn and meshed with their respective elements and materials as seen in Figure 26.

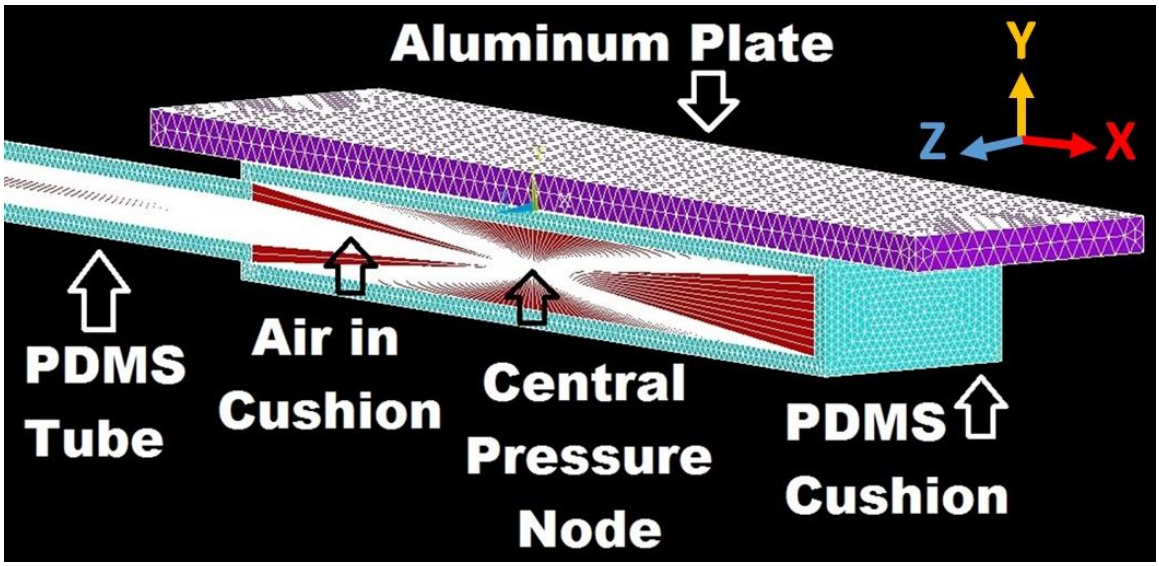

Figure 26 - FEM model materials of the cushion.

In order for the flat surface and the cushion surface to come into contact with each other and interact with respect to their physical properties, contact and target elements were used on the top surface of the cushion and the bottom surface of the flat surface. Since this model was created to simulate a three-dimensional structure, the CONTRA170 [52] and TARGE174 [52] elements were used, and are indicated by the red surface as seen in Figure 27.

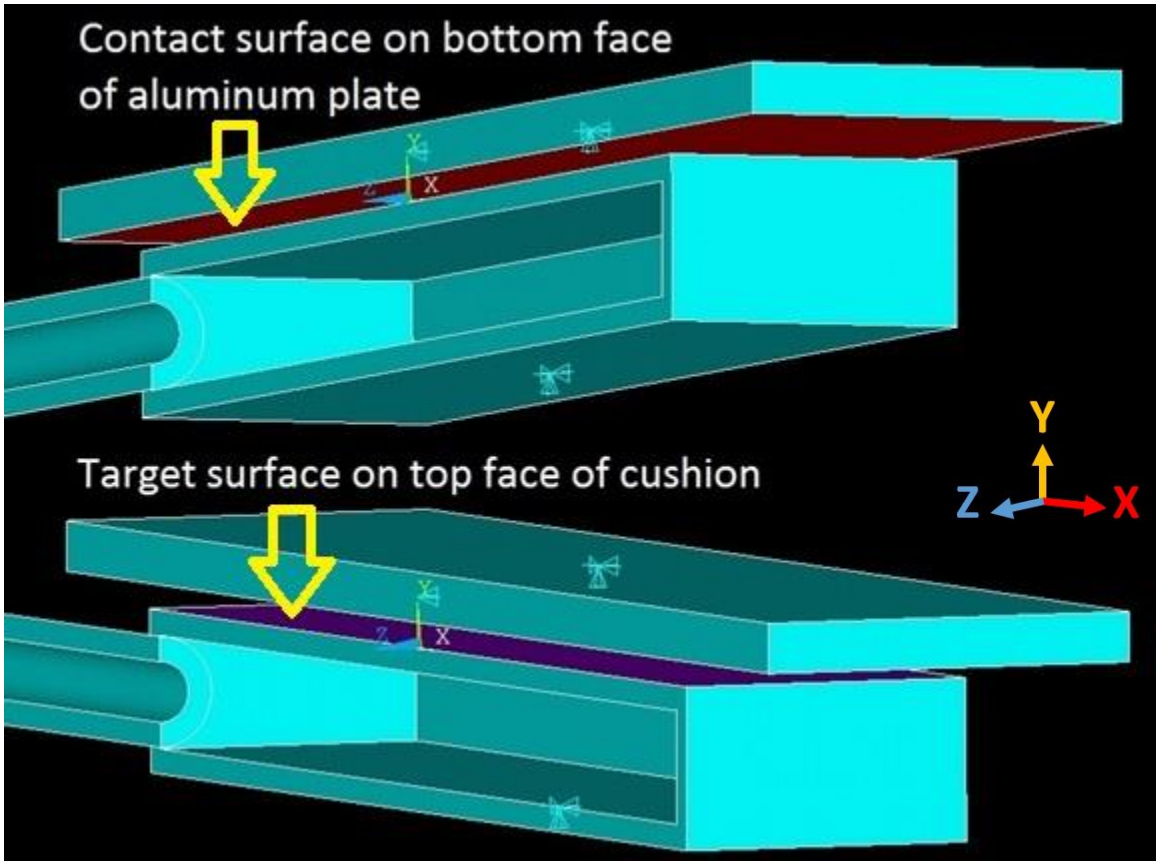

Figure 27 - Target and contact elements on the cushion and aluminum plate.

5.2.3. Boundary Conditions

The boundary conditions applied on the cushion were made to simulate the cushion's behaviour, and account for simplifications of the model. The bottom surface and outer end of the air tube were fixed in place to represent the cushion being placed on a rigid surface, and the end of the air tube was attached to the inlet of the IC pressure sensor. The top surface of the flat plate was given a displacement value that would simulate the flat surface pushing on the top surface of the cushion. ANSYS Mechanical APDL displaces the quarter sphere onto the cushion to compress it, where then the elements representing the air inside the cushion are compressed, and so the results show a final change in pressure. Finally, in order to simplify the model and save computational processing time, the model was split in half along the axis of symmetry down the length of the cushion, the air tube, and the flat plate. The symmetrical boundary plane of the model was free to move in the horizontal and vertical X and Y-axis but kept at the initial zero

position along the perpendicular Z-axis. The boundary conditions of the cushion were made to simulate cushion's physical limitations, as seen in Figure 28.

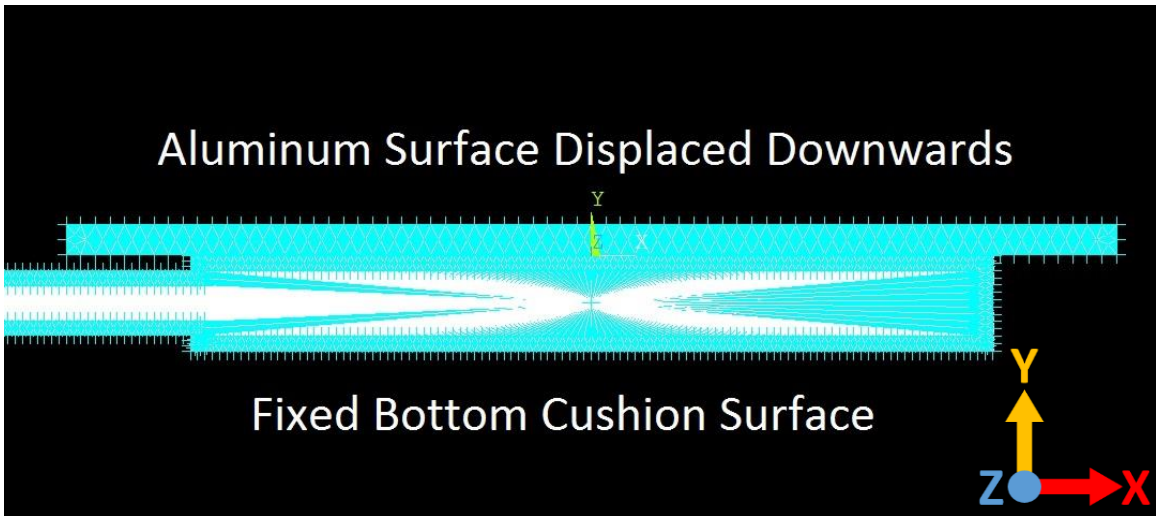

Figure 28 - Polymeric Cushion with Aluminum Plate Boundary Conditions.

5.2.4. Finite Element Solution

The central pressure node was measured after the aluminium plate was lowered by a set distance of 0.2mm, in 50µm step increments, onto the top surface of the cushion and pushed down to compress the cushion. As the top of the PDMS cushion was pressed by the flat surface, the inner volume of the cushion's bladder was reduced, which compressed the air inside the bladder and increased the pressure from its initial atmospheric pressure. The ANSYS parameters and settings are set such that the analysis type was a Static Analysis, and large deflection was turned on. The number of sub-steps was set to be 20, and auto time-stepping was turned on, with the maximum and minimum number of sub-steps being 100 and 20 respectively. These resulting displacement, force, and output pressure relationships are compared to the experimental results in Chapter 6.

5.3. Cushion FEM with Quarter Sphere Glass Tube

A quarter sphere was drawn to represent a solid object that pressed onto the top surface of the cushion. This quarter sphere was modeled with rigid material properties

similar to the end of a glass tube, which can be experimentally tested by attaching a glass tube to a linear stage. As the glass tube was pressed onto the cushion, the pressure of the contained air would increase due to the reduction in volume of the chamber. The solid volumes of the cushion and glass tube model in ANSYS Mechanical APDL 14.0 are shown in Figure 29.

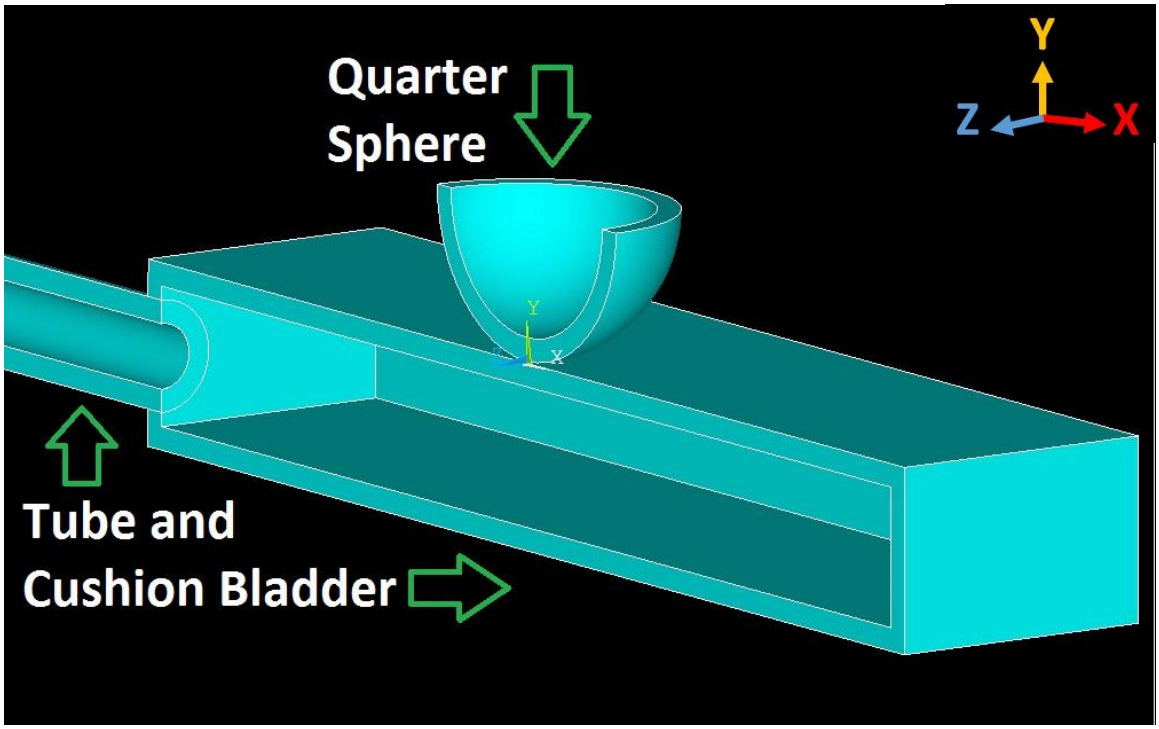

Figure 29 - Cross-section view of the cushion tube, bladder, and quarter sphere.

5.3.1. Meshing and Surface Mapping

The mesh of the PDMS material and the quarter sphere was made of 93,579 and 6,591 SOLID285 elements respectively. There were 17,712 HSFLD242 elements that represented the air, which connected to a node of the inner walls of the cushion and the central pressure node, which was located at the geometric centre of the cushion chamber. There were 2,581 TARGE and CONTRA elements meshed on the surfaces of the cushion and the aluminium block that would come into contact and push against each other. The tetrahedral elements were chosen to be 1mm in size to allow for at least two layers of elements along the thickness of the aluminium plate, with a total number of meshed elements being 124,487, as seen in Figure 30.

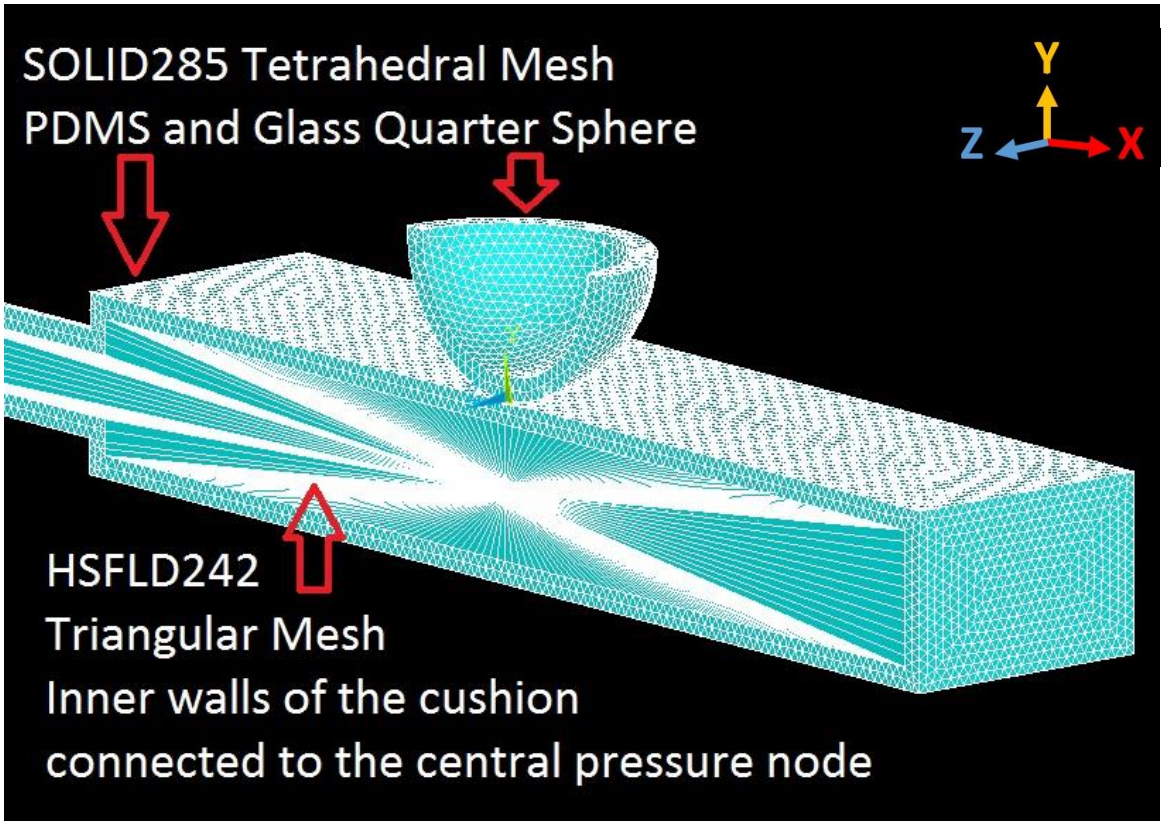

Figure 30 - Elemental Meshing of the solid and air elements.

The white cross that is seen in the middle of the cushion is due to the geometry of the cushion mesh having a higher concentration of HSFLD242 elements connecting the inner walls of the cushion to the central pressure node.

5.3.2. Element Types and Materials

The elements used to model the cushion system were chosen for their properties and function. In order to model an air cushion undergoing a physical deformation due to contact with an external object, there had to be particular elements to represent the cushion material, the object that contacts the cushion, the air inside the cushion, as well as particular surface elements for the two objects to come into contact with each other. In order to simulate the air contained inside the cushion, a specific element was chosen; the three-dimensional hydrostatic fluid element, HSFLD242 [52]. As the fluid's volume or temperature changes, the pressure exerted on the walls of the structure will change. It was not possible to accurately model this type of relationship with a regular fluid element

due to its linear stiffness relationship, such as FLUID79/80, in ANSYS Mechanical APDL or user subroutines [54]. The HSFLD242 [52] elements do not need to be meshed in a typical way inside the container, where single lines connect the nodes on the inner walls of the chamber to the shared central 'pressure node', in order to model the change in volume of the cushion and result in a measureable uniform pressure. In the model used in this paper, the central pressure node was placed at the geometric center of the rectangular cushion chamber. The structural element used to model the cushion's PDMS material was SOLID285 [52], which is a three-dimensional tetrahedral element. This element was chosen because of its compatibility with the hydrostatic fluid elements used to model the air inside with cushions. The model was drawn and meshed with their respective elements and materials as seen in Figure 31.

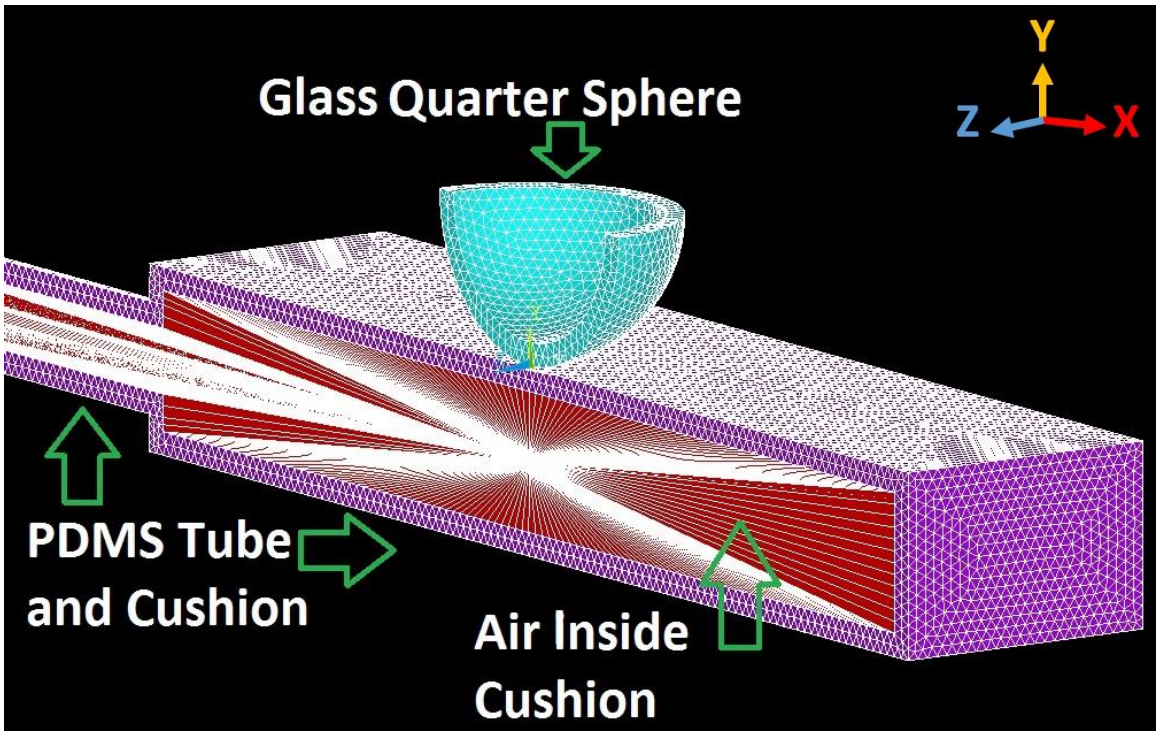

Figure 31 - FEM model materials of the cushion and quarter sphere.

In order for the quarter sphere and the cushion surface to come into contact with each other and interact with respect to their physical properties, contact and target elements were used on the top surface of the cushion and the bottom surface of the quarter sphere. Since this model was created to simulate a three-dimensional structure,

the CONTRA170 [52] and TARGE174 [52] elements were used, and are indicated by the red surface as seen in Figure 32.

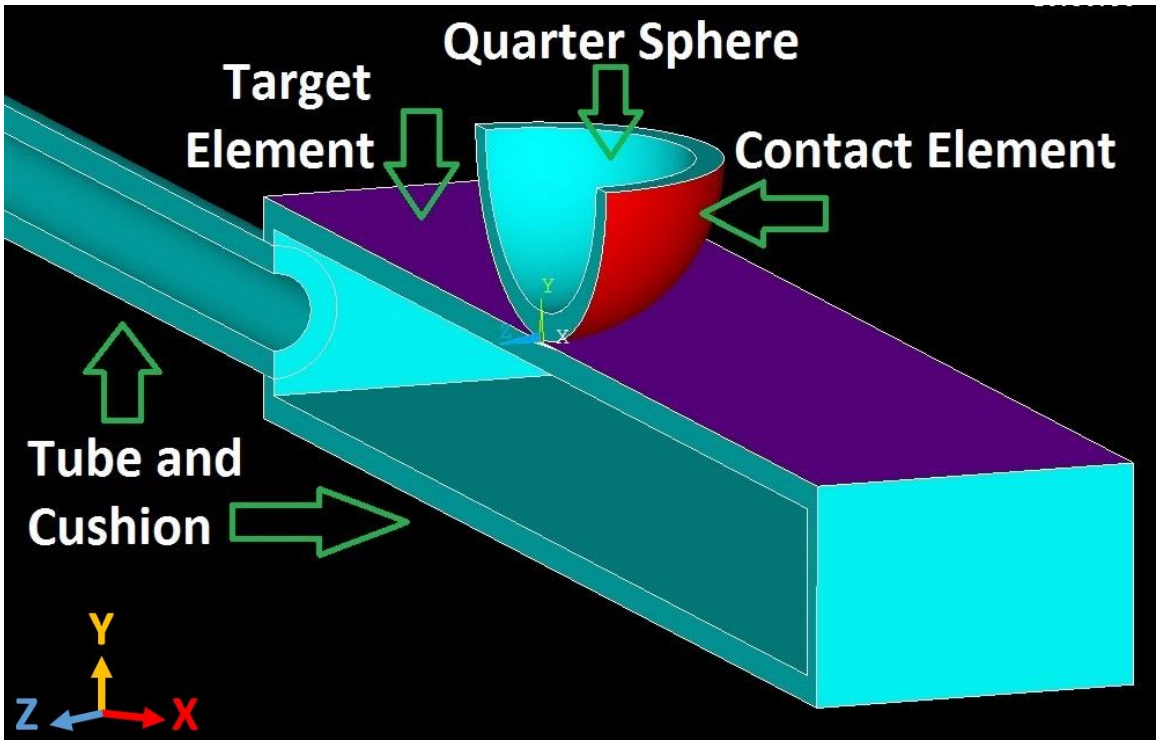

Figure 32 - Target and contact elements on the cushion and quarter sphere.

5.3.3. Boundary Conditions

The boundary conditions applied on the cushion were made to simulate the cushion's behaviour, and account for simplifications of the model. The bottom surface and outer end of the air tube were fixed in place to represent the cushion being placed on a rigid surface, and the end of the air tube was attached to the inlet of the IC pressure sensor. The top surface of the quarter sphere was given a displacement value that would simulate the flat surface pushing on the top surface of the cushion. ANSYS Mechanical APDL displaces the glass tube onto the cushion to compress it, where then the elements representing the air inside the cushion are compressed, and so the results show a final change in pressure. Finally, in order to simplify the model and save computational processing time, the model was split in half along the axis of symmetry down the length of the cushion, the air tube, and the quarter sphere. The symmetrical boundary plane of the

model was free to move in the horizontal and vertical X and Y-axis but kept at the initial zero position along the perpendicular Z-axis. The boundary conditions of the cushion were made to simulate cushion's physical limitations, as seen in Figure 33.

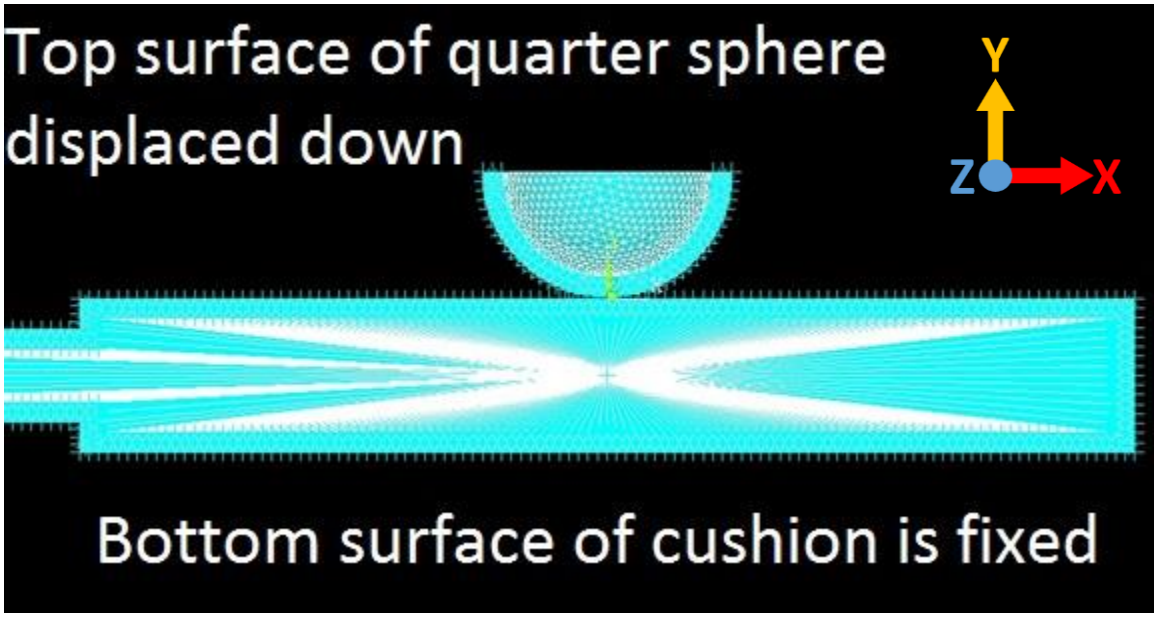

Figure 33 - Polymeric Cushion with Quarter Sphere Boundary Conditions.

5.3.4. Finite Element Solution

The pressure node was measured after the quarter sphere was lowered by a set distance up to 3mm, in 1mm step increments, onto the top surface of the cushion and pushed down to compress the cushion. An additional 3.88mm displacement point of the quarter sphere was made, in order to reach close to the full 4mm height of the cushion bladder, before the ANSYS simulation would not converge. As the top of the PDMS cushion was pressed by the glass tube, the inner volume of the cushion's bladder was reduced, which compressed the air inside the bladder and increased the pressure from its initial atmospheric pressure. The ANSYS parameters and settings are set such that the analysis type was a Static Analysis, and large deflection was turned on. The number of sub-steps was set to be 20, and auto time-stepping was turned on, with the maximum and minimum number of sub-steps being 100 and 20 respectively. These resulting displacement, force, and output pressure relationships are compared to the experimental results in Chapter 6.

5.4. Summary

The polymeric cushion's dimensions were simplified to be represented by a hollow rectangular prism. Half of the cushion was modelled, along its symmetrical x-z plane. The steps were done in order to conserve computational time. The outlet tube of the cushion was attached to the bladder, and represented by the same material properties using the SOLID285 element. The aluminum plate and glass tube were also meshed by the same SOLID285 element, but were assigned their respective aluminum and glass material properties. The SOLID285 element was chosen in order to model the cushion's interaction forces with the hydrostatic pressure of the air. The air inside of the cushion was modelled by the HSFLD242 element, which represents a uniformly distributed fluid pressure inside of a contained chamber, while applying pressure onto a single central pressure node. In order to simulate the aluminum plate and glass tube contacting and compressing the tube, the TARGE174 and CONTRA170 elements were mapped onto the top surface of the cushion and the bottom surface of the glass tube and aluminum plate, respectively.

The bottom surface of the cushion was fixed in the x, y, and z directions to keep the cushion in place. The end of the tube was also fixed in the x, y, and z directions to simulate the tube being press-fitted onto the pressure sensor. The symmetrical plane of the cushion was fixed in its normal z direction. The top surface of the cushion and the aluminum plate was displaced in order to facilitate the compression of the polymeric cushion.

Mesh independence was found where the solution of the FEM analysis converged properly and did not change more than 2%, before the solution would not converge and would require more computational power. These resulting force and output pressure relationships are compared to the experimental results in chapter 6.

Chapter 6. Experimental Testing

Objective 2 is partly covered by Chapter 6. This chapter is dedicated to the experimental testing of the cushion in order to evaluate its response to the input force and displacement in order to characterize the cushion's relation between the input force and the output pressure, as well as checking its repeatability and evaluating its depressurization rate. The experimental results of this chapter prepare for the comparison of the cushion's behaviour with the FEM results in the next chapter with respect to Objective 2.

6.1. Experimental Linear Stage Test Setup

The experimental testing of a fabricated polymeric cushion was done using a single test cushion for consistency. In order to accurately model the performance of the cushion with a controllable system, a linear stage (T-LS28-SMV, Zaber Technologies Inc., Vancouver, BC) [55] was used with a linear force sensor (LRF400 2.2lb, FUTEK Advanced Sensor Technology, Inc., Irvine, CA) [56] connected to a 7.2 x 3.1 x 3.1cm^3 aluminum block that covered the surface of the cushion, as seen in Figure 34. The linear stage was controlled by a LabVIEW program that raises and lowers the probe with a resolution of 100nm, reading the values of the linear force sensor due to the reaction force felt from the aluminum block on the cushion surface.

The polymeric cushion's air tube was used to channel air from the cushions bladder to the MEMS differential pressure sensor (MPXV7007DP, Freescale Semiconductor, Inc., Austin, TX) [57]. These MEMS differential pressure sensors sent the analog signals to a data acquisition board (USB-6009 DAQ, National Instruments, Austin, TX) [58] to be processed by the LabVIEW program.

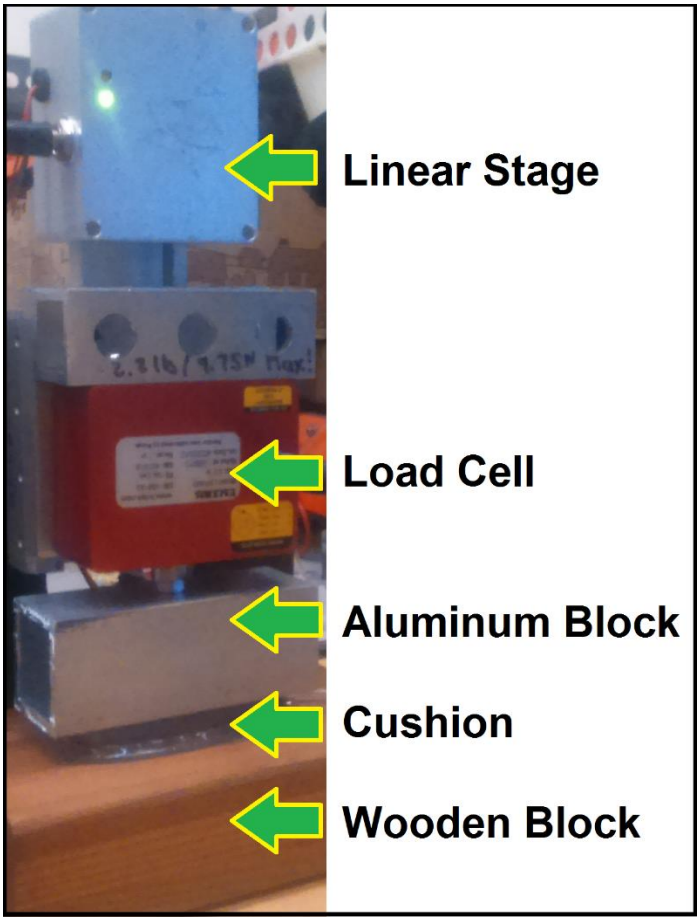

Figure 34 - Linear stage and load cell with aluminum block and test cushion.

The LabVIEW program controlled the linear stage to lower and retract the aluminum block in order to compress the cushion. A wooden block supported the bottom of the cushion during the linear stage test. Before performing this test, an air leak test was done on the cushion, where soapy water was applied on the outside of the cushion while manually pressing on the cushion's top surface. If no bubbles were observed due to the applied force, then the cushion was well sealed and used for further testing. If bubbles were detected, then the cushion was repaired by applying uncured PDMS on the leaking areas and putting the cushion in the oven for 30min, then after cooling to room temperature the cushion was retested for leaks with soapy water.

The linear stage experimental setup was again done on the test cushion, but replaced the aluminum block with a glass tube that had a spherical end, as seen in Figure 35.

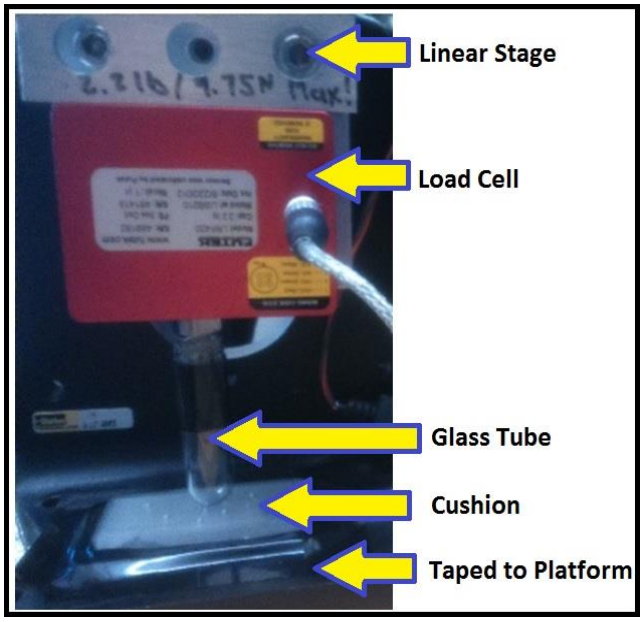

Figure 35 - Linear stage and load cell with glass tube and test cushion.

This experiment involved the linear stage moving the glass tube down, to push on the top surface of the cushion in 1mm steps, up to and including 3.88mm, which is close to the 4mm cushion bladder height, and observing the changes in air pressure inside the cushion while measuring the reaction force using the load cell. The test cushion edges were taped in place to resist the edges of the cushion from folding or lifting up when the glass tube pushed on the cushion. This linear stage test was repeated for five trials. The experimental force and pressure of the cushion due to the glass tube and linear stage were plotted, as shown in Figure 36.

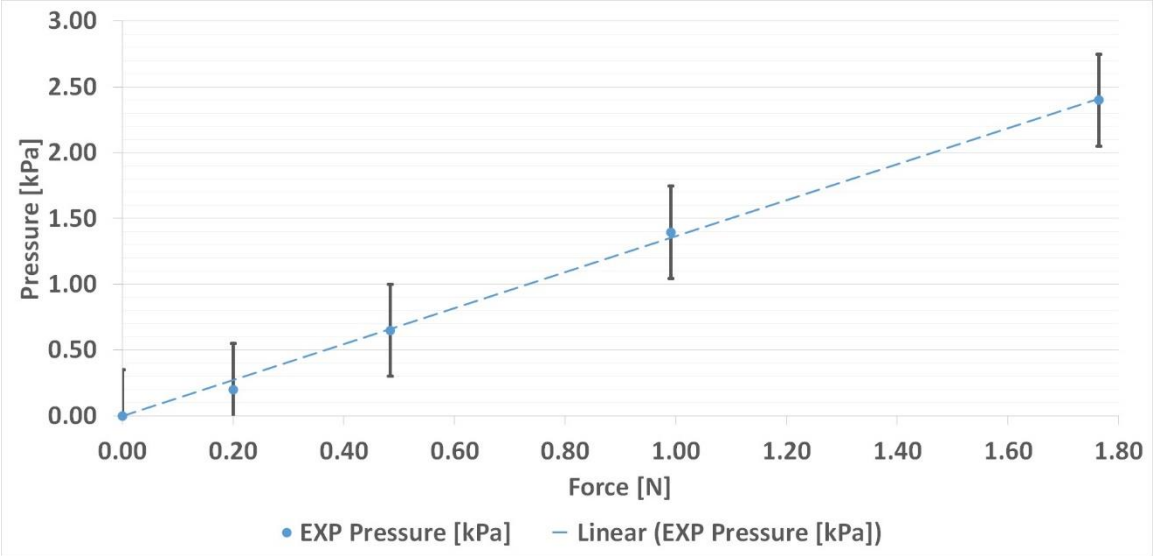

Figure 36 - Force vs pressure plot from the glass tube and the test cushion.

A linear curve fitting was applied onto the data points, which had an R^2 value above 0.9, with the *y=mx* form, and were within the error bars which represent the uncertainty of the air pressure sensor ±0.35kPa [57].

It is interesting to note the physical characteristics of the glass tube, the cushion, and its interactions which change the air pressure of the cushion. As described from the textbooks "Theory of Plates and Shells" by S. Timoshenko and S. Woinowsky-Krieger [59] and "Thin Plates and Shells: Theory, Analysis, and Applications" by E. Ventsel and T. Krauthammer [60], the cushion's top surface can be considered as a thin plate if

$$8 \dots 10 \leq a/h \leq 80 \dots 100 \quad (1)$$

where *h* is the plate thickness and *a* is a typical dimension of a plate. If *a/h* is 10 or less, the plate is considered to be a thick plate, or if *a/h* is 80 or greater, the plate is considered a membrane. In the case of the cushion in this study, *a=50mm* and *h=1mm*, thus this cushion is considered a thin plate, and so Kirchhoff's Classical Plate Theory can be used [60]. The governing equation for plate bending is given as

$$\frac{\partial^4 w}{\partial x^4} + 2\frac{\partial^4 w}{\partial x^2 \partial y^2} + \frac{\partial^4 w}{\partial y^4} = \frac{q}{D} \quad (2)$$

where *w=w(x,y)* is the vertical deformation, which is orthogonal to the *x* and *y* directions and normal to the top surface of the plate, *q=q(x,y)* is the intensity of the load, and *D* is the flexural rigidity of the plate given as the following:

$$D = \frac{Eh^3}{12(1-\upsilon^2)} \tag{3}$$

where *E* is the modulus of elasticity, *h* is the thickness of the plate, and *v* is Poisson's ratio. The boundary condition that best fits the case of the cushion's top surface and its walls is a clamped edge where the walls of the cushion are assumed to be rigid. This means that the deflection and slope at the edges of the plate are zero in the *x* and *y* directions:

$$w = 0 \qquad \frac{\partial w}{\partial x} = 0 \Big\} \; x \; constant \tag{4}$$

$$w = 0 \qquad \frac{\partial w}{\partial y} = 0 \Big\} \; y \; constant$$

where *w* is the deflection and the partial derivative of *w* is the slope. If the displacement of the cushion is the product of two functions with respect to the *x* and *y* directions, then the deflection equation is as follows:

$$w(x,y) = F(x)G(y) = \sum_m^\infty F_m \sin\left(\frac{m\pi x}{a}\right) * \sum_n^\infty G_n \sin\left(\frac{n\pi y}{b}\right) \tag{5}$$

$$w(x,y) = \sum_m^\infty \sum_n^\infty F_m G_n \sin\left(\frac{m\pi x}{a}\right) \sin\left(\frac{n\pi y}{b}\right) \tag{6}$$

where F_m, and G_n and are the coefficients found from the Fourier series. The multiplication of these coefficients can be expressed as the displacement coefficient w_{mn}, where the deflection equation for a thin plate becomes

$$w(x,y) = \sum_m^\infty \sum_n^\infty w_{mn} \sin\left(\frac{m\pi x}{a}\right) \sin\left(\frac{n\pi y}{b}\right). \tag{7}$$

Solving for the displacement coefficient and integrating the periodic functions using Fourier expansion with limits from *0* to *a* along the length of the plate with respect to *x*, and *0* to *b* along the width of the plate with respect to *y*, we obtain

$$w_{mn} = \frac{4}{ab}\int_{y=0}^{y=b}\int_{x=0}^{x=a} \mathrm{w(x,y)}\sin\left(\frac{m\pi x}{a}\right)\sin\left(\frac{n\pi y}{b}\right) d_x d_y. \qquad (8)$$

Differentiating the vertical displacement of equation (2), and substituting the deflection equation for a thin plate (7), the governing equation then becomes

$$\sum_m^\infty \sum_n^\infty \left(\frac{m\pi}{a}\right)^4 w_{mn} \sin\left(\frac{m\pi x}{a}\right)\sin\left(\frac{n\pi y}{b}\right)$$

$$+2\sum_m^\infty \sum_n^\infty \left(\frac{m\pi}{a}\right)^2\left(\frac{n\pi}{b}\right)^2 w_{mn} \sin\left(\frac{m\pi x}{a}\right)\sin\left(\frac{n\pi y}{b}\right)$$

$$+\sum_m^\infty \sum_n^\infty \left(\frac{n\pi}{b}\right)^4 w_{mn} \sin\left(\frac{m\pi x}{a}\right)\sin\left(\frac{n\pi y}{b}\right) = \frac{q_{mn}}{D} \qquad (9)$$

where q_{mn} is the loading coefficient and is dependent on the type of load that is applied onto the thin plate. Simplifying equation (9) and collecting like terms gives

$$\left[\left(\frac{m\pi}{a}\right)^4 + 2\left(\frac{m\pi}{a}\right)^2\left(\frac{n\pi}{b}\right)^2 + \left(\frac{n\pi}{b}\right)^4\right] w_{mn} = \frac{q_{mn}}{D} \qquad (10)$$

which can be solved for the displacement coefficient w_{mn} as the following algebraic expression:

$$w_{mn} = \frac{q_{mn}}{D\pi^4\left(\frac{m^2}{a^2}+\frac{n^2}{b^2}\right)^2}. \qquad (11)$$

Substituting equation (11) into the thin plate displacement equation (7), the deflection of the plate's surface is the following expression:

$$w(x,y) = \sum_m^\infty \sum_n^\infty \frac{q_{mn}}{D\pi^4\left(\frac{m^2}{a^2}+\frac{n^2}{b^2}\right)^2}\sin\left(\frac{m\pi x}{a}\right)\sin\left(\frac{n\pi y}{b}\right). \qquad (12)$$

The diagram of the centralized load from the glass tube onto the cushion is as seen in Figure 37, where *a* is the length of the cushion, *b* is the width of the cushion, *r* is the radius of the glass tube, which is represented by the orange circle, and q_{CLo} in the orange circle is the centralized load on the cushion.

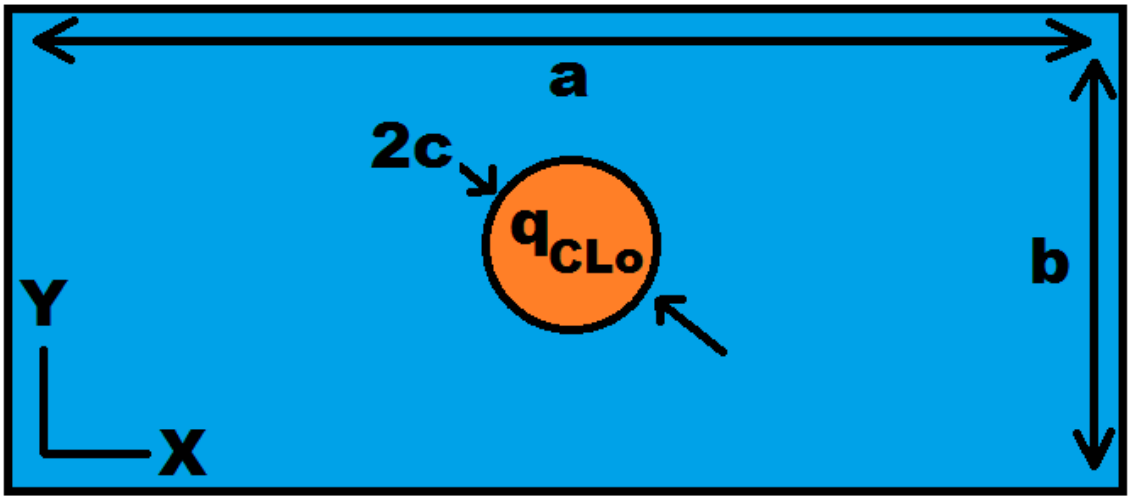

Figure 37 - Centralized loading of the cushion top view from the glass tube.

The glass tube loading onto the cushion creates large deflections on the cushion's top surface. From plate bending theory, when there are large deflections, there are can be a stretching of the middle surface. This stretching of the plate surface occurs when

$$w \geq 0.3h, \tag{13}$$

where *w* is the displacement and *h* is the plate thickness [60]. For the case of the cushion in the glass tube linear stage test, the *w=3.88mm* and *h=1mm*. Therefore, the large deformations on the cushion's top surface are seen as bulging areas on the cushion surface on either side of the glass tube, as well as the surface area where the glass tube pushes into the cushion bladder, as seen in Figure 38.

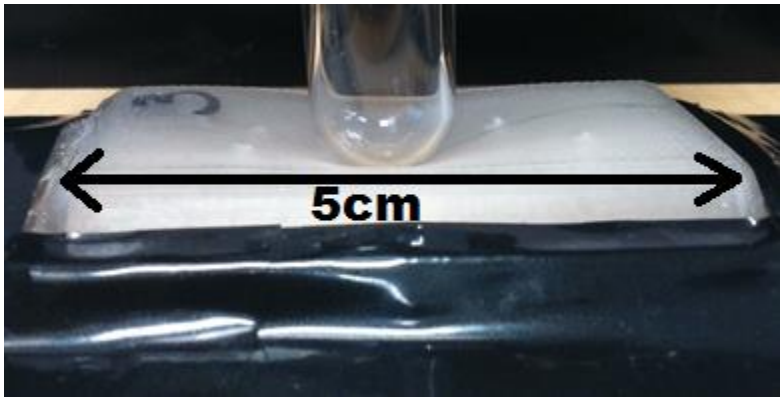

Figure 38 - Linear stage with glass tube pushing on the cushion surface.

The theory of plate bending with a centralized load on a flat plate [59] will be investigated in the following equations below.

From the textbook “Theory of Plates and Shells” by S. Timoshenko and S. Woinowsky-Krieger [59], the centralized load q_{CLo} of a circular area over a rectangular plate, can be expressed in polar coordinates ρ and θ, with a radius c, and the centroid located at the centre of the plate $x=\zeta$ and $y=\eta$. Solving for the loading coefficient of centralized load q_{CLmn} gives

$$q_{CLmn} = \frac{4}{ab}\frac{q_{CLo}}{\pi c^2}\int_0^c\int_0^{2\pi} sin\frac{m\pi(\zeta+\rho cos(\theta))}{a} sin\frac{n\pi(\eta+\rho cos(\theta))}{b}\rho\, d\rho\, d\theta. \qquad (14)$$

Since the circle remains inside the plate boundaries and $c=\rho$, then the integrals from equation (14) gives the following expression:

$$q_{CLmn} = \frac{8q_{CLo}}{abc\gamma_{mn}} J_1(\gamma_{mn}c) sin\frac{m\pi\zeta}{a} sin\frac{n\pi\eta}{b} \qquad (15)$$

where $\gamma_{mn} = \pi\sqrt{\left(\frac{m}{a}\right)^2 + \left(\frac{n}{b}\right)^2}$ and $J_1(\gamma_{mn}c)$ is the Bessel function of order one, with the argument $\gamma_{mn}c$. Substituting the loading coefficient q_{CLmn} from equation (15) into the displacement equation (12), then gives the following:

$$w_{CL_{mn}} = w(x,y) = \frac{1}{\pi^4 D}\sum_m^\infty\sum_n^\infty \frac{\sin\left(\frac{m\pi x}{a}\right)\sin\left(\frac{n\pi y}{b}\right)}{\left[\left(\frac{m}{a}\right)^2 + \left(\frac{n}{b}\right)^2\right]^2} * \frac{8q_{CLo}}{abc\gamma_{mn}} J_1(\gamma_{mn}c) sin\frac{m\pi\zeta}{a} sin\frac{n\pi\eta}{b}$$

$$= \frac{8q_{CLo}}{\pi^4 Dabc} * \sum_m^\infty \sum_n^\infty \frac{\sin\left(\frac{m\pi x}{a}\right)\sin\left(\frac{n\pi y}{b}\right)}{mn\left[\left(\frac{m}{a}\right)^2+\left(\frac{n}{b}\right)^2\right]^2} * \frac{J_1(\gamma_{mn}c)}{\gamma_{mn}} sin\frac{m\pi\zeta}{a} sin\frac{n\pi\eta}{b} \quad (16)$$

where w_{CLmn} is the displacement of the plate at any position *m* and *n* due to a centralized load of a circular area. The maximum deflection of the rectangular plate surface from a uniformly distributed load can be found at the centre of the plate where *x=a/2* and *y=b/2*.

Although there is another load acting on the cushion's surface, the air inside the cushion is also applying a uniformly distributed load on the cushion's top surface from the inside as seen in Figure 39, where *a* is the length of the cushion, *b* is the width of the cushion, and q_{UDLo} is the uniformly distributed load.

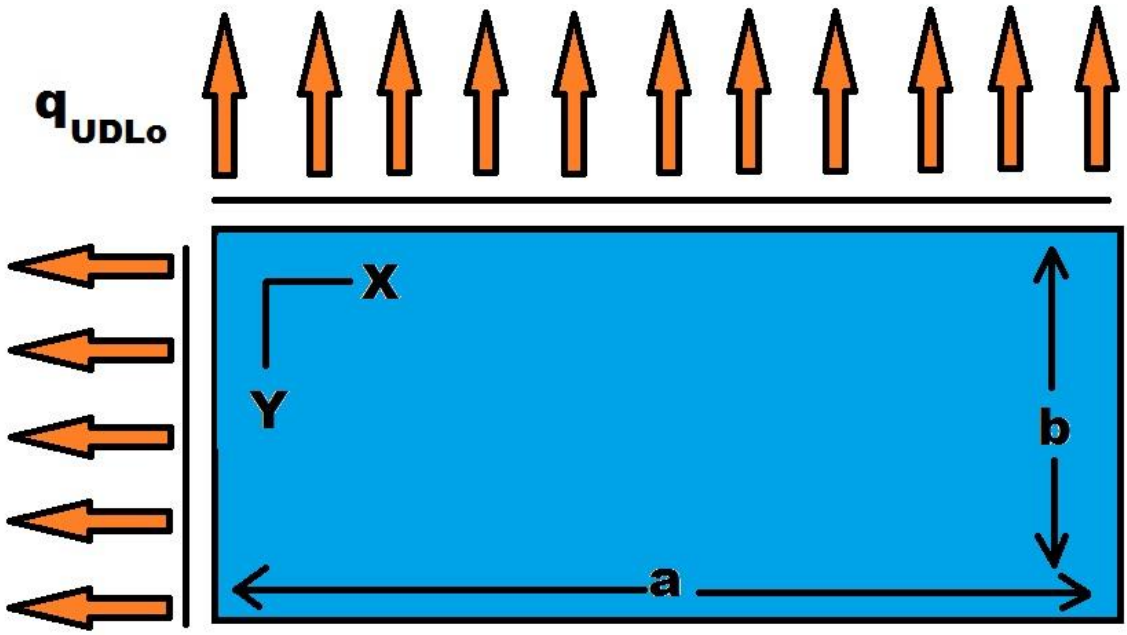

Figure 39 - Uniformly distributed loading of air viewed from the cushion bottom.

The plate theory equation as seen in the textbook "Theory of Plates and Shells" by S. Timoshenko and S. Woinowsky-Krieger [59], for a uniformly distributed load q_{UDLo}, over a rectangular plate is

$$q_{UDLo} = q(x,y) = \sum_m^\infty \sum_n^\infty q_{UDL_{mn}} * \sin\left(\frac{m\pi x}{a}\right) * \sin\left(\frac{n\pi y}{b}\right). \quad (17)$$

The load covers the total area of the cushion's top surface of the inside of the cushion, from *0 to a* in the *y* direction, and from *0 to b* in the *x* direction. The loading coefficient q_{UDLmn} of the uniformly distributed load of the total rectangular area of the plate surface is given by the double Fourier expansion as:

$$q_{UDL_{mn}} = \frac{4}{ab}\int_0^a \int_0^b q_{UDLo} * \sin\left(\frac{m\pi x}{a}\right) * \sin\left(\frac{n\pi y}{b}\right) d_x d_y. \quad (18)$$

The integrals of equation (18) are evaluated as:

$$\int_0^a \sin\left(\frac{m\pi x}{a}\right) d_x = -\frac{a(cos(m\pi)-1)}{m\pi}, \quad (19)$$

$$\int_0^b \sin\left(\frac{n\pi y}{b}\right) d_y = -\frac{b(cos(n\pi)-1)}{n\pi}. \quad (20)$$

Combining equations (18), (19), and (20) gives the loading coefficient to be

$$q_{UDL_{mn}} = \frac{4q_{UDLo}}{ab} * \frac{-a(cos(m\pi)-1)}{m\pi} * \frac{-b(cos(n\pi)-1)}{n\pi}. \quad (21)$$

If *m* or *n* or both in equation (21) are even integers then the loading coefficient q_{UDLmn} becomes zero. If *m* and *n* are odd integers, then the loading coefficient q_{UDLmn} becomes

$$q_{UDLmn} = \frac{4q_{UDLo}}{ab} * \frac{2a}{m\pi} * \frac{2b}{n\pi}. \quad (22)$$

Simplifying equation (22) by multiplying the terms obtains

$$q_{UDL_{mn}} = \frac{4q_{UDLo}}{ab}\left(\frac{4ab}{mn\pi^2}\right) = \frac{16q_{UDLo}}{mn\pi^2}. \quad (23)$$

The plate displacement equation (12) for the case of a uniformly distributed load on a rectangular plate is given by

$$w_{UDL_{mn}} = w(x,y) = \frac{1}{\pi^4 D}\sum_m^\infty \sum_n^\infty \frac{q_{UDL_{mn}} \sin\left(\frac{m\pi x}{a}\right)\sin\left(\frac{n\pi y}{b}\right)}{\left[\left(\frac{m}{a}\right)^2 + \left(\frac{n}{b}\right)^2\right]^2} \quad (24)$$

where w_{UDLmn} is the displacement of the plate at any position *m* and *n* due to the uniformly distributed load.

Then substituting the loading coefficient q_{UDLmn} from equation (23) into the uniformly distributed load plate equation (24) gives the deflection equation

$$w_{UDL_{mn}} = \frac{16q_{UDLo}}{\pi^6 D} \sum_m^\infty \sum_n^\infty \frac{\sin\left(\frac{m\pi x}{a}\right)\sin\left(\frac{n\pi y}{b}\right)}{mn\left[\left(\frac{m}{a}\right)^2+\left(\frac{n}{b}\right)^2\right]^2} \quad (25)$$

where *m* and *n* are odd integers. The maximum deflection of the rectangular plate's surface from a uniformly distributed load can be found at the centre of the plate where $x=a/2$ and $y=b/2$.

6.2. Repeatability Test

The usability of the polymeric cushion is dependent upon how reliably the cushion can provide a consistent value for a given load. To prove the cushion's ability to reproduce results, the chosen PDMS cushion underwent a repeatability test. In this test, the linear stage pushed on the top surface of the cushion with an aluminum block, repeatedly loading and unloading five times until the force sensor on the linear stage reached a set-point force limit. This process was repeated for the force values of 2N, 4N, 6N, and 8N. The data is used for calibrating the cushions' force and pressure characterization relationship. The repeatability test with the linear stage allows the experiments to be done consistently and in a controlled manner. If the repeatability test shows that the cushion can give pressure readings that are within the uncertainty of the air pressure cushion's error bars, then the cushion will be considered sufficiently repeatable. The results of the repeatability test for the test cushion, using the linear stage and aluminum block, as seen in Figure 40.

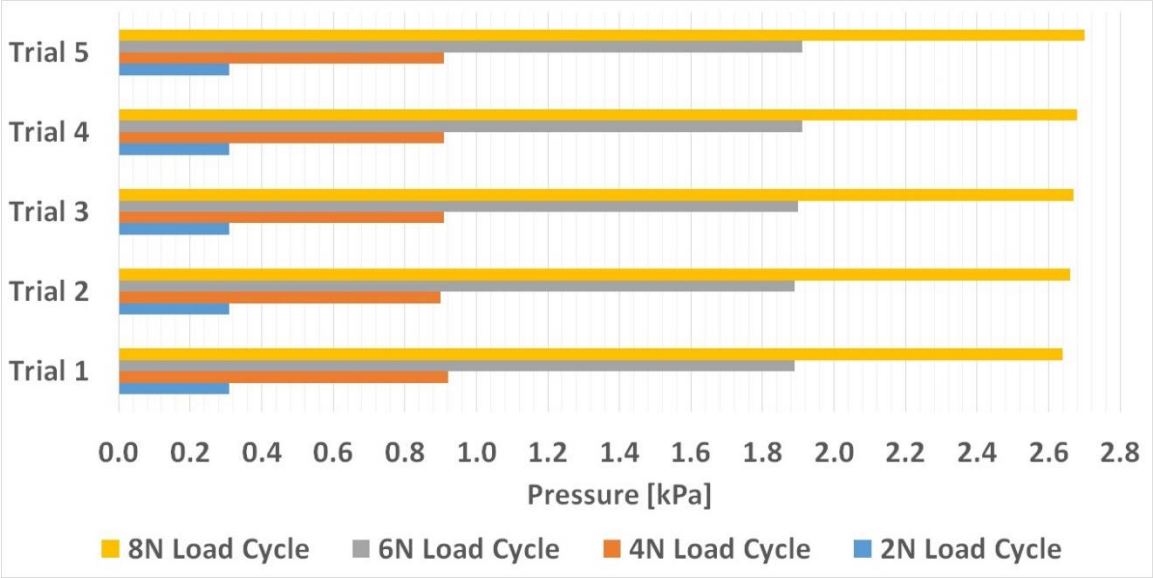

Figure 40 - Repeatability test results for the test cushion.

The pressure output results, in kilo-pascals, of the repeatability test on the test cushion for five repetitions of loading and unloading of 2N, 4N, 6N, and 8N, are shown in Table 1. The standard deviation of each trial for each load, the mean value for each load, and the standard error of the mean for each load are calculated to show a numerical representation of the repeatability test.

Table 1 - Numerical representation of the repeatability test results.

Load Cycle	**Air Pressure [kPa]**						
	Trial 1	**Trial 2**	**Trial 3**	**Trial 4**	**Trial 5**	**Mean Value**	**Standard Deviation**
2N	0.31	0.31	0.31	0.31	0.31	0.31	0.00
4N	0.92	0.90	0.91	0.91	0.91	0.91	0.01
6N	1.89	1.89	1.90	1.91	1.91	1.90	0.01
8N	2.64	2.66	2.67	2.68	2.70	2.67	0.02

The data from the repeatability test was used to calibrate the cushion for an input force from the output pressure. The pressure of the test cushion and the force from the linear stage vs time plot for an 8N load during one trial of five cycles, is seen in Figure 41.

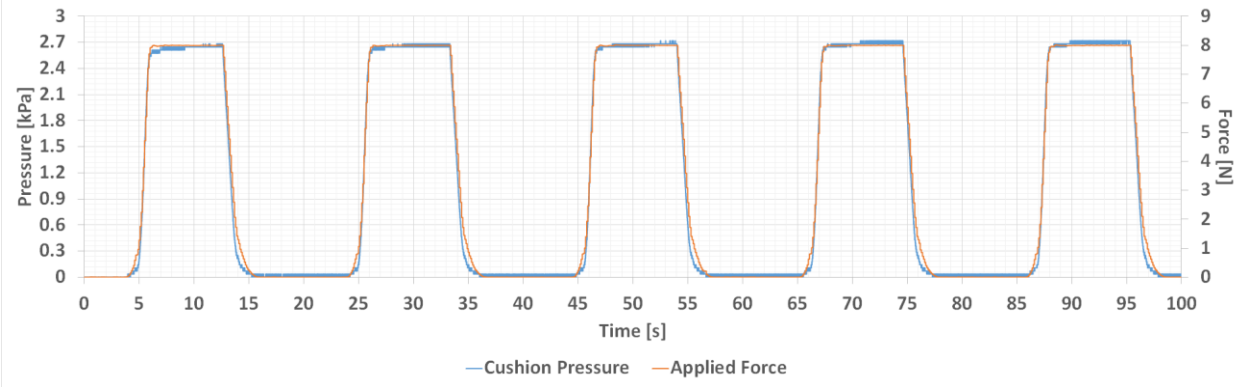

Figure 41 - Calibration test plot with the output of the test cushion.

6.3. Cushion Characterization

The recorded values of each force trial were averaged from each test that was performed on each cushion and recorded. The test cushion's characteristics showed slight variations within the error bounds of the pressure sensors in their plotted averages, which was expected because the cushions were made by hand. The trend line of the test cushion's output pressure vs input force is shown in Figure 42.

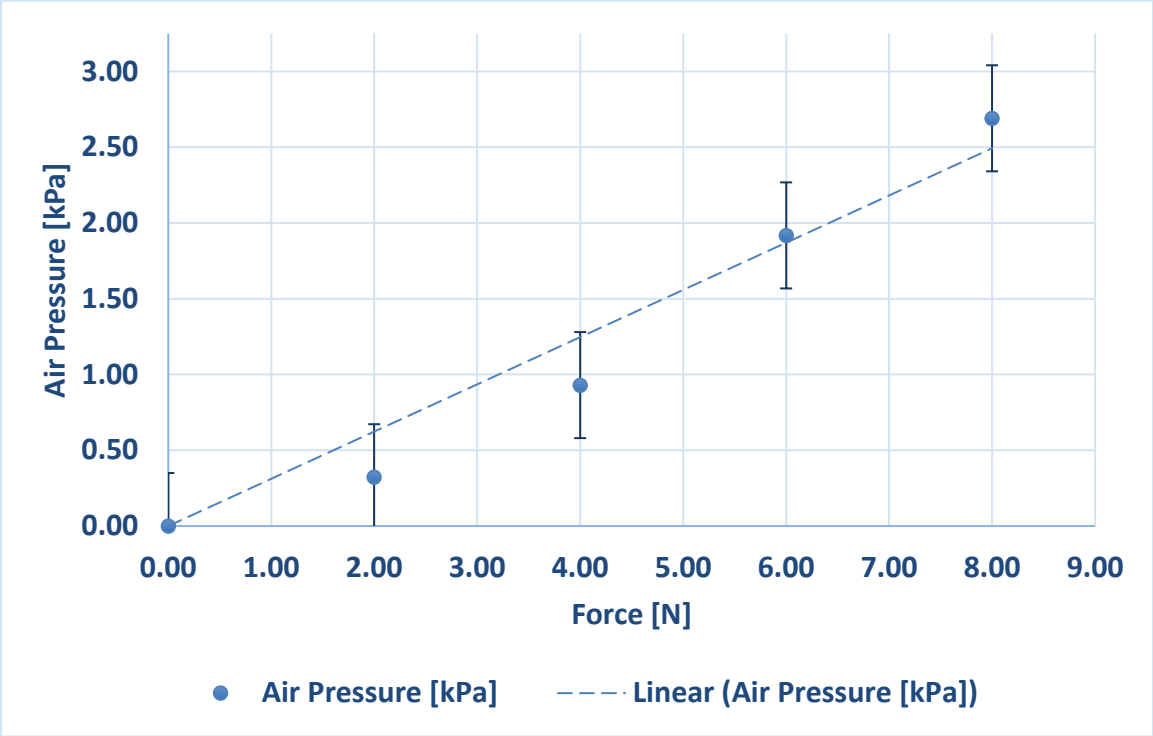

Figure 42 - Force vs pressure plot from the aluminum block and the test cushion.

It's interesting to note that the deflection of the cushion's top surface is uniformly displaced by the aluminum block that was attached to the linear stage, and that the cushion was subjected to small deformations up to and including the 8N applied force point. Small deflections on thin plates are defined as

$$w \leq 0.2h \tag{26}$$

where *w* is the displacement and *h* is the plate thickness [60]. For the case of the cushion in the aluminum block linear stage test, the *w=0.2mm* and *h=1mm*, and so this case is considered a small deformation. The maximum deflection measured from the aluminum block test was less than 5% of the total cushion's bladder height. The loading from the aluminum plate is simply a vertical displacement of the cushion's top surface. Since this displacement occurs due to small deformations, which do not affect the bending of the cushion surface and thus do not involve any plate theory equations, it can be assumed that the change in pressure of the cushion from the aluminum plate is simply given by the Ideal Gas Law:

$$P = \frac{n_a RT}{\Delta V_c} \tag{27}$$

where ΔV_c is the change in volume of the cushion bladder due to a small vertical compression, R is the gas constant, T is the temperature of air inside the cushion which is assumed to be at room temperature, due to the small deformation of the cushion [61]. In equation (27) n_a is the number of air molecules, or moles, and is given as

$$n_a = \rho_a \frac{V_o}{m_a} \tag{28}$$

where the initial volume V_o of air inside the cushion, which can be found using the density of dry air ρ_a at room temperature, and the molar mass of air m_a [61].

The force and air pressure data points from the test cushion, seen plotted in Figure 42, are fitted with the linear trend line:

$$P = K * F \tag{29}$$

where K is the coefficient that relates the applied force on the cushion, F, to the measured output air pressure, P, from the cushion. The experimental and finite element model's K coefficients and R^2 values of the trend lines for the cushion. Using this relationship of air pressure to applied force, the cushions can be attached on an exoskeleton. This equation allows the LabVIEW 2013 code to interpret the air pressure values that are given from the cushion to an applied force. The sensitivity of the test cushion was found from the slope of the characteristic curve's trend line to be 0.312 kPa/N. This relationship is repeated for each of the six cushions used in the wrist brace exoskeleton application in Chapter 8. A combination of these cushion force equations were used to interpret the pressures that were read from the pressure sensors into isometric force and measure specific movements of a forearm on a wrist brace exoskeleton.

Six cushions were fabricated by hand in-house and had undergone the linear stage aluminum block repeatability test to be characterized for their force and pressure relationships, as seen in Figure 43.

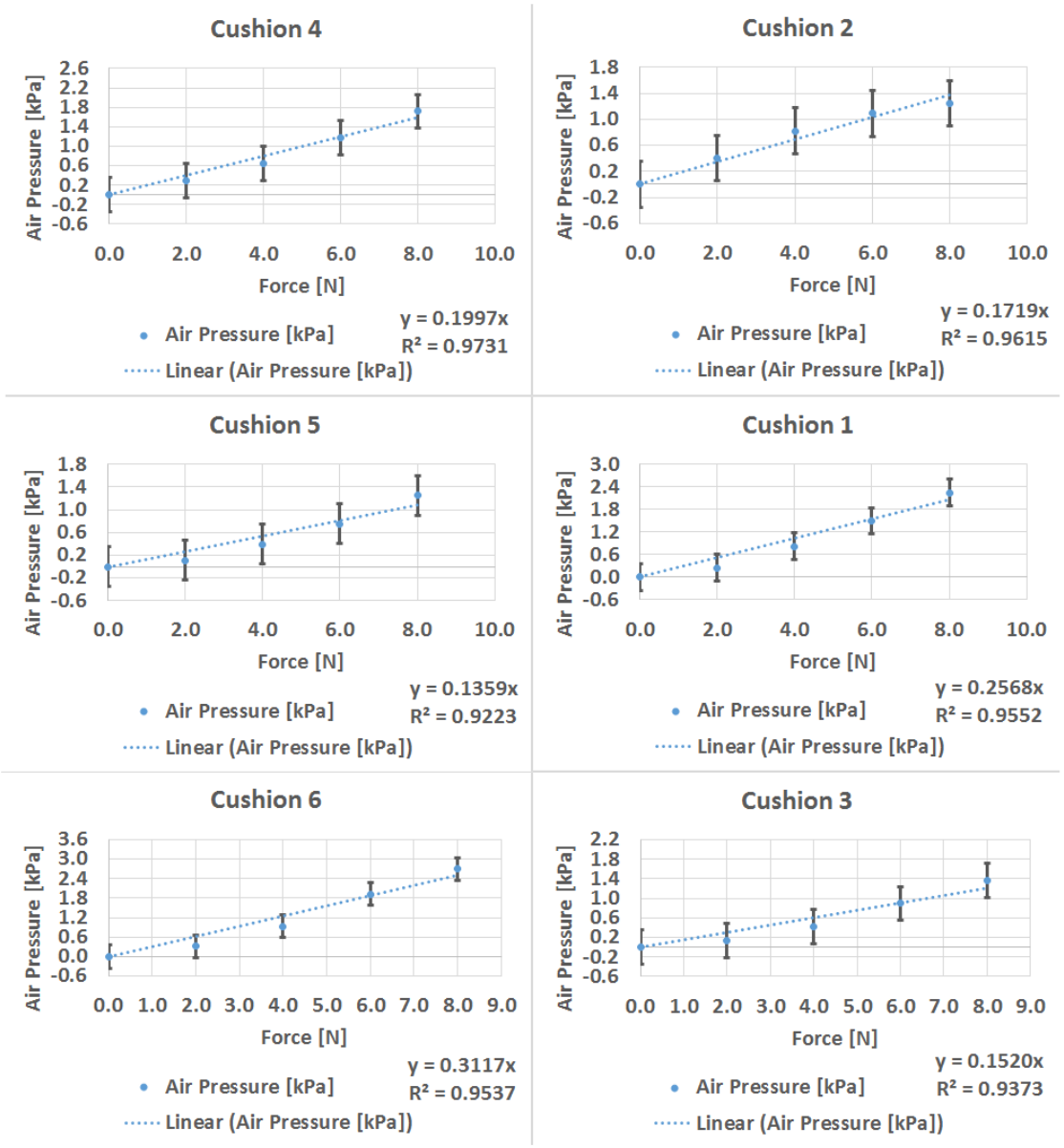

Figure 43 - Linear stage characterization trend lines for all 6 cushions.

When comparing the slopes of the force versus pressure trend lines between the six cushions, the average slope of the trend lines and the variation between the cushions can be seen in Figure 44.

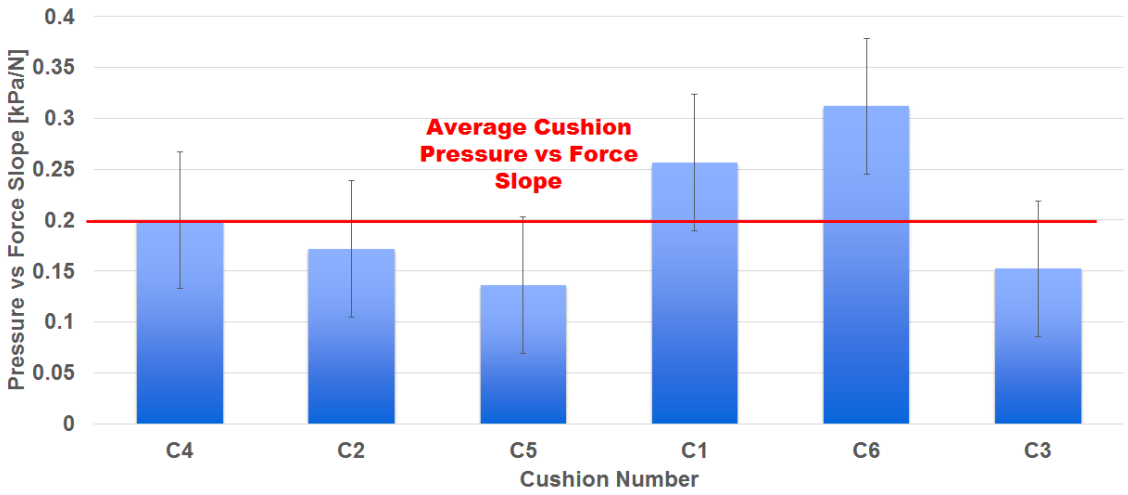

Figure 44 - Average cushion pressure vs force slope.

The six cushions have an average force versus pressure slope of 0.20kPa/N. The variability of the six cushion characterization curves have a standard deviation of 0.07kPa/N. This variability in the input force and output pressure slope relationship of the six cushions in this study, compared to the of the force and output MVC metric slopes of the six cushions that were used by Kong et al. [19] had a standard deviation to mean value ratio of 39%, whereas the same ratio for the cushions in this study is 35%. For the purposes of this preliminary testing of the cushions, since the cushion characterization slopes themselves are within the ±0.35kPa error bars of the air pressure sensor it's considered acceptable. This variability can be significantly reduced if another 3D-printed mold could be made such that all six cushions would be fabricated at once. The variabilities in human error during the fabrication procedure regarding each cushion's exact hardening and bulk material's ratios, mixing process, degassing process, oven curing times and cooling effects after being taken out of the oven, would greatly reduce the variation in performance between each cushion. Ideally the cushions would have a stand deviation to input/output slope ratio that is within that of the air pressure sensor's ratio, which is the 5%, as seen in the air pressure sensor's datasheet [57].

6.4. Long Duration Loading Test

A long duration loading test was performed on the test cushion to see how much the depressurization rate would be if the cushion was loaded with 8N for 15 minutes, or 900 seconds. The results showed at the end of the test, the pressure of the cushion had dropped at a depressurization rate of -0.00048 kPa/s as seen in Figure 45.

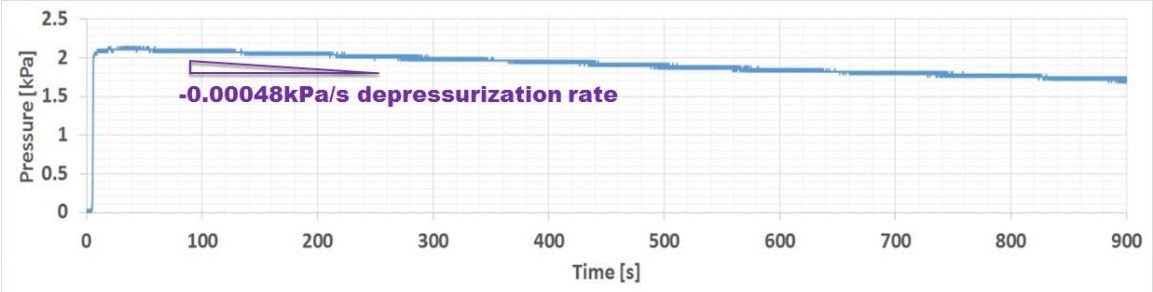

Figure 45 - Long duration loading test on the cushion.

This rate is considered to be insignificant compared to the average loading time of a few seconds as described in the rehab protocols of Herrnstadt et al. [17], when loading the cushions with an arm and holding that position. This test for loading over a long period of time observe is the creep effects of the PDMS cushion's material begin to relax and stretch under pressure. A more rigorous test would be needed to be performed in order to verify the suitability of the polymeric cushions for practical applications such as rehabilitation exoskeletons and assistive orthoses. A test to measure the maximum applied force from a human forearm that the cushions could sustain before breaking or leaking the air inside the cushion bladder was performed.

6.5. Maximum Cushion Pressure Failure Test

A maximum cushion pressure failure test was performed on the test cushion in order to measure what the maximum pressure can be held inside a polymeric cushion before it fails. The polymeric cushion was loaded with an increasing applied force until its breaking point or maximum holding pressure was reached. The air pressure inside the cushion was measured with the (MPXV7007DP, Freescale Semiconductor, Inc., Austin, TX) pressure sensor [50], and the applied force was measured from a (LCM300, FUTEK Advanced Sensor Technology, Inc., Irvine, CA) load cell [62]. The maximum load and pressure measured by the load cell and pressure sensor was approximately 190N (19.4kg of force) and 52kPa, which occurred at 4.3 seconds as shown in Figure 46.

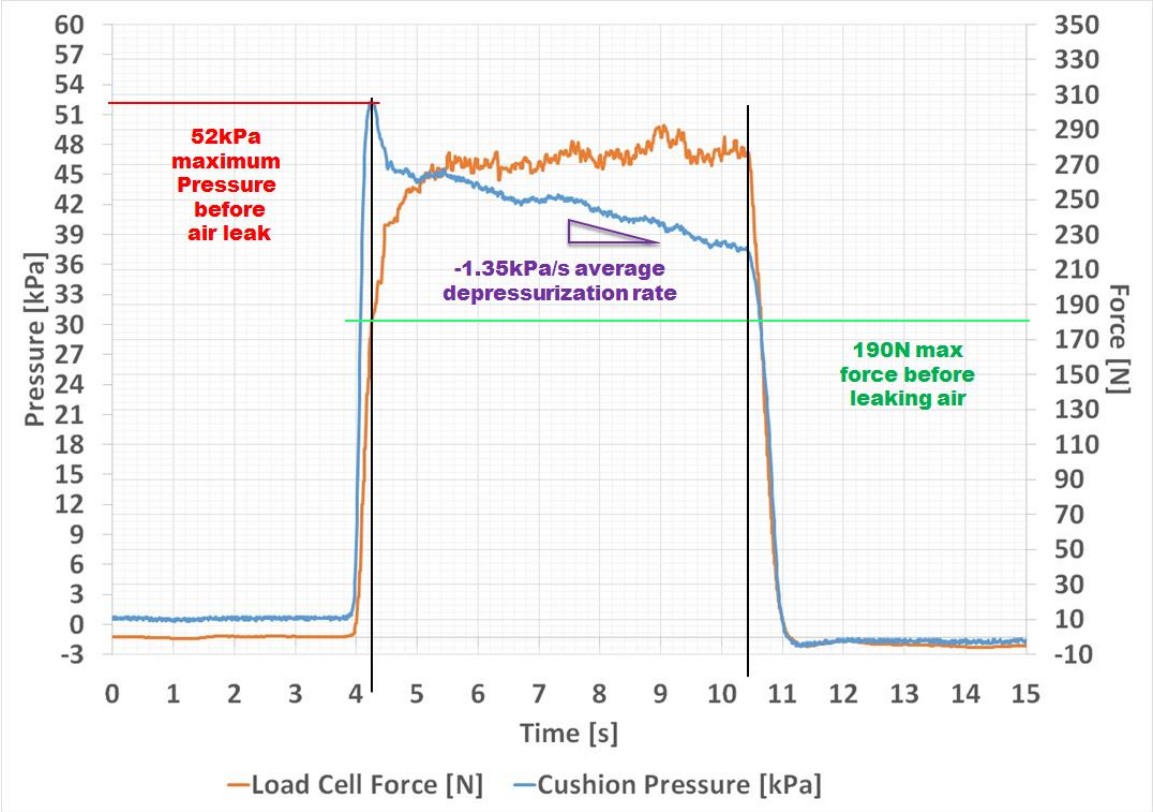

Figure 46 - Maximum cushion pressure failure test.

This test was performed with an elbow flexion/extension motion, measuring the maximum applied force at the forearm with the test cushion. At 52kPa of pressure inside the cushion, which correlates to 190N of force as measured by the load cell, the air pressure showed a spike at 4.3 seconds and began to decrease at an average rate of -1.35kPa/s until the applied pressure was removed at 10.2 seconds. Since the distance from the elbow to the forearm is 26.2cm, the maximum applied torque from the elbow was 49.8Nm. This is 69% of the recommended design requirements for training/rehabilitation devices for elbow flexion/extension forces as described by Tsagarakis et al. [30] to be 72.5Nm. The cushion's maximum force could be further improved by better sealing the interfacing connection of the polymeric cushion's tube and the pressure sensor's port. No tears or ruptures were found on the cushion's surface anywhere. It was observed at the end of the test, that the cushion had deflated, as seen in Figure 47, and remained this way until after the test, when the ambient air was let back into the cushion's bladder; after which the cushion functioned normal.

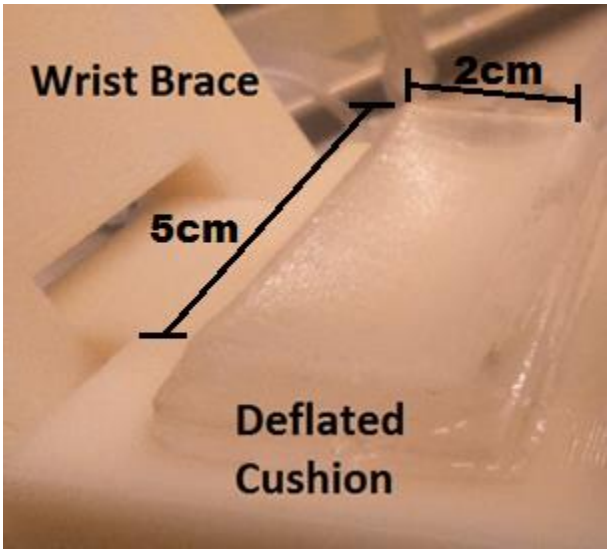

Figure 47 - Cushion deflated surface after maximum pressure test.

After checking the cushion for leaks using the soapy water test, it was confirmed that the cushion had not broken or torn anywhere, and that the air had leaked out of the end of the cushion's tube interface that was press fitted with friction onto the air pressure sensor port.

6.6. Summary

The linear stage test setup with the aluminum block and the glass tube were done to carry out the physical experiment of the conditions that the FEM was made to simulate. The aluminum block test had a distributed load on the tested cushion during the linear stage test, where the cushion underwent a small deformation of 5% of the cushion bladder's height under 8N of force, even though the maximum measureable force before reaching the failure point at 190N. This resulted in a linear trend line from the test cushion's aluminum block experimental force vs pressure data, with an R^2 value above 0.9. The glass tube test had a centralized loading on the tested cushion during the linear stage test, where and the cushion underwent a large deformation nearly touching the bottom surface of the cushion bladder. This resulted in a linear trend line from the test cushion's glass tube experimental force vs pressure data, with an R^2 value above 0.9. The average force and pressure characterization slope between the six cushions is 0.2kPa/N with a standard deviation of 0.07kPa/N. The variation of the characteristic curves from the six fabricated

cushions was found to have a better average value-to-standard-deviation ratio, 35%, compared to that of the prior art at 39%.This variation can be significantly reduced if the six cushions were to be fabricated at the same time, throughout each fabrication process step. The repeatability test showed that the test cushion had a standard deviation of 0.024 kPa. The characterization of the test cushion was performed and found a linear trend line from equation (38). The long period loading test showed that the depressurization rate of the test cushion was -0.00048 kPa/s. And finally the maximum pressure test showed that the test cushion was able to measure forces up to 190N of force (52kPa of pressure) without leaking air or rupturing. This is very good since the recommended joint torques that rehabilitation exoskeleton should be able to sustain the suggested 72.5Nm of elbow torque, and the polymeric cushions have shown to be able to withstand 69% of that suggested value This is the highest load that the prior art of polymeric air cushions has been shown to bear. This shows the functional and practical capabilities of the polymeric air cushions and its potential applications for portable and cost effective rehabilitation and assistive orthoses.

Chapter 7. Finite Element Model vs Experimental

Objective 2 is partly covered by Chapter 7. This chapter is dedicated to the comparison between the performance results found from the finite element model and the experimental test data. The displacement of a glass tube onto the surface of a cushion was tested, and the output pressure of the cushion was measured and compared between the FEM and experimental results. The applied force from an aluminum plate onto the surface of a cushion was tested, and the output pressure of the cushion was measured and compared between the FEM and experimental data. The results of this chapter conclude the purpose of Objective 2.

7.1. Aluminum Plate Comparison

The experimental results of the aluminum block displacement test, compared to the FEM pressure results, are within the ±0.35kPa error bounds of the differential air pressure sensor [50] used to measure the pressure inside the cushions, as seen in Figure 48. This shows that the experimental results and the FEM model made on ANSYS line up well with each other, and verifies that the model of the cushion is accurate.

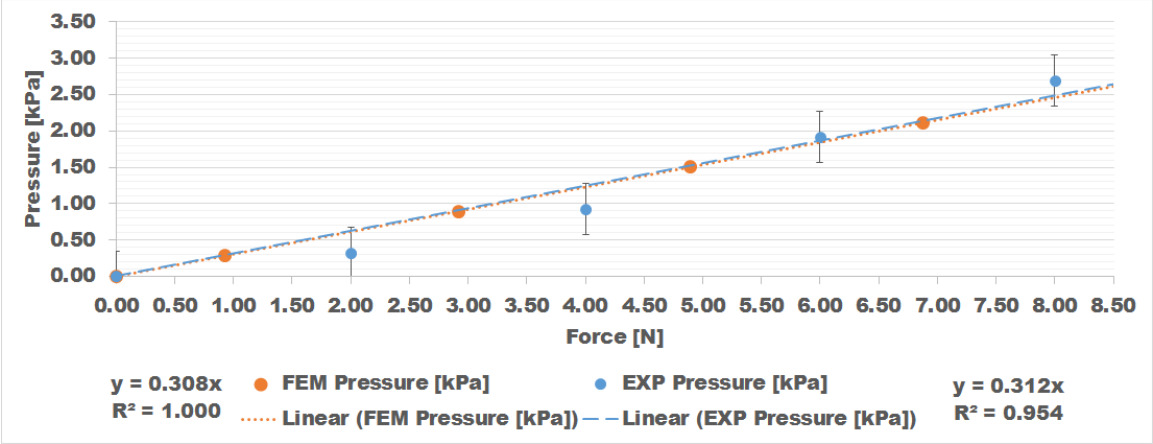

Figure 48 - Pressure vs Force comparison with the aluminum plate.

This shows that the experimental results and the FEM model made in ANSYS line up well with each other, and verifies that the finite model of the cushion is representative of

its behaviour. The experimental and finite element model K coefficients and R^2 values of the trend lines for the cushion are shown in Table 2.

Table 2 - Experimental and FEM Comparison for Aluminum Plate.

	K coefficient	**R^2 value**
Experimental	0.312	0.954
FEM	0.308	1.000

The R^2 value of the experimental and FEM trend lines are 0.954 and 1.000 respectively. The K coefficients representing the slopes of the trend lines between the experimental and FEM data points for the cushion has a difference of 1.28%. The data points from the FEM pressure curve suggest a linear relationship between the reaction force and the output pressure of the cushion, as the aluminum plate pushed onto the cushion. When the force sensor on the linear stage reached its maximum force range at 8N, the displacement of the top surface of the cushion reached a maximum of 0.2mm. The height of the inside chamber of the cushion's bladder is 4.5mm, which means that the deformation of the cushion's top surface was only 5% of its maximum inner chamber height. This means that the FEM and experimental trend line curves from Figure 48 represent the behaviour of the cushion under small deformations. The structural forces were measured in ANSYS from the contact elements between the aluminum plate and the top surface of the cushion. The changes in air pressure were measured from the pressure node on the inside the cushion. The force and pressure ranges measured in the FEM model matched with the experimental test results.

7.2. Glass Tube Displacement vs Pressure Comparison

The FEM model of the glass tube was displaced by 1mm, 2mm, 3mm, and 3.8mm, while the air pressure inside the cushion was measured and plotted against the experimental glass tub test. The experimental results of the glass tube displacement test,

compared to the FEM pressure results, are within the ±0.35kPa error bounds of the differential air pressure sensor [50] used to measure the pressure inside the cushions, as seen in Figure 48. This shows that the experimental results and the FEM model made on ANSYS line up well with each other, and verifies that the model of the cushion is accurate.

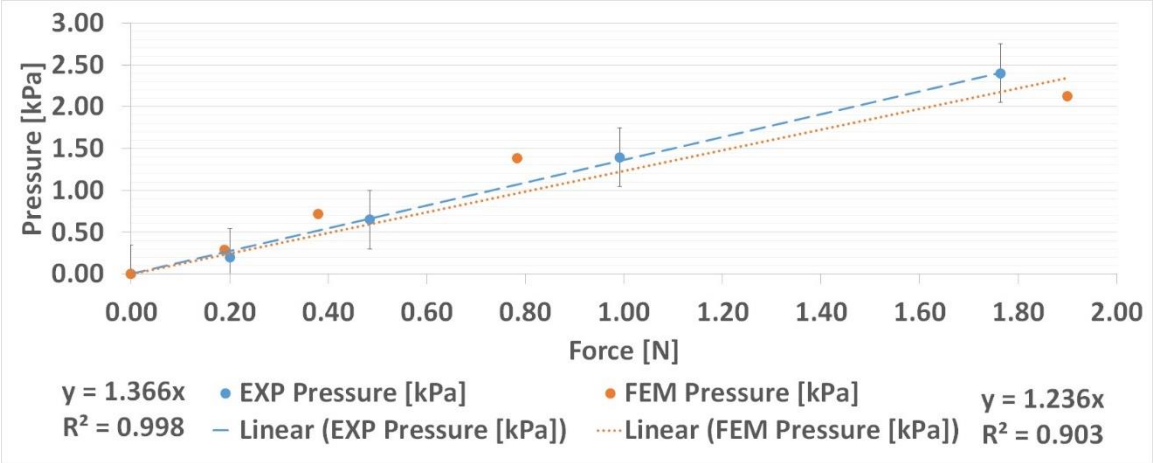

Figure 49 - Pressure vs Force comparison with the quarter sphere.

The experimental and FEM data points of the applied forces from the glass quarter sphere and the air pressure inside the cushion, are each fitted with a linear trend line, as shown in Table 3.

Table 3 - Experimental and FEM Comparison for Quarter Sphere.

	K coefficient	**R^2 value**
Experimental	1.366	0.998
FEM	1.236	0.903

Since the R^2 value of both the FEM and experimental data is above 0.9 while being within the error bars of the pressure sensor, it was suggested that the trend lines of the data points of both the FEM and experimental results were linear. The slopes of the trend lines between the experimental and FEM data points differ by 0.13kPa, which is off by 9.05%. The deformation of the cushion under the glass tube may have represented some

material behaviour due to the PDMS stretching as the air pressure forced the cushion's top surface around the glass tube to bulge up while the sides of the cushion remained unchanged, which the FEM model did capture. Although the FEM may not have been able to fully represent the experimental test cushion's material properties under the large deformations. This resulted in the slight deviation of the trend line from the FEM model compared to the experimental data as seen in Figure 49. Given this observation, both the FEM and experimental trend lines still remained within the error bounds of the air pressure sensor. The data points from the FEM pressure curve suggested a linear relationship between the input force and the output pressure of the cushion, as the glass tube pushed onto the cushion. The data was extracted from the ANSYS simulation with respect to the contact elements between the glass tube and the top surface of the cushion. The changes in air pressure were measured from the pressure node on the inside the cushion.

7.3. Summary

The FEM model and the experimental data showed both trend lines of the aluminum plate test and glass tube test to be within the errors of the air pressure sensor. The FEM and experimental characterization test results show that under the conditions of the cushion for both the aluminum plate and the glass tube, that the trend lines of the data were appeared to be linear. The small deformations that occurred during the aluminum plate test showed that the FEM and experimental data were off by only 1.28% while having an R^2 value above 0.9 suggesting a good fit with a linear relationship between applied force and the cushion's air pressure. The bulging of the PDMS material's properties that occurred may not have been well represented in the FEM model, resulting in a 9.05% difference compared to the experimental data's trend line, although again, both trend lines were within the error bounds of the air pressure sensor.

Chapter 8. Wrist brace Exoskeleton Application

Objective 3 is covered in Chapter 8. This chapter is dedicated to the application of the cushions on the wrist brace exoskeleton, the test procedure of measuring arm forces from different movements (forearm pronation/supination, flexion/extension of the elbow, and shoulder internal/external rotation), the mathematical equations for calculating the torque and forces from the cushions, and discussing the results and output comparisons between the wrist brace exoskeleton cushion values and the torque sensor and load cells. The outcomes of Objective 1 and 2 have to the investigation of Objective 3.

8.1. Wrist brace Exoskeleton and Cushion Configuration

The polymeric cushions were arranged in a hexagonal configuration on the exoskeleton wrist brace in order to measure the applied forces from the forearm in the assembled exoskeleton, as shown in Figure 50. The wrist brace was a 3D printed 9 x 7 x 7cm^3 structure that opened up from a hinge in order to allow the user to place their arm inside. When the latch was closed, the arm was in contact with all of the cushions, which then measured the movements of the forearm. The applied force from the user's forearm was the input to the system, and the contained change in air pressure inside the cushion was the measured output. The change in pressure was measured by the differential pressure sensor read by the data acquisition card and processed by a LabVIEW program.

The air pressure sensors worked in differential pairs, as seen in Figure 50, where the blue tube with the '+' and red tube with the '-' represent the positive and negative inlets of the differential pressure sensor. The three pressure sensors are labeled S1, S2, and S3 respectively. Each pressure sensor is connected to two polymeric cushions. Thus, the sensor S1's attached polymeric cushions are labelled C4 and C2, respectively, the sensor S2's attached polymeric cushions are labelled C5 and C1, respectively, and the sensor S3's attached polymeric cushions are labelled C6 and C3. The output signals from each of the pressure sensors are the mathematical difference between each of the cushions in the pairs, where a differential change on the polymeric cushions influences the output signal of the pressure sensor to which they are attached, thus changing the output signal

in the positive or negative direction. If the pressure values of the cushion pairs are equal in value, then the output signal of the pressure sensor will be zero.

Characterization tests as presented in the previous section were performed using the polymeric test cushion, which was then used as cushion C6, as seen in the cushion and sensor configuration in Figure 50. Similar characterization curves were obtained for other cushions as well.

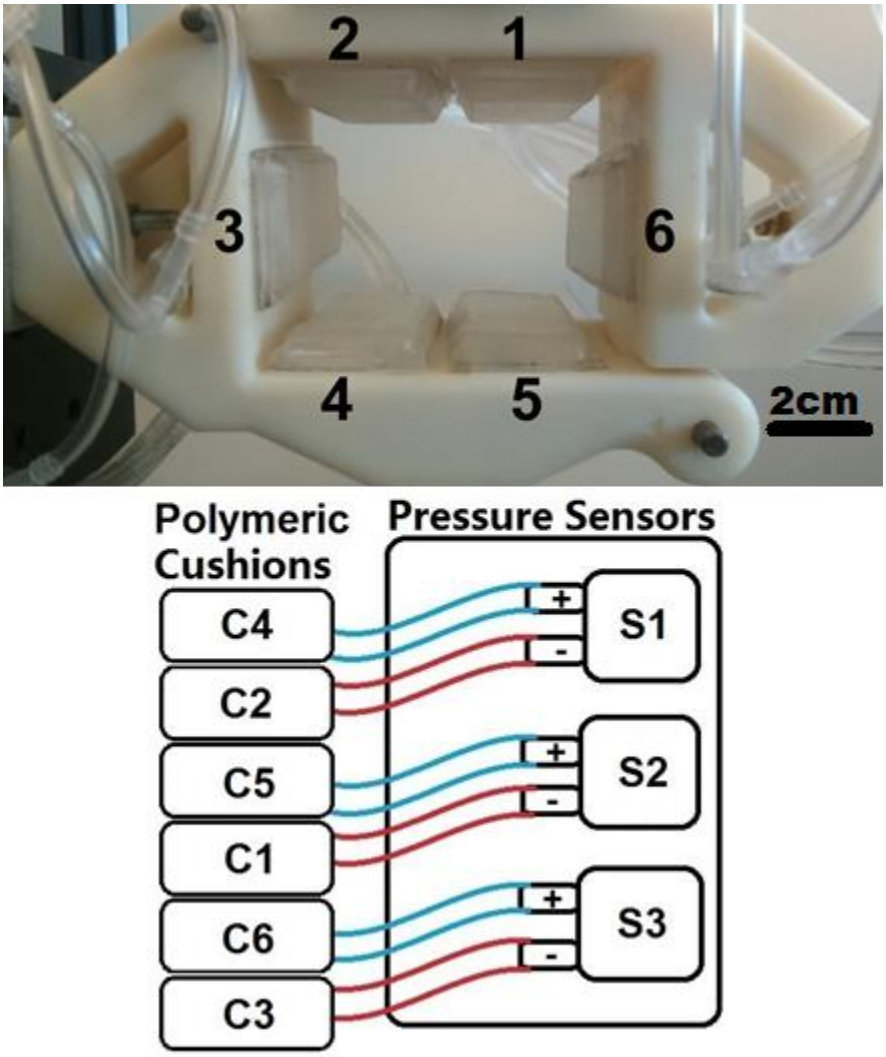

Figure 50 - Wrist brace cushions C1 to C6, pressure sensors S1 to S3.

8.2. Arm Movements in the Exoskeleton

The polymeric cushions were mounted on the wrist brace to measure isometric forces of three degrees of freedom at the user's forces at the wrist brace center, in torsional forearm pronation/supination, vertical elbow flexion/extension, and horizontal shoulder internal/external rotation, as illustrated in Figure 51 and labelled in green, red, and blue, respectively. The remaining three degrees of freedom as labelled in black, were not measureable with the proposed cushion configuration. Forearm yaw and forearm pitch rotations would require a second row of cushions to measure the differential pressure about the x-axis and z-axis respectively. Similarly, the forearm translation along the y-axis would require a cushion at the end of the user's hand. These considerations are not included in the current design. The preliminary study of these polymeric cushions as tested on a wrist brace exoskeleton focuses on evaluating the performance of the cushions and the human interaction forces in a simple configuration to reduce the measured errors from the system. The single row of cushions around the inside of the wrist brace captures the forces applied in the xz-plane, i.e. one rotational torque and two perpendicular translation forces, as shown in Figure 51.

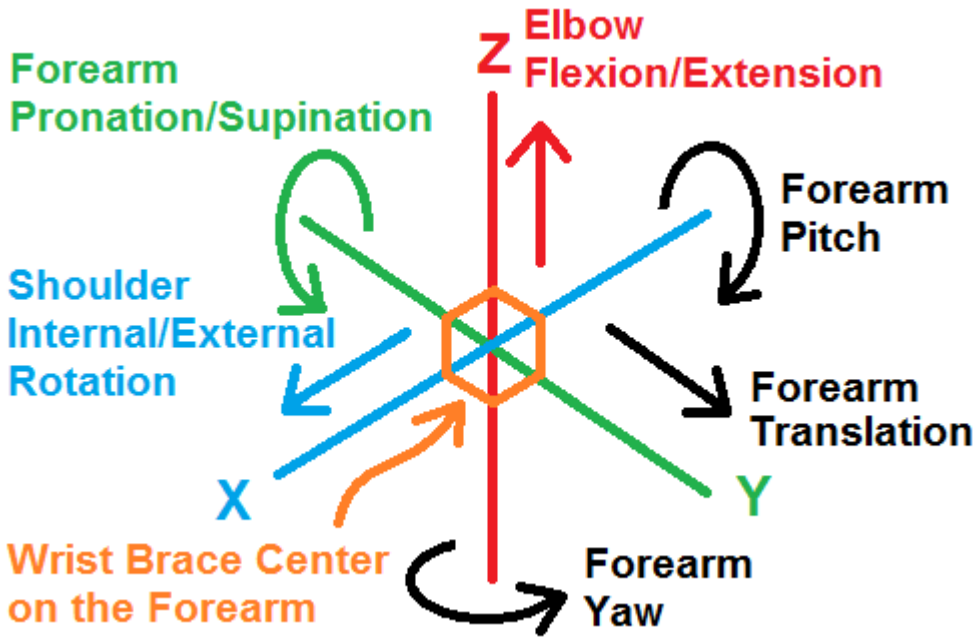

Figure 51 - Degrees of freedom measureable by the wrist brace cushions.

Each of the possible movements can be recognized from specific combinations of force values read by the cushions on the wrist brace exoskeleton. A test setup was made to verify the accuracy of these combinations of forces from the cushions on the wrist brace exoskeleton with a load cell (LCM300, FUTEK Advanced Sensor Technology, Inc., Irvine, CA) [62] and torque sensor (TRT-100, Transducer Techniques, LLC. Temecula, CA) [63] while being mounted on a fixed platform. The difference between the measured cushion values on the wrist brace exoskeleton and the load cell or torque sensor reading was calculated as:

$$\Delta F = |F_{LC} - F_{WB}| \tag{30}$$

where F_{LC} is the force measured from the load cell, F_{WB} is the force measured from the cushions on the wrist brace exoskeleton, and ΔF is the difference in force between the load cell and the combined forces measured from the cushions.

The torsional forces applied on the wrist brace cushions from forearm pronation/supination were measured by a torque sensor, where distance *d* from the axis of rotation to the normal force direction of the cushion surface to create a moment. The number 2 and 5 (green) and 1 and 4 (red) cushions being alternately relaxed and compressed, respectively, as illustrated in Figure 52.

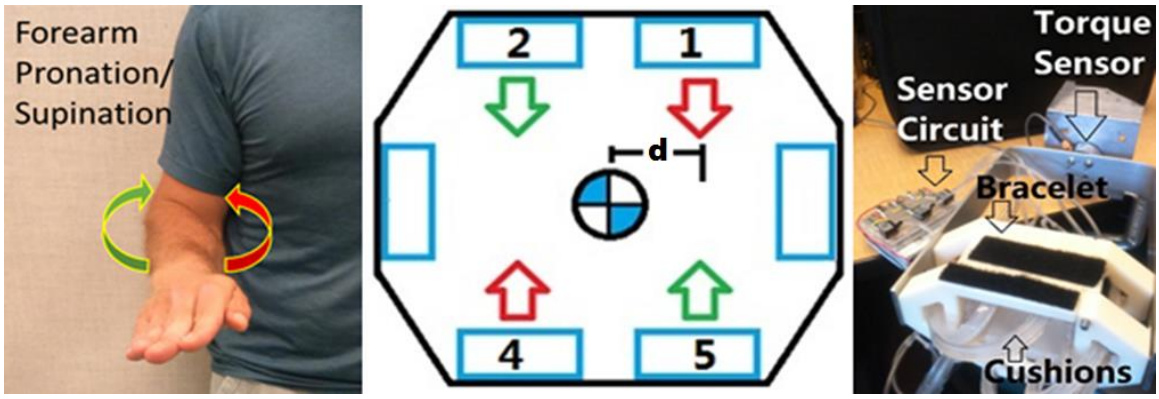

Figure 52 - Forearm pronation/supination, wrist brace and torque sensor.

The torsional forces on the exoskeleton wrist brace due to the pronation/supination of the forearm were measured as:

$$T_{PS} = \left[[F_{C4} + F_{C1}] - [F_{C5} + F_{C2}]\right] * (d) \quad (31)$$

where T_{PS} is the torque of the pronation/supination, F_{C1}, F_{C2}, F_{C4}, and F_{C5} are the forces measured from cushion 1, 2, 4, and 5, respectively, and *d* is the 15mm distance from the center of the wrist brace to the point of the applied force on the cushion surface, as labelled in Figure 52.

The vertical forces at the forearm applied on the wrist brace cushions from elbow flexion/extension were measured by a load cell, with the number 4 and 5 (green) and 2 and 1 (red) cushions being alternately relaxed and compressed as illustrated in Figure 53.

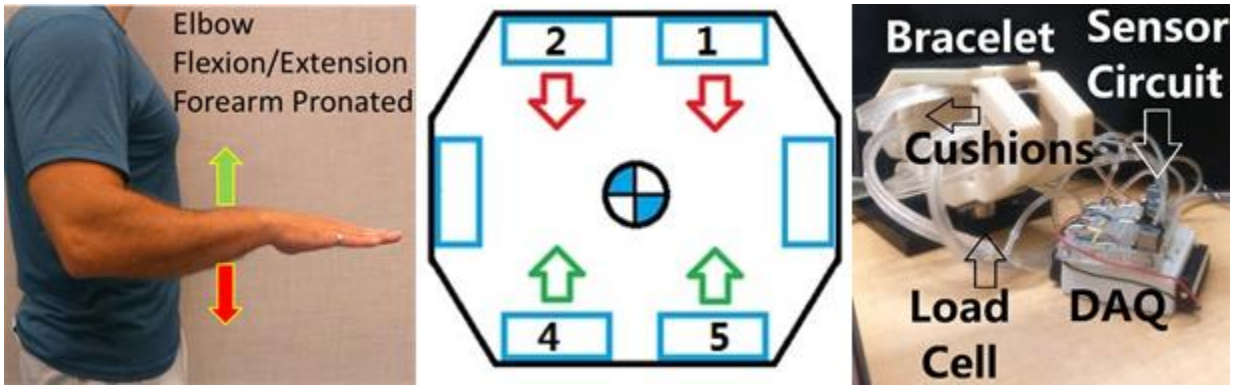

Figure 53 - Elbow flexion/extension, wrist brace and load cell.

The vertical forces on the exoskeleton wrist brace due to the flexion/extension of the elbow, were measured as:

$$F_{FE} = \left[[F_{C4} + F_{C5}] - [F_{C2} + F_{C1}]\right] \quad (32)$$

where F_{FE} is the flexion/extension force with the elbow in the pronated position, F_{C1}, F_{C2}, F_{C4}, and F_{C5} are the forces measured from cushion 1, 2, 4, and 5, respectively.

The horizontal forces at the forearm applied on the wrist brace cushions from internal/external shoulder rotation were measured by a load cell where the number 3 (green) and 6 (red) cushions being alternately relaxed and compressed as illustrated in Figure 54.

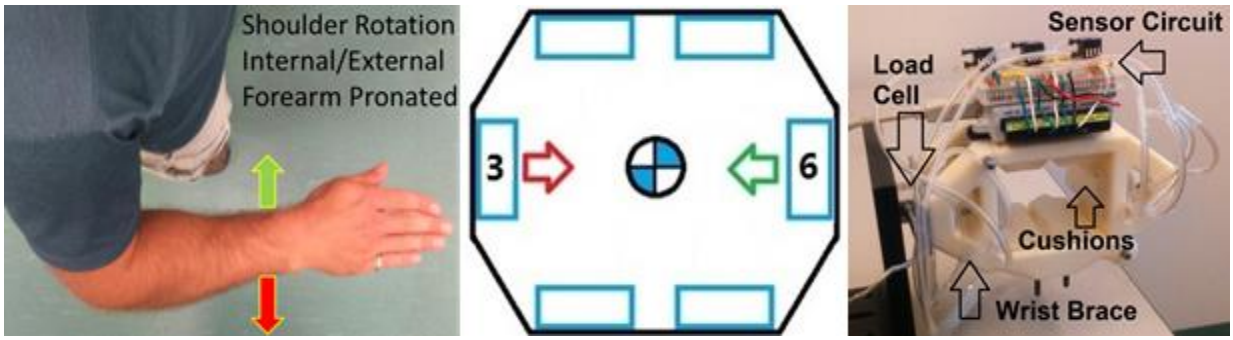

Figure 54 - Shoulder internal/external rotation, wrist brace and load cell.

The horizontal forces on the exoskeleton wrist brace due to the internal/external rotation of the shoulder were measured as:

$$F_{IE} = [F_{C6} - F_{C3}] \tag{33}$$

where F_{IE} is the force measured at the forearm from the internal/external rotation of the shoulder, F_{C6}, and F_{C3}, are the forces measured from cushion 6 and 3, respectively.

The results of the three forearm movements were found through processing the output signals of the differentail pressure sensors and the load cell or torque sensor data through LabVIEW. The data was collected for a session of 60 seconds for each movement. Using the pressure-force relationships for each of the six cushions, the root mean square error (RMSE) between the measured cushion forces and the load cell or torque sensor were calculated. The plot of the torque sensor and the output from the cushions on the wrist brace exoskeleton during forearm pronation/supination is shown in Figure 55. The red line is the combined output torque from the cushions on the wrist brace and the blue line is the data from the torque sensor.

8.3. Cushion and Load Cell/Torque Sensor Comparison

The results of the three forearm movements were found through processing the output signals of the differentail pressure sensors and the load cell or torque sensor data through LabVIEW. The data was collected for a session of 60 seconds for each movement. Using the pressure-force relationships for each of the six cushions, the root mean square error (RMSE) between the measured cushion forces and the load cell or torque sensor were calculated. The plot of the torque sensor and the output from the cushions on the wrist brace exoskeleton during forearm pronation/supination is shown in Figure 55. The red line is the combined output torque from the cushions on the wrist brace and the blue line is the data from the torque sensor.

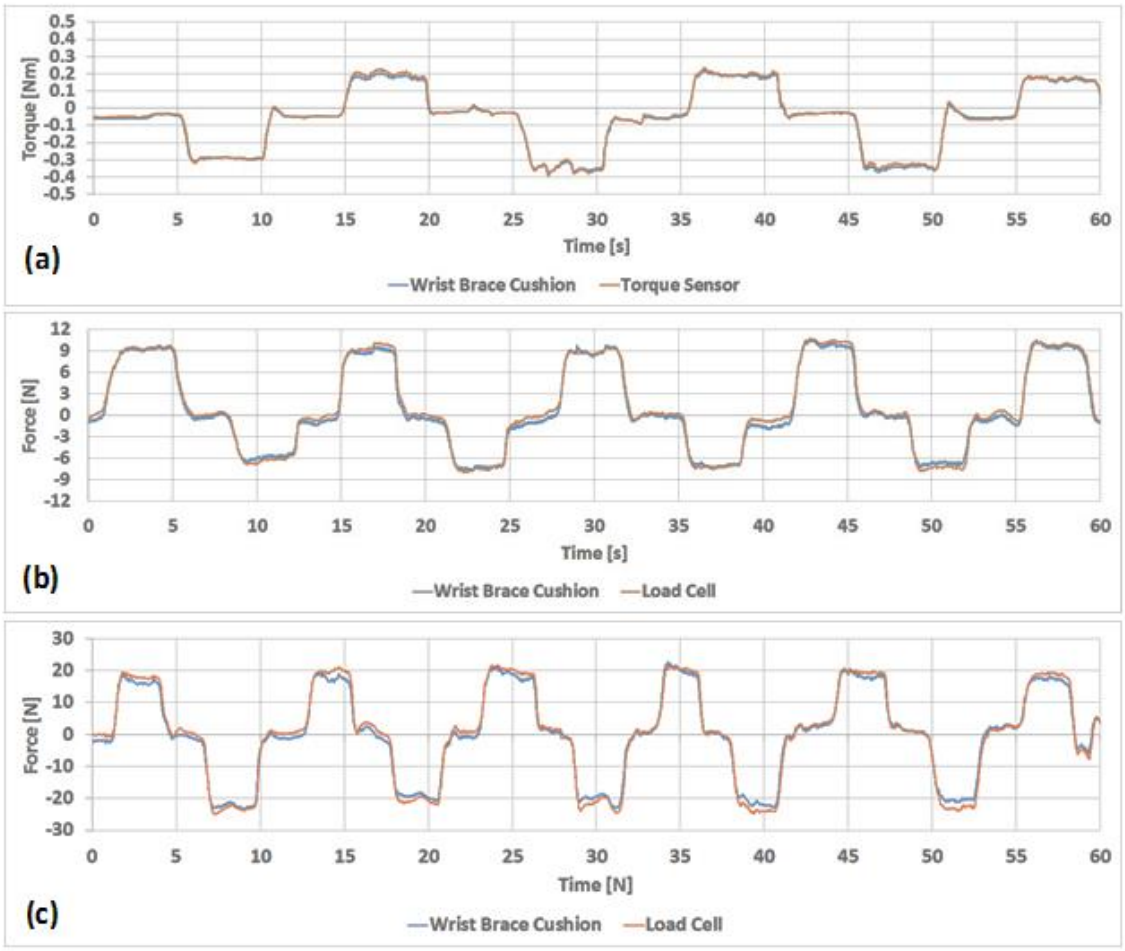

Figure 55 - Forearm pronation/supination a) elbow flexion/extension b) shoulder internal/external rotation c).

The RMSE between the torque sensor values and the combined torque values from the cushions for pronation/supination measured at the forearm was 13mNm (4.3% off from the torque sensor). The RMSE between the load cell values and the combined force values from the cushions for flexion/extension of the elbow measured at the forearm was 0.50N (4.8% off from the load cell). The RMSE between the load cell values and the combined force values from the cushions for internal/external shoulder rotation measured at the forearm was 1.24N (5.7% off from the load cell).

8.4. Summary

These results show that the exoskeleton wrist brace and the differential pressure cushion setup are able to measure the isometric forces and torques from three degrees of freedom at the forearm, and are able to comfortably and accurately measure these forces within a maximum measured RMSE value of 1.24N between the wrist brace exoskeleton cushions and the off-the-shelf load cell or torque sensors. This results in a maximum RMSE percentage between the off the shelf sensors and the cushions on the wrist brace exoskeleton to be less than 6% between the three isometric force directions that were tested in this study. This error is considered to be acceptable, since the RMSE force of the wrist brace cushions that was measured at the forearm for internal/external shoulder rotation, was found to be 1.24N, where if the forearm length is 26.2cm, would result in a torque error of 0.32Nm, which compared to the device by Tsagarakis et al. [30] is an error of 5%. Further work can be done to improve the sensitivity of the cushions which can reduce the error of the cushion compared to conventional off the shelf force and torque sensors.

Chapter 9. Discussion

This chapter is dedicated to the discussion of the cushion and its performance as a force sensor and its potential to be used in exoskeletons for stroke rehabilitation. The FEM model and its comparison to the experimental results is discussed.

9.1. Cushion Performance

The material of PDMS has been shown to be biocompatible and safe to use in micro devices regarding humans [37] [38] and was a good choice of material for the polymeric force cushions in this study. This paper focuses on a proposed biocompatible air polymeric cushion force sensing system for wearable devices, which is attached to a 3D-printed exoskeleton wrist brace. This paper advocates a method for measuring human forces enacted upon machines, which is that these human forces are detected through a change in the air pressure in the polymeric cushion that interacts with the human. An FEM model of the proposed polymeric cushion was made and compared to an experimental test setup with a linear stage and load cell. The polymeric cushion was fabricated in-house though a process of molding and thermal curing of Poly(dimethylsiloxane) (PDMS) to create an air bladder. The performance of these polymeric cushions was experimentally compared to the FEM model in LabVIEW, and the cushions were tested for repeatability, calibrated and characterized for their force measurement. Six polymeric cushions were mounted onto a 3D printed wrist exoskeleton wrist brace. The applied forces measured from the wrist brace were verified with another bench setup fixed onto a stage that measured forces applied from the user's arm onto a load cell and torque sensor through LabVIEW software. The wrist brace exoskeleton with the six polymeric cushions measured isometric forces produced by the pronation/supination of the forearm (rotational motion), as well as the flexion/extension of the elbow (up/down motion), and shoulder internal/external rotation (left/right motion).

The FEM and experimental comparison showed to be within the known error of the pressure sensor, which was ±0.35kPa. The linear curve fitting of the FEM and experimental aluminum plate model and quarter sphere model had an error of 1.28% and

9.05% respectively. The distributed and centralized loading conditions of the cushion FEM showed linear trend lines from the data points of the force and pressure characterization results, due to the R^2 values of the FEM and experimental trend lines being greater than 0.9 and staying within the error bars of the air pressure sensor's uncertainty. The distributed loading of the aluminum plate test, with its small deformation of 5% of the bladder chamber height, suggested a linear relationship between the applied force and the cushion's top surface's displacement. The glass tube's larger deformation of the cushion's top surface had material effects that were not taken into consideration in the FEM model of the glass tube and the cushion, which showed a larger deviation from the experimental data, although still within the error of uncertainty of the pressure sensor and with an R^2 value greater than 0.9.

The maximum error that was found in the repeatability test was from the 8N load, where the sample mean was 2.67kPa with a standard deviation of 0.011kPa. A maximum RMSE between the forces and torques measured from the wrist brace polymeric cushions and the load cell and torque sensor was 1.24N and 13mNm respectively. Typical isometric strength capabilities of human joint torques have been considered in the design of many powered exoskeletons for stroke rehabilitation [64] [65], as described by Tsagarakis et al. [30] where elbow flexion/extension and forearm pronation/supination are said to be 72.5Nm and 9.1Nm respectively [30]. The error of the polymeric cushions is small enough to be used with exoskeletons, such as the two following examples. The first example is the Haptic Knob, which is a robotic end-effector device, where the user grabs the knob interface with their fingers and performs forearm pronation/supination rehabilitation exercises. The 13mNm error of from the polymeric cushions when measuring forearm pronation/supination is less than 1% of the Haptic Knob's maximum forearm pronation/supination torque of 1.5Nm [64]. The second example is the BWRD system, which is a force feedback bimanual wearable elbow rehabilitation device for stroke. The BWRD system's Master and Slave arms were able to provide a maximum theoretical torque of 18.2Nm and 13.9Nm respectively at the elbow for flexion/extension exercises that follow a series of tasks from a training protocol. Within the series of tasks in the protocol, task #5 required stroke individuals to actively move both their elbow joints together. If the force sensors detected that the difference of applied forces between the two arms was >1N, the BWRD would apply resistance to the motion of both arms through

its motor and brake system, prompting the user to correct the imbalance of the forces they are applying on the exoskeleton arms. When the difference of applied forces was <1Nm, the arms would be free to move [65]. The polymeric cushions would be suitable for task #5, since the error in the measured torque at the elbow for flexion/extension would be approximately 0.13Nm if the average forearm length is 26.2cm [66] and the maximum error from the polymeric cushions is 0.5Nm for flexion/extension of the elbow. Herrnstadt et al. [65] observed that a few participants found this task to be difficult, and would consider increasing the 1Nm threshold for some participants. Yet even at this setting, the polymeric cushions would be appropriate for measure elbow flexion/extension forces. The robotic device made by Tsagarakis et al. for upper extremity physiotherapy and training was able to produce 6Nm for torque for the shoulder internal/external rotation joint [67]. The RMSE force of the wrist brace cushions that was measured at the forearm for internal/external shoulder rotation, was found to be 1.24N, where if the forearm length is 26.2cm, would result in a torque error of 0.32Nm, which compared to the device by Tsagarakis et al. is an error of 5%. These errors measured from the polymeric cushions are considered to be acceptable due to the results of the cushion's maximum pressure test, which was able to successfully reach 190N of force before deflating due to air leaks between the interface of the pressure sensor and the polymeric cushion's tube. When taking into account the torque of the elbow joint in the test which reached nearly 50Nm, these results are close to the design requirements from Tsagarakis et al [30] of 70Nm, showing that these cushions are suitable for future applications in measuring force on orthoses for stroke rehabilitation. There was no indication of any ruptures or tears found on the cushion's surface after applied 190N, suggesting that if the interface between the polymeric cushion tube and the pressure sensor was more securely sealed, it is likely that the polymeric cushions would be able to sustain even greater forces without failure.

The FEM model of the polymeric cushions represents a good estimation of the experimental data using the linear stage test setup. The use of a comfortable and flexible air cushion to be used as an air pressure sensor on an exoskeleton's human machine interface shows potential to be a useful device for rehabilitation exercises. This proposed wrist brace exoskeleton, based upon the prototype that was developed, demonstrates an example of the polymeric cushions' future applications.

9.2. Summary

The polymeric cushions showed good potential as a useful force sensors for exoskeletons in rehabilitation training and assistive devices. The FEM model of the aluminum plate and glass tube is a good representation of the cushion's behaviour when subjected to loads on its top surface. The FEM and experimental characterization results were both fitted with a linear trend line that was within the error bounds of the pressure sensor and had an R^2 value greater than 0.9. Its ability to transmit forces from a human forearm and be used to measure the movements of the forearm is a feasible use of the cushions. The cushions performed well when compared to the off-the-shelf load cell and torque sensor, since the maximum measured error found between the cushions and the off-the-shelf sensors was less than 6%. When compared to rehabilitation exoskeletons from other work, the polymeric cushions were found to be suitable for their applications given the rehabilitation protocols or the range of forces required of the exoskeletons. When compared to the prior art of cushion force sensors, the polymeric cushions in their study were able to outperform the force measuring range of other cushions before saturating or reaching its maximum force at 190N. As suggested by Tsagarakis et al. [30] this is 69% of what is recommended for exoskeletons to be able to measure from interactions with the human body, where the highest percentage of the maximum force from the prior art had only 22% of this recommended value. The polymeric cushions, which act as a mechanical sensor, can be connected to any pressure sensor and so can be used in a variety of applications which are not limited by a specific predefined resolution of pressure or force.

Chapter 10. Conclusions

In this thesis, a proposed polymeric air cushion for measuring applied forces from a human forearm onto an orthosis is presented. The cushions showed to be suitable for measuring forces in applications with for robotic rehabilitation, as the errors measured from the cushions was within the acceptable error of robotic devices used for stroke rehabilitation. Six polymeric cushions were mounted onto the interface surface of a wrist brace exoskeleton, with the goal of being able to ideally meet the following criteria: to be in direct contact with the user's forearm to measure isometric forces, to be light weight, to be functionally easy to use, and to comfortably conform to the shape of a user's arm. This reduced the measured force error that would occur from calculating an indirect force from where the sensors were located, which was on another part of the exoskeleton structure. The flexible polymeric cushions conforming to the user's arm also allowed for direct measurements, since there was no gap between the cushion's top surface and the arm.

10.1. Summary of Accomplishments

The first objective of this thesis was to improve on the prior art of a polymeric cushion force sensing system, in terms of the maximum applied force on the cushion before saturation or leaking of air. The maximum applied force was found to be 190N from a maximum pressure test conducted at the forearm. The cushion also improved on the comfort of the user from the cushion, made by Zampierin et al. while still weighting only 20g, being flexible and comfortable, as well as being easy to put on. Objective 1 was accomplished with the cushion's new tubing configuration sealing the major leaking issue, and the removal of the PMMA contact surface for comfort and conformity to the shape of the forearm. Improvements were also made on the choice of air pressure sensor with respect to its sensing range, resolution, and a reduction in the number of sensors from six individual gauge pressure sensors, as shown in the configuration by Zampierin et al., to three with differential pressure sensors that were used in this study.

The second objective of this thesis was to create an FEM model of the polymeric cushion to simulate compression from a load on the cushion's top surface, first with a flat

aluminum plate, and another with a spherical glass tube. This would be similar to when the polymeric cushion is loaded by an arm that covered the whole surface and from a centralized loading point, such as the Ulna or Radius bones when worn by the wrist brace. The top surface of the cushion that would come into contact with the forearm is made such that one cushion fits along the width and thickness of the arm, which led to a rectangular shape. The finite element model suggested a linear trend of the force and pressure characterization curves for the glass tube and aluminum plate models, as well as showing a maximum air pressure range that the experimental setup would require to measure. With these results, the new proposed cushion configuration would proceed to be fabricated. Then a new mold with the bladder and tube connected as one piece was 3D-printed and used to fabricate six new leak-resistant polymeric cushions made from PDMS that weighted only 20g. The polymeric cushions were connected to an air pressure sensor to measure the applied forces through a DAQ and a LabVIEW program. The flexibility of choosing the desired air pressure sensor allows for customizing the device accuracy and precision for a specific application, such as the forearm forces performed in this study. The next step was to perform a repeatability test, a long period test, and a failure test. The test cushion underwent a repeatability test, where five cycles of loading and unloading were performed and repeated for 2N, 4N, 6N, and 8N. The 8N load which had a mean value of 2.67kPa had the largest standard deviation from the repeatability test was 0.02kPa. The cushions characterize the polymeric cushions for their input force and output pressure. Next was to compare the FEM results with the experimental testing. The test cushion was subjected to the same loads as simulated in the FEM model. Objective 2 was accomplished with the comparison between the FEM and experimental results showed the difference to be within the error of the air pressure sensor from the experimental results and showed a difference in their linear fitting lines to be 1.28% and 9.05% for the aluminum flat plate and the glass tube models respectively. The R^2 values of both the experimental and FEM characterization trend lines were above 0.9 and were within the error of the air pressure sensor, giving the confidence to move onto the application testing of the cushions on a wrist brace exoskeleton. The maximum pressure test showed that the cushion failed at 69% of the suggested measureable torque from Tsagarakis et al. [30] where the maximum force from the prior art was only 22% of this suggested value.

The third and final objective of this thesis was to test the new polymeric cushions on a wrist brace exoskeleton. The wrist brace exoskeleton was mounted with six individual cushions and configured to measure the isometric forces at the forearm. A test was made to compare the differences between the forces and torques measured by the wrist brace exoskeleton's polymeric cushions and an off-the-shelf torque sensor and load cell. Objective 3 was accomplished with the RMSE difference between the off-the-shelf sensors and the polymeric cushions was found to be 13.5mNm of error (4.3% from the torque sensor) for forearm pronation/supination, 0.50N of error (4.8% from the load cell) for elbow flexion/extension which 0.13Nm of torque at the elbow, and 1.24N of error (5.7% from the load cell) for internal/external shoulder rotation which is 0.32Nm of torque error at the shoulder.

10.2. Future Works

Some future work would involve the exploration of different shapes and sizes of the polymeric cushions that may be used to measure movements of other parts of the body, and optimizing the dimensions to maximize the sensitivity of the cushions using the FEM model. Further testing should be done to find the best material properties of PDMS for the application of force sensing on wearable exoskeletons, by maximizing the stiffness of the cushion material from the ratio of the PDMS hardening and bulk materials. This optimized ratio will improve the sensitivity of the cushion for force sensing, although still holding a balance of stiffness and softness for the comfort of the user. Also, the improvements should also be made to better seal the interface between the cushion tube and the pressure sensor from air leaks to maximize the usable pressure range of the cushion until saturation levels are achieved. Other future work would be to have more intensive dynamic testing with the polymeric cushions, as well as performing end-of-life tests. The effects of a significantly longer version of the polymeric cushion's tube has not been tested yet for its time delay effects to the system. There is potential for these cushions to be used in an MEG room since conductive materials are prohibited [20]. In order to fully allow the polymeric cushions to be functional in an MEG room, the tubes of the polymeric cushions must extend out of the magnetically sealed room and into the data analysis equipment room to process the data. The polymeric cushions could be mounted on a newly 3D printed

ergonomic exoskeleton wrist brace, which should be attached onto a fully functional arm exoskeleton with abilities to perform forearm pronation/supination (rotation), elbow flexion/extension with forearm pronated (up/down), and internal/external shoulder rotation (left/right). Although with a second row of cushions around the forearm, more degrees of freedom of the arm can be measured. These include forearm pitch (rotation about the forearm center moving up/down), forearm yaw (rotation about the forearm center moving left/right), and forearm translation (forward/backward along the forearm). This new forearm cuff should be made similar to the one that was created for the bimanual rehabilitation robot for upper extremities called the BWRD in the MENRVA research lab in Simon Fraser University [17]. Using the BWRD forearm cuff as inspiration will allow the new iteration of the wrist brace exoskeleton to conform to the shape of the forearm, and should be fabricated with hole-inserts where the polymeric cushions can be embedded into the forearm cuff. Using plate bending equations [59] [60], the displacement of the cushion's surface can be mathematically modeled to show that the applied load from the aluminum plate and the glass tube that was attached to the linear stage has a relationship with the air pressure inside the cushion.

References

[1] “Statistics - Heart and Stroke Foundation of Canada,” *heartandstroke.ca*. [Online]. Available: http://www.heartandstroke.com/site/c.ikIQLcMWJtE/b.3483991/k.34A8/Statistics.htm. [Accessed: 10-Apr-2016].

[2] D. Lynch, M. Ferraro, J. Krol, C. M. Trudell, P. Christos, and B. T. Volpe, “Continuous passive motion improves shoulder joint integrity following stroke,” *Clin. Rehabil.*, vol. 19, no. 6, pp. 594–599, Sep. 2005.

[3] A. A. Blank, J. A. French, A. U. Pehlivan, and M. K. O’Malley, “Current Trends in Robot-Assisted Upper-Limb Stroke Rehabilitation: Promoting Patient Engagement in Therapy,” *Curr. Phys. Med. Rehabil. Rep.*, vol. 2, no. 3, pp. 184–195, Jun. 2014.

[4] M. Caimmi *et al.*, “Predicting Functional Recovery in Chronic Stroke Rehabilitation Using Event-Related Desynchronization-Synchronization during Robot-Assisted Movement,” *BioMed Res. Int.*, vol. 2016, p. e7051340, Jan. 2016.

[5] N. Hogan *et al.*, “Motions or muscles? Some behavioral factors underlying robotic assistance of motor recovery,” *J. Rehabil. Res. Dev.*, vol. 43, no. 5, pp. 605–618, Sep. 2006.

[6] S. Zampierin, “Study, Analysis, Implementation and Testing of a Force Gauge for Rehabilitation,” Master of Applied Science, 2Department of Industrial Engineering, University of Padua, Via Venezia 1, Padua, Italy, Italy, 2014.

[7] S. Zampierin, N. Alavi, S. Cocuzza, S. Debei, and C. Menon, “Design, Fabrication, and Testing of a Polymer Force Transducer for Rehabilitation Exoskeletons,” presented at the CanSmart 2015.

[8] S. W. Brose *et al.*, “The Role of Assistive Robotics in the Lives of Persons with Disability:,” *Am. J. Phys. Med. Rehabil.*, vol. 89, no. 6, pp. 509–521, Jun. 2010.

[9] G. Kwakkel, B. J. Kollen, and H. I. Krebs, “Effects of Robot-assisted therapy on upper limb recovery after stroke: A Systematic Review,” *Neurorehabil. Neural Repair*, vol. 22, no. 2, pp. 111–121, 2008.

[10] P. S. Lum, C. G. Burgar, and P. C. Shor, “Evidence for improved muscle activation patterns after retraining of reaching movements with the MIME robotic system in subjects with post-stroke hemiparesis,” *IEEE Trans. Neural Syst. Rehabil. Eng.*, vol. 12, no. 2, pp. 186–194, Jun. 2004.

[11] D. J. Reinkensmeyer, L. E. Kahn, M. Averbuch, A. McKenna-Cole, B. D. Schmit, and W. Z. Rymer, “Understanding and treating arm movement impairment after chronic brain injury: progress with the ARM guide,” *J. Rehabil. Res. Dev.*, vol. 37, no. 6, pp. 653–662, Dec. 2000.

[12] B. Husemann, F. Müller, C. Krewer, S. Heller, and E. Koenig, “Effects of Locomotion Training With Assistance of a Robot-Driven Gait Orthosis in Hemiparetic Patients After Stroke A Randomized Controlled Pilot Study,” *Stroke*, vol. 38, no. 2, pp. 349–354, Feb. 2007.

[13] K. K. Ang *et al.*, “Brain-computer interface-based robotic end effector system for wrist and hand rehabilitation: results of a three-armed randomized controlled trial for chronic stroke,” *Front. Neuroengineering*, vol. 7, p. 30, 2014.

[14] P. Maciejasz, J. Eschweiler, K. Gerlach-Hahn, A. Jansen-Troy, and S. Leonhardt, “A survey on robotic devices for upper limb rehabilitation,” *J. NeuroEngineering Rehabil.*, vol. 11, p. 3, 2014.

[15] N. G. Kutner, R. Zhang, A. J. Butler, S. L. Wolf, and J. L. Alberts, “Quality-of-Life Change Associated With Robotic-Assisted Therapy to Improve Hand Motor Function in Patients With Subacute Stroke: A Randomized Clinical Trial,” *Phys. Ther.*, vol. 90, no. 4, pp. 493–504, Apr. 2010.

[16] S. Patel *et al.*, “A Novel Approach to Monitor Rehabilitation Outcomes in Stroke Survivors Using Wearable Technology,” *Proc. IEEE*, vol. 98, no. 3, pp. 450–461, Mar. 2010.

[17] G. Herrnstadt, N. Alavi, B. K. Randhawa, L. A. Boyd, and C. Menon, “Bimanual Elbow Robotic Orthoses: Preliminary Investigations on an Impairment Force-Feedback Rehabilitation Method,” *Front. Hum. Neurosci.*, vol. 9, Mar. 2015.

[18] R. Song, K. Tong, X. Hu, and W. Zhou, “Myoelectrically controlled wrist robot for stroke rehabilitation,” *J. NeuroEngineering Rehabil.*, vol. 10, p. 52, 2013.

[19] P. G. Jung, G. Lim, S. Kim, and K. Kong, “A Wearable Gesture Recognition Device for Detecting Muscular Activities Based on Air-Pressure Sensors,” *IEEE Trans. Ind. Inform.*, vol. 11, no. 2, pp. 485–494, Apr. 2015.

[20] A. Keil *et al.*, “Committee report: publication guidelines and recommendations for studies using electroencephalography and magnetoencephalography,” *Psychophysiology*, vol. 51, no. 1, pp. 1–21, Jan. 2014.

[21] S. L. Phillips and W. Craelius, “Residual kinetic imaging: a versatile interface for prosthetic control,” *Robotica*, vol. 23, no. 3, pp. 277–282, May 2005.

[22] R. L. Abboudi, C. A. Glass, N. A. Newby, J. A. Flint, and W. Craelius, “A biomimetic controller for a multifinger prosthesis,” *IEEE Trans. Rehabil. Eng.*, vol. 7, no. 2, pp. 121–129, Jun. 1999.

[23] L. Yu, J. Zheng, Y. Wang, Z. Song, and E. Zhan, “Adaptive method for real-time gait phase detection based on ground contact forces,” *Gait Posture*, vol. 41, no. 1, pp. 269–275, Jan. 2015.

[24] K. Kong and M. Tomizuka, “Smooth and continuous human gait phase detection based on foot pressure patterns,” in *IEEE International Conference on Robotics and Automation, 2008. ICRA 2008*, 2008, pp. 3678–3683.

[25] G. T. Bae, J. B. Song, and B. S. Kim, “Imitation of human motion based on variable stiffness actuator and muscle stiffness sensor,” in *2013 IEEE/ASME International Conference on Advanced Intelligent Mechatronics*, 2013, pp. 1016–1020.

[26] Y. Makino, Y. Sugiura, M. Ogata, and M. Inami, “Tangential Force Sensing System on Forearm,” in *Proceedings of the 4th Augmented Human International Conference*, New York, NY, USA, 2013, pp. 29–34.

[27] “Myo Gesture Control Armband.” [Online]. Available: https://www.myo.com/. [Accessed: 08-Sep-2016].

[28] B. Zhou, M. Sundholm, J. Cheng, H. Cruz, and P. Lukowicz, “Never skip leg day: A novel wearable approach to monitoring gym leg exercises,” in *2016 IEEE International Conference on Pervasive Computing and Communications (PerCom)*, 2016, pp. 1–9.

[29] S. M. M. De Rossi *et al.*, “Sensing Pressure Distribution on a Lower-Limb Exoskeleton Physical Human-Machine Interface,” *Sensors*, vol. 11, no. 1, pp. 207–227, Dec. 2010.

[30] N. Tsagarakis, D. G. Caldwell, and G. A. Medrano-Cerda, “A 7 DOF pneumatic muscle actuator (pMA) powered exoskeleton,” in *8th IEEE International Workshop on Robot and Human Interaction, 1999. RO-MAN ’99*, 1999, pp. 327–333.

[31] A. W. Andrews and R. W. Bohannon, “Distribution of muscle strength impairments following stroke,” *Clin. Rehabil.*, vol. 14, no. 1, pp. 79–87, Feb. 2000.

[32] H. Kazerooni, J. L. Racine, L. Huang, and R. Steger, “On the Control of the Berkeley Lower Extremity Exoskeleton (BLEEX),” in *Proceedings of the 2005 IEEE International Conference on Robotics and Automation, 2005. ICRA 2005*, 2005, pp. 4353–4360.

[33] A. Raichur, G. Wihardjo, S. Banerji, and J. Heng, “A step towards home-based robotic rehabilitation: An interface circuit for EEG/SEMG actuated orthosis,” in *IEEE/ASME International Conference on Advanced Intelligent Mechatronics, 2009. AIM 2009*, 2009, pp. 1998–2003.

[34] B. T. Volpe *et al.*, “Intensive Sensorimotor Arm Training Mediated by Therapist or Robot Improves Hemiparesis in Patients With Chronic Stroke,” *Neurorehabil. Neural Repair*, vol. 22, no. 3, pp. 305–310, May 2008.

[35] A. Schiele and F. C. T. van der Helm, “Kinematic Design to Improve Ergonomics in Human Machine Interaction,” *IEEE Trans. Neural Syst. Rehabil. Eng.*, vol. 14, no. 4, pp. 456–469, Dec. 2006.

[36] R. D. Willmann, G. Lanfermann, P. Saini, A. Timmermans, J. t Vrugt, and S. Winter, “Home Stroke Rehabilitation for the Upper Limbs,” in *29th Annual International Conference of the IEEE Engineering in Medicine and Biology Society, 2007. EMBS 2007*, 2007, pp. 4015–4018.

[37] T. G. van Kooten, J. F. Whitesides, and A. F. von Recum, “Influence of silicone (PDMS) surface texture on human skin fibroblast proliferation as determined by cell cycle analysis,” *J. Biomed. Mater. Res.*, vol. 43, no. 1, pp. 1–14, Mar. 1998.

[38] D. S. Lee *et al.*, “Biocompatibility of a PDMS-coated micro-device: Bladder volume monitoring sensor,” *Chin. J. Polym. Sci.*, vol. 30, no. 2, pp. 242–249, Mar. 2012.

[39] S. Zampierin, N. Alavi, S. Cocuzza, S. Debei, and C. Menon, “Design, Fabrication, and Testing of a Polymer Force Transducer for Rehabilitation Exoskeletons,” presented at the CanSmart, MENRVA Research Group, Room ASB 10839, School of Engineering science, Simon Fraser University, 8888 University Drive, Burnaby, BC, V5A 1S6, Canada, Dipartimento di Ingegneria Industriale, Corso di Laurea in Ingegneria Aerospaziale, Università degli Studi di Padova, Via Gradenigo, 6/a - 35131 Padova PD, Italy.

[40] “Tygon S3 E-3603 Laboratory Tubing (Imperial Sizes) | Teastech, Ireland | Saint-Gobain Performance Plastics | Teflon | CHR Tapes | Tygon.” .

[41] “About Fortus 250mc Product 3D Manufacturing Machine | Stratasys.” [Online]. Available: http://www.stratasys.com/3d-printers/design-series/fortus-250mc. [Accessed: 28-Nov-2016].

[42] “ABSplus, Fortus 3D Production Systems FDM Materials | Stratasys.” [Online]. Available: http://www.stratasys.com/materials/fdm/absplus. [Accessed: 28-Nov-2016].

[43] “SYLGARD® 184 SILICONE ELASTOMER KIT.” [Online]. Available: http://www.dowcorning.com/applications/search/products/Details.aspx?prod=01064291. [Accessed: 31-Mar-2016].

[44] “VLS3.60 Laser Platform.” [Online]. Available: http://www.ulsinc.com/products/vls360/. [Accessed: 10-Apr-2016].

[45] “Check Out the Latest CorelDRAW Graphics Suite.” [Online]. Available: /en/product/graphic-design-software/. [Accessed: 14-Dec-2016].

[46] N. Alavi, “Operation of CO2 Laser Cutter for Material Cutting/Engraving and Microchannel Fabrication,” Simon Fraser University School of Engineering Science and School of Mechatronic Systems Engineering, Lab Manual Revised Version 2, May 2014.

[47] H.-B. Liu and H.-Q. Gong, “Templateless prototyping of polydimethylsiloxane microfluidic structures using a pulsed CO 2 laser,” *J. Micromechanics Microengineering*, vol. 19, no. 3, p. 37002, 2009.

[48] A. W. Holle, S. H. Chao, M. R. Holl, J. M. Houkal, and D. R. Meldrum, “Characterization of Program Controlled CO2 Laser-Cut PDMS Channels for Lab-on-a-chip Applications,” in *IEEE International Conference on Automation Science and Engineering, 2007. CASE 2007*, 2007, pp. 621–627.

[49] Z. Isiksacan, M. T. Guler, B. Aydogdu, I. Bilican, and C. Elbuken, “Rapid fabrication of microfluidic PDMS devices from reusable PDMS molds using laser ablation,” *J. Micromechanics Microengineering*, vol. 26, no. 3, p. 35008, 2016.

[50] “MPXV7007DP Freescale Semiconductor - NXP | Sensors, Transducers | DigiKey.” [Online]. Available: http://www.digikey.ca/product-detail/en/freescale-semiconductor-nxp/MPXV7007DP/MPXV7007DP-ND/1168438. [Accessed: 10-Apr-2016].

[51] “MPXV5100GP Freescale Semiconductor | Mouser,” *Mouser Electronics*. [Online]. Available: http://ca.mouser.com/Search/ProductDetail.aspx?R=MPXV5100GPvirtualkey55700000virtualkey841-MPXV5100GP. [Accessed: 04-Dec-2014].

[52] “ANSYS - Simulation Driven Product Development.” [Online]. Available: http://www.ansys.com/. [Accessed: 31-Mar-2016].

[53] F. Schneider, J. Draheim, R. Kamberger, and U. Wallrabe, “Process and material properties of polydimethylsiloxane (PDMS) for Optical MEMS,” *Sens. Actuators Phys.*, vol. 151, no. 2, pp. 95–99, Apr. 2009.

[54] Sheldon Imaoka, “Hydrostatic Fluid Elements at ANSYS 13.0,” *ANSYS Inc.*, 2010. [Online]. Available: http://ansys.net/ansys/input/expansion.pdf. [Accessed: 31-Mar-2016].

[55] “Linear Slides and Linear Actuators from Zaber Technologies.” [Online]. Available: http://www.zaber.com/. [Accessed: 31-Mar-2016].

[56] “LRF400 Tension and Compression Load Cell.” [Online]. Available: http://www.futek.com/product.aspx?t=load&m=lrf400. [Accessed: 31-Mar-2016].

[57] “MPXV7007DP Freescale Semiconductor - NXP | Sensors, Transducers | DigiKey.” [Online]. Available: http://www.digikey.ca/product-detail/en/freescale-semiconductor-nxp/MPXV7007DP/MPXV7007DP-ND/1168438. [Accessed: 31-Mar-2016].

[58] “NI USB-6009 14-Bit, 48 kS/s Low-Cost Multifunction DAQ,” *National Instruments Corporation*. [Online]. Available: http://sine.ni.com/nips/cds/view/p/lang/en/nid/201987.

[59] S. Timoshenko and S. Woinowsky-Krieger, *Theory of plates and shells*. McGraw-Hill, 1959.

[60] E. Ventsel and T. Krauthammer, *Thin Plates and Shells: Theory: Analysis, and Applications*. CRC Press, 2001.

[61] S. S. Zumdahl and D. J. DeCoste, *Chemical Principles*. Nelson Education, 2016.

[62] “LCM300 Miniature/Inline Threaded Tension and Compression Load Cell.” [Online]. Available: http://www.futek.com/product.aspx?t=load&m=lcm300. [Accessed: 10-Apr-2016].

[63] “TRT Series low capacity (In- lb) general purpose reaction Torque Sensor.” [Online]. Available: https://www.transducertechniques.com/trt-torque-sensor.aspx. [Accessed: 01-Apr-2016].

[64] O. Lambercy *et al.*, “Rehabilitation of grasping and forearm pronation/supination with the Haptic Knob,” in *2009 IEEE International Conference on Rehabilitation Robotics*, 2009, pp. 22–27.

[65] G. Herrnstadt, N. Alavi, B. K. Randhawa, L. A. Boyd, and C. Menon, “Bimanual Elbow Robotic Orthoses: Preliminary Investigations on an Impairment Force-Feedback Rehabilitation Method,” *Front. Hum. Neurosci.*, vol. 9, Mar. 2015.

[66] “Size of a Human: Body Proportions.” [Online]. Available: http://hypertextbook.com/facts/2006/bodyproportions.shtml. [Accessed: 05-Jul-2016].

[67] N. G. Tsagarakis and D. G. Caldwell, “Development and Control of a ‘Soft-Actuated’ Exoskeleton for Use in Physiotherapy and Training,” *Auton. Robots*, vol. 15, no. 1, pp. 21–33, Jul. 2003.